Influence of dynamic mechanical properties of subgrade soil in cold climate on fatigue life of road pavement

寒冷気候下の路床土の動的力学特性が道路舗装の疲労寿命に及ぼす影響

By

Tianshu LIN

A thesis submitted in partial fulfilment of the requirements for the degree of Doctor of Philosophy in Engineering

under the guidance and supervision of

Professor Tatsuya ISHIKAWA

Examined by the Doctoral Committee

Professor Tatsuya ISHIKAWA
Professor Yoichi WATABE
Professor Yoshiaki FUJII

September 2020

English Engineering Program (e^3)

Laboratory of Analytical Geomechanics

Division of Field Engineering for the Environment

Graduate School of Engineering

Hokkaido University
Sapporo, Hokkaido, Japan

ABSTRACT

Current Japanese design guide uses mechanical-empirical criteria to predict the failure loading number against cracking and rutting. These criteria have some limitations that variant base and subgrade layer moduli with fluctuating water contents, freeze-thaw history, stress states are not considered. However, in snowy cold regions such as Hokkaido, a northern island in Japan, pavement structures suffer annually freeze-thaw cycles as the 0°C isotherm may penetrate deep into the pavement. Freeze-thaw action deteriorates pavement structures in two ways as frost-heave and thaw-weakening. Swelling of soil during freezing conditions caused by an increasing presence of ice lens finally leads to cracking in asphalt-mixture layer. Thaw-weakening means a drop of base and subgrade layer strength and stiffness caused by suddenly rising water content, which comes from the inflow of snowmelt water or the thawing of ice lenses, and deteriorates uniformity of particle skeleton structure after freeze-thaw action. A detailed understanding of the mechanical behavior of the base/subgrade materials during freeze-thaw is essential to develop a mathematical model of the mechanical response of the base/subgrade layer in cold regions and incorporate it into the theoretical design method for pavement structures. To achieve such understanding, it is necessary to quantitatively capture the deformation-strength characteristics of unbound granular base course and subgrade materials subjected to cyclic freeze-thaw actions under various compaction conditions and water contents through laboratory element tests with high-precision under sufficiently controlled experimental conditions. As the results, a significant loss of stiffness from frozen to thawed and an increase in the recovery period are observed in both in-situ bearing capacity test for frozen and thawed pavement structure and laboratory element test for frozen, thawed, and recovered base/subgrade material.

However, partly due to the apparatus limitation and different research topic, the synergistic effects between water content and freeze-thaw on the resilient modulus, which is the key factor of base/subgrade layer as it associates with the elastic modulus used in the design calculation for pavement structures applying the multi-layer elastic theory or finite element method, have not yet been quantitatively evaluated and modelled in these tests. Besides, rutting failure criterion used now provides no indication of the behavior of rutting over time and the effect of principal stress axis rotation on rutting development is also not captured.

To overcome such limitations, this study firstly examines the effects of freeze-thaw actions and the concurrent seasonal fluctuations in water content, named as climate effect in this study,

on the resilient modulus of subgrade materials to evaluate their mechanical behavior in cold regions. A series of suction-controlled resilient modulus tests on subgrade materials with variant freeze-thaw, wheel loads, and water contents conditions were conducted using a newly developed test apparatus. Test results were used to construct a simple model to estimate the climate effect on the resilient modulus by considering the synergistic effects between water content and freeze-thaw. This model is also proved to be valid when estimating the resilient modulus of base course material subjected to complex moisture content and freeze-thaw action. Then, constant base course and subgrade layer elastic modulus used in current Japanese design guide are replaced to resilient modulus related to stress states and complex climate conditions. Secondly, rutting failure criterion used in current Japanese design guide is revised referring to widely used Mechanical-Empirical Pavement Design Guide model. Besides, the effect of principal stress axis rotation is examined based on previous test results obtained through multi-ring shear apparatus, which could apply axial stress and shear stress simultaneously to simulate the principal stress axis rotation. Effect of principal stress axis rotation on rutting is also used to modify the rutting failure criterion. Applicability and accuracy of modified Japanese design guide are proved to be high on the failure loading prediction especially on the flexible pavement in cold regions by comparing predict fatigue life to long-term measured performance of test pavements built in Hokkaido. Chapter 1 introduces the background, objective, and organization of this study. Chapter 2 gives the detail of test apparatus, like freeze-thaw triaxial apparatus and medium-size triaxial apparatus, and test material used for resilient modulus test used in this study. Chapter 3 describes the test methods and experimental conditions of resilient modulus test under complex combination of matric suction, freeze-thaw action, and wheel loads. Chapter 4 presents the resilient modulus test results obtained in this study. A modified constitutive model is proposed to capture the synergistic effect between water contents and freeze-thaw action on resilient modulus of subgrade material. Chapter 5 discussed the effect of principal stress axis rotation on permanent deformation of specimen based on previous multi-ring shear test. Chapter 6 gives a modified pavement design guide comes from laboratory element test results shown in Chapter 4 and 5. Predicted fatigue life through modified design method is compared with long-term performance observation data to check the applicability. Chapter 7 summarizes the conclusion obtained in this study.

< This dissertation is a modified and revised form of the following original journals and proceedings>

Lin T, Ishikawa T, Luo B: Applicability of modified University of Illinois at Urbana–Champaign model for unbound aggregate material with different water content. *Transportation Research Record: Journal of the Transportation Research Board*, Vol.2673, No.3, pp 439-449 (2019). (DOI: https://doi.org/10.1177/0361198119827530)

Ishikawa T, Lin T, Yang J, et al.: Application of the UIUC model for predicting ballast settlement to unsaturated ballasts under moving wheel loads. *Transportation Geotechnics*, Vol.18, pp 149-162 (2019). (DOI: https://doi.org/10.1016/j.trgeo.2018.12.003)

Ishikawa T, Lin T, Kawabata S, et al.: Effect evaluation of freeze-thaw on resilient modulus of unsaturated granular base course material in pavement. *Transportation Geotechnics*, Vol.21, 100284 (2019). (DOI: https://doi.org/10.1016/j.trgeo.2019.100284)

Lin T, Ishikawa T, Yang J, et al.: Evaluation of climate effect on resilient modulus of granular subgrade material. *Cold Regions Science and Technology*. (under review)

Lin T, Ishikawa T, Tokoro T: Testing method for resilient properties of unsaturated unbound granular materials subjected to freeze-thaw action. *7th Asia-Pacific Conference on Unsaturated Soils*, 2019 Aug 23-25, Nagoya, Japan.

Lin T, Ishikawa T, Aoki R, et al: Resilient properties of unbound granular materials subjected to freeze-thaw and wheel loads. *16th Asian Regional Conference on Soil Mechanics and Geotechnical Engineering*, 2019 Oct 14-18, Taipei.

Lin T, Ishikawa T, Tokoro T, et al: Performance evaluation of modified UIUC model with the consideration of principal stress axis rotation. *XVI Pan-American Conference on Soil Mechanics and Geotechnical Engineering*, 2019 Nov 17-20, Cancun, Mexico.

ACKNOWLEDGEMENT

My deepest gratitude goes first and foremost to my supervisor, Prof. Tatsuya Ishikawa for his patient guidance, understanding, and support throughout the course of this study. It is Sensei who introduce me to the field of unsaturated soil mechanics and transportation geomechanics and encourage me to explore unknown. The good example in rigorous academic attitude and hard-working set by him always inspire me. Without research environment and resource provided by Sensei, this dissertation would not have been possible.

Thanks are also due to all members of doctoral committee, Prof. Yoichi Watabe and Prof. Yoshiaki Fujii for their constructive comments and suggestions not only on this dissertation but also on annual evaluations.

I would like to thank Prof. (Assoc.) Tetsuya Tokoro, who taught me technique and useful trick in unsaturated tests. I want to express my sincere thanks Prof. (Assoc.) Koichi Isobe and Prof. (Asst.) Shoji Yokohama for their big support and advices. Research supports, valuable data provided by Dr. Kimio Maruyama and the Civil Engineering Research Institute for Cold Region make validation and verification for this study possible

I am also greatly indebted to Dr. Nguyen Binh Thanh, Dr. Yulong Zhu, and Dr. Jiaqiang Yang who were always forwarded to help me during experiments and encourage me when I were depressed. I grateful acknowledge to the students of Laboratory of Analytical Geomechniacs for their help during these three years.

This research was made possible through the financial support of the China Scholarship Council.

Finally, my special thanks are extended to my beloved parents, family, and friends. Without their encouragement and confidence in me all through these years, it would not be possible for me to arrive in Japan and complete my doctoral study at Hokkaido University.

TABLE OF CONTENTS

ABSTRACT I
ACKNOWLEDGEMENT IV
TABLE OF CONTENTS V
LIST OF FIGURES VII
LIST OF TABLES IX
1 INTRODUCTION 1
1.1 BACKGROUND 1
1.2 LITERATURE REVIEW 4
1.2.1 Resilient modulus 4
1.2.2 Rutting failure models 5
1.3 THESIS OBJECTIVES 7
1.4 THESIS ORGANIZATION 8
2 APPARATUS AND MATERIAL FOR RESILIENT MODULUS TEST 10
2.1 FREEZE-THAW TRIAXIAL APPARATUS 10
2.2 MEDIUM-SIZE TRIAXIAL APPARATUS 11
2.3 TEST MATERIAL 13
3 RESILIENT MODULUS TEST METHOD 15
3.1 LOADING CONDITION IN MR TEST 15
3.2 TEST SEQUENCE 17
3.3 CLIMATE AND WHEEL LOADING CONDITIONS 20
3.3.1 Suction process 20
3.3.2 Freezing and thawing process 21
3.3.3 Wheel loads process 22
4 PROPOSAL OF A MODIFIED CLIMATE MODEL 24
4.1 RESILIENT MODULUS TEST RESULTS 24
4.1.1 Effects of loading frequency 24
4.1.2 Effects of matric suction 26
4.1.3 Effects of freeze-thaw action 32
4.1.4 Effects of wheel loads 32
4.2 A MODIFIED CLIMATE MODEL 35
4.2.1 Applicability of EICM 35

4.2.2 Modified Ng model 36
4.3 APPLICATION TO JAPANESE PAVEMENT DESIGN GUIDE 39
4.3.1 Fatigue life analysis of asphalt pavement 39
4.3.2 Loading frequency effect on fatigue life of the pavement 44
4.3.3 Climate effect on fatigue life of the pavement 45
4.4 SUMMARY 46
5 EFFECT OF PRINCIPAL STRESS AXIS ROTATION ON RUTTING 48
5.1 MATERIALS AND MULTI-RING SHEAR TESTING PROGRAM 48
5.2 DEPENDENCY OF PERMANENT STRAIN ON SHEAR STRENGTH 51
5.3 PROPOSAL AND APPLICATION OF MODIFIED UIUC MODEL 56
5.4 MODEL IMPLEMENTATION FOR PREDICTING RUTTING DEPTH OF FLEXIBLE PAVEMENT 66
5.5 SUMMARY 69
6 MODIFICATION OF PAVEMENT DESIGN METHOD 70
6.1 TEST PAVEMENTS 70
6.1.1 Pavement structures 70
6.1.2 Traffic volume observation 71
6.1.3 Climate data 71
6.1.4 Predicted fatigue life with present Japanese design guide 72
6.2 VARIANT LAYER MODULI 73
6.2.1 Climate effect 73
6.2.2 Stress state 85
6.2.3 Climate effect on fatigue life 91
6.3 MODIFICATION OF FAILURE CRITERIA 94
6.3.1 MEPDG rutting prediction model 94
6.3.2 Principal stress axis rotation 97
6.4 SUMMARY 103
7 FINDING AND ASSIGNMENT 105
7.1 FINDING 105
7.2 ASSIGNMENT 106
REFERENCES 108
NOTATIONS 113

LIST OF FIGURES

Figure 1-1 Three-layers model for allowable loading number calculation 1
Figure 1-2 Sequence in current Japanese flexible pavement design guide 3
Figure 1-3 Flowchart of this study 9
Figure 2-1 Freeze-thaw triaxial apparatus 11
Figure 2-2 Medium-size triaxial apparatus 13
Figure 2-3 Soil-water characteristic curves of Toyoura sand 14
Figure 3-1 Loading wave in (a) this study, (b) AASHTO standard 16
Figure 3-2 Volume of water drainage and axial displacement during freeze-thaw process 19
Figure 3-3 Resilient modulus of unfrozen and freeze-thawed specimens 20
Figure 3-4 Pavement structure used in GAMES to determine wheel loads 23
Figure 4-1 Average resilient modulus ratio under different matric suction conditions 24
Figure 4-2 Frequency effect under different matric suction conditions 25
Figure 4-3 Resilient modulus of U test under saturated and unsaturated condition 27
Figure 4-4 Resilient modulus of UW test under saturated and unsaturated condition 28
Figure 4-5 Resilient modulus of FT test under saturated and unsaturated condition 29
Figure 4-6 Resilient modulus of FTW test under saturated and unsaturated condition 30
Figure 4-7 Resilient modulus of FWT test under saturated and unsaturated condition 31
Figure 4-8 Axial strain and Secant Young's modulus during wheel loads process in FWT test 34
Figure 4-9 Axial strain and Secant Young's modulus during wheel loads process in FTW test 35
Figure 4-10 Fitting surfaces of FT test results through (a) EICM (b) modified Ng model 38
Figure 4-11 Cross section used in GAMES 40
Figure 4-12 Test pavement structures 40
Figure 4-13 Long-term field measured degree of saturation of subgrade layer 43
Figure 4-14 Loading frequency effect on fatigue life against rutting 45
Figure 4-15 Climate effect on fatigue life against rutting 46
Figure 5-1 Multi-ring shear apparatus (after Ishikawa et al., 2011) 50
Figure 5-2 Relations between permanent, resilient axial strain, shear strength 53
Figure 5-3 Shear stress-strain curve in monotonic shearing test 55
Figure 5-4 Estimation of the permanent axial strain of C-9.5 58
Figure 5-5 Estimation of the permanent axial strain of RC-9.5 59

Figure 5-6 Estimation of the permanent strain of C-9.5 and RC-9.5 with fixed A, B, C, D ... 62
Figure 5-7 Stress paths involves principal stress axis rotation ... 65
Figure 5-8 Synergistic effect of principal stress axis rotation and change in moisture content ... 66
Figure 5-9 Games model for stress analysis ... 67
Figure 5-10 Computation of rutting depth using modified UIUC model ... 69
Figure 6-1 Test pavement structures ... 71
Figure 6-2 Average monthly representative air temperature ... 72
Figure 6-3 Predicted fatigue life through current Japanese design guide ... 73
Figure 6-4 (a) Field measured base course water content and (b) SWCC of C-40 ... 75
Figure 6-5 (a) Field measured subgrade layer water content and (b) SWCC of Toyoura sand 76
Figure 6-6 Resilient modulus of C-40 under different water contents ... 78
Figure 6-7 7 Resilient modulus of Toyoura sand under different water contents ... 79
Figure 6-8 Estimated freeze-thawed C-40 resilient modulus with (a) modified Ng model and (b) modified Liang model ... 82
Figure 6-9 Freeze-thaw resilient modulus of Toyoura sand under different water contents ... 84
Figure 6-10 Stress states calculation points in base and subgrade layer ... 86
Figure 6-11 Iteration of resilient modulus of (a) base layer and (b) subgrade layer ... 87
Figure 6-12 Convergent (a) Resilient modulus and (b) stress states in different sections ... 89
Figure 6-13 Convergence analysis effect on fatigue life under (a) water content fluctuation condition (b) climate effect condition ... 91
Figure 6-14 Fatigue life against rutting of eight test pavement structures ... 93
Figure 6-15 Fatigue life against cracking of eight test pavement structures ... 93
Figure 6-16 Allowable loading number calculated through AI and MEPDG model ... 95
Figure 6-17 Predicted and actual rutting failure loading number ... 96
Figure 6-18 Effect of convergence analysis on N_{fs} ... 97
Figure 6-19 Permanent axial strain of Toyoura sand ... 98
Figure 6-20 Stress states calculation point in subgrade layer ... 100
Figure 6-21 Stress states in different depth ... 102
Figure 6-22 Predicted rutting failure loading number considering principal stress axis rotation ... 102
Figure 6-23 Sequence in modified Japanese flexible pavement design guide ... 103

LIST OF TABLES

Table 3-1 Loading conditions of MR tests 16
Table 3-2 Test sequence for U, UW, FT, FTW, and FWT test 18
Table 4-1 Regression analysis results through Ng model 31
Table 4-2 Applicability of EICM and modified Ng models 36
Table 4-3 Monthly representative elastic moduli of subgrade layer 43
Table 5-1 Experimental conditions of multi-ring shear tests for aggregate 51
Table 5-2 Regression analysis results with Duncan-Chang model 55
Table 5-3 Results of regression analysis through modified UIUC model 57
Table 5-4 Results of regression analysis through modified UIUC model with fixed parameters 60
Table 6-1 Value of regression constants through Ng model 79
Table 6-2 Monthly representative layer moduli considering fluctuating water contents 79
Table 6-3 Applicability of Modified Liang model and Modified Ng model on C-40 83
Table 6-4 Applicability of Modified Liang model and Modified Ng model on Toyoura sand 85
Table 6-5 Monthly representative subgrade layer moduli considering climate effect 85
Table 6-6 Convergent monthly representative base/subgrade layer moduli in A section 88
Table 6-7 Experimental conditions of multi-ring shear tests for Toyoura sand 97

1 INTRODUCTION

1.1 BACKGROUND

Japanese design guide [Japan Road Association, 2006] provides fatigue failure criteria, as shown in Equations (1-1) and (1-2), to calculate allowable loading number of equivalent 49-kN wheel loads against rutting (N_{fs}) and fatigue cracking (N_{fa}), which are calculated by a theoretical design method, also known as AI model, [Asphalt Institute, 1982] using a simplified three-layers model which consists of asphalt mixture layer (hereafter referred to as the "As layer"), base layer, and subgrade layer as shown in Figure 1-1.

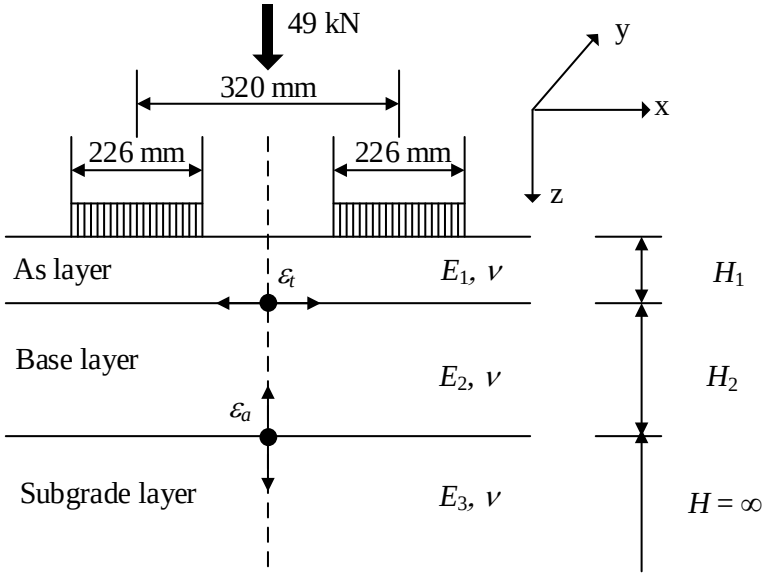

Figure 1-1 Three-layers model for allowable loading number calculation

$$N_{fs} = \beta_{s1} \cdot \left\{1.365 \times 10^{-9} \cdot {\varepsilon_a}^{-4.477 \cdot \beta_{s2}}\right\} \quad (1\text{-}1.1)$$

$$\beta_{s1} = 2134 \quad (1\text{-}1.2)$$

$$\beta_{s2} = 0.819 \quad (1\text{-}1.3)$$

$$N_{fa} = \beta_{a1} \cdot C_a \cdot \left\{6.167 \times 10^{-5} \cdot {\varepsilon_t}^{-3.291 \cdot \beta_{a2}} \cdot {E_1}^{-0.854 \cdot \beta_{a3}}\right\} \quad (1\text{-}2.1)$$

$$C_a = 10^M \quad (1\text{-}2.2)$$

$$M = 4.84 * \left(\frac{VFA}{100} - 0.69\right) \quad (1\text{-}2.3)$$

$$\beta_{a1} = K_a * {\beta_{a1}}' \quad (1\text{-}2.4)$$

$$K_a = \begin{cases} \frac{1}{8.27\times10^{-11}+7.83\cdot e^{-0.11H_a}}, & H_1 < 0 \\ 1, & H_1 \geq 0 \end{cases} \quad (1\text{-}2.5)$$

$$\beta_{a1}{}' = 5.229 \times 10^4 \quad (1\text{-}2.6)$$

$$\beta_{a2} = 1.314 \quad (1\text{-}2.7)$$

$$\beta_{a3} = 3.018 \quad (1\text{-}2.8)$$

where β_{s1}, β_{s2}, β_{a1}, β_{a2}, and β_{a3} are the compensation rates for AI failure criteria based on the actual situation of Japanese pavement; C_a is the material parameter; K_a is a correction factor, which relates to the thickness of asphalt mixture, H_1. ε_a is the compressive strain on the top surface of the subgrade layer; ε_t is the tensile strain on the lower surface of the As layer.

ε_a and ε_t are determined through multi-layers model, which involves elastic moduli (E) and Poisson's ratio (v) of each layer, built in General Analysis of Multi-layered Elastic Systems (GAMES) [Maina and Matsui, 2004] as shown in Fig 1-1. In present Japanese design guide, elastic moduli of As layer (E_1) changes with temperature as shown in Equation (1-3), while the elastic moduli of base layer (E_2) and subgrade layers (E_3) are constant throughout a whole year since lacking investigation of how moisture content, freeze-thaw, or stress states influence E_2 and E_3.

$$E_1 = -278.4M_p + 10930 \quad (1\text{-}3.1)$$

$$M_p = M_a\left[1 + \frac{2.54}{h_1+10.16}\right] - \frac{25.4}{9(h_1+10.16)} + \frac{10}{3} \quad (1\text{-}3.2)$$

where M_p is the monthly mean temperature of asphalt mixture at depth of h_1 (℃); M_a is monthly mean air temperature (℃); h_1 is the depth equals to one-third of the height of asphalt mixture (cm).

Consequently, monthly representative E_1 and constant E_2/E_3 are used to calculate allowable loading number under monthly average temperature condition, $N_{fs.i}$ and $N_{fa.i}$. i=1~12. Failure loading number $N_{fs.d}$ or $N_{fa.d}$ is calculated through Equations (1-4) and (1-5).

$$N_{f.d} = \frac{1}{D_a} \quad (1\text{-}4)$$

$$D_a = \frac{1}{12}\sum_{i=1}^{12}\frac{1}{N_{f.i}} \quad (1\text{-}5)$$

As a result, Fig. 1-2 illustrates the sequence in current Japanese flexible pavement design guide.

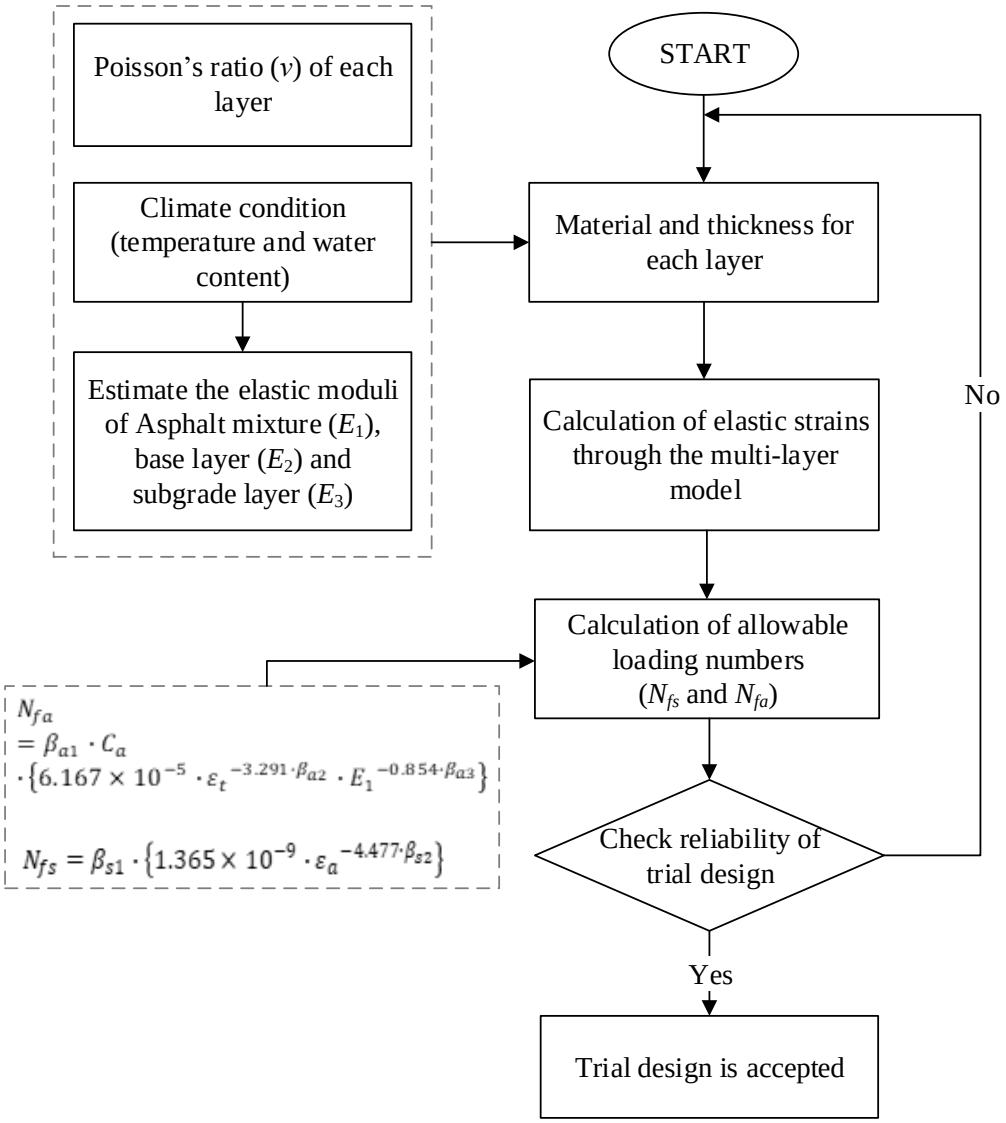

Figure 1-2 Sequence in current Japanese flexible pavement design guide

Several serious drawbacks limit the applicability and accuracy of present fatigue failure criteria shown here. First, only elastic moduli of base and subgrade layer are used while the effect of stress states on layer stiffness is not considered. Furthermore, effects of moisture content and freeze-thaw action, which greatly influence the stiffness of base and subgrade layer [Berg et al., 1996; Cole et al., 1981; Johnson et al., 1978; Simonsen et al., 2002; Simonsen and Isacsson, 2001], are also not considered here. On the other hand, current rutting failure criterion (Equation (1-1)) is limited that it provides no indication of the behavior of rutting over time or with the application of traffic loading. It also does not provide any indication of rate-hardening, nor does it consider the contribution of the non-subgrade layers to rutting. Besides, the effect of principal stress axis rotation (PSAR), a phenomenon caused by moving wheel loads and greatly amplified the permanent deformation of base and subgrade layer [Miura et al., 1986; Brown,

1996; Gräbe and Clayton, 2009; Inam et al., 2012; Ishikawa et al., 2011, 2019b] is also ignored now.

1.2 LITERATURE REVIEW

1.2.1 Resilient modulus

Resilient modulus (M_r), originally proposed by Seed [1955], is capable to capture the effect of stress states on the stiffness of soil, and widely used in Mechanistic-Empirical Pavement Design Guide (MEPDG) as shown in Equation (1-6) [AASHTO, 2008]. Generally speaking, the resilient modulus decreases with increasing deviator stress and decreasing confining pressure.

$$M_r = k_1 p_a \left(\frac{\theta}{p_a}\right)^{k_2} \left(\frac{\tau_{oct}}{p_a} + 1\right)^{k_3} \quad (1\text{-}6)$$

where k_1, k_2, k_3 are regression constants; p_a is atmospheric pressure and set as 101 kPa in this study; θ is bulk stress (kPa); τ_{oct} is octahedral shear stress (kPa).

However, effects of moisture content and freeze-thaw action, which greatly influence the stiffness of base and subgrade layer [Berg et al., 1996; Cole et al., 1981; Johnson et al., 1978; Simonsen et al., 2002; Simonsen and Isacsson, 2001], are not considered in universal model (Equation (1-6)). In snowy cold regions such as Hokkaido, a northern island in Japan, pavement structures suffer annually freeze-thaw cycles as the 0°C isotherm may penetrate deep into the pavement. Freeze-thaw action deteriorates pavement structures in two ways as frost-heave and thaw-weakening. Swelling of soil during freezing conditions caused by an increasing presence of ice lens finally leads to cracking in As layer. Thaw-weakening means a drop of base and subgrade layer strength and stiffness caused by suddenly rising water content, which comes from the inflow of snowmelt water or the thawing of ice lenses, and deteriorates uniformity of particle skeleton structure after freeze-thaw action [Jong et al., 1998; Simonsen and Isacsson, 1999]. To be precise, rising water content, as a result of the inflow of water during rainfall or the thawing of ice lenses, causes a temporary decrease in the stiffness of base course and subgrade material. Meanwhile, freeze-thaw action always decreases moduli of base and subbase layer materials even with no excess water storage after thawing, as ice formation tends to break some of the particle contacts and interlocking of soil particles and finally deteriorates the soil structure uniformity and stiffness.

To overcome such shortcoming, several models [Cary and Zapata, 2011; Liang et al., 2008; Ng et al., 2013] are proposed based on the universal model. Within these models, Ng model

shown in Equation (1-7) adds an independent stress state variable that incorporates matric suction effects into the universal model and shows good applicability on predicting resilient modulus of unsaturated unbound granular materials through the relatively higher coefficient of determination (R^2) value than other models [Han and Vanapalli, 2016].

$$M_r = k_1 p_a \left(\frac{\theta}{p_a}\right)^{k_2} \left(\frac{\tau_{oct}}{p_a} + 1\right)^{k_3} \left(\frac{\psi}{\sigma_{net}} + 1\right)^{k_4} \quad (1\text{-}7)$$

where k_1, k_2, k_3, k_4 are regression constants; p_a is atmospheric pressure; θ is bulk stress; τ_{oct} is octahedral shear stress; σ_{net} is net mean stress (kPa), defined as [$\boldsymbol{\theta}$ /3-u_a]; ψ is matric suction (kPa).

MEPDG also suggests a model, named as EICM (Enhanced Integrated Climatic Model) (NCHRP, 2004), to capture the freeze-thaw effect on M_r as shown in Equation (1-8). This model adds a new factor, F_{env}, on the universal model (Equation (1-6)) to represent the reduction of M_r due to freeze-thaw. F_{env} is a reduction factor defined by the ratio of M_r for freeze-thawed soil divided by M_r for unfrozen soil.

$$M_r = F_{env} \cdot k_1 p_a \left(\frac{\theta}{p_a}\right)^{k_2} \left(\frac{\tau_{oct}}{p_a} + 1\right)^{k_3} \quad (1\text{-}8)$$

Ishikawa et al. [2019a] examine the climate effect on the resilient deformation characteristics of base course materials through a series of resilient modulus tests on base course materials under various water contents. However, climate effect on the resilient deformation characteristics of subgrade materials has not been fully studied.

1.2.2 Rutting failure models

To overcome the limitations of AI model that no indication of the behavior of rutting over time or with the application of traffic loading, MEPDG proposed a rutting depth prediction model [NCHRP, 2004], which converts the plastic strain measured from the laboratory to the field condition, as shown in Equation (1-9). The strain ratio, $\varepsilon_p/\varepsilon_v$, in the equation is a function of the layer modulus for different traffic levels. Assuming values for $\varepsilon_p/\varepsilon_v$ at different loading number, N=1 and N=10^9, to calculate the a_1, b_1, a_9, and b_9 values and a_1=0.15, b_1=0, a_9=20, and b_9=0 are "universal" constants obtained from national calibrations.

$$\varepsilon_p(N) = \beta_1 \left(\frac{\varepsilon_0}{\varepsilon_r}\right) e^{-\left(\frac{\rho}{N}\right)^{\beta}} \varepsilon_v \quad (1\text{-}9.1)$$

$$\frac{\varepsilon_0}{\varepsilon_r} = \left[\left(e^{(\rho)^{\beta}} a_1 E^{b_1}\right) + \left(e^{\left(\frac{\rho}{10^9}\right)^{\beta}} a_9 E^{b_9}\right)\right]/2 = \left[\left(e^{(\rho)^{\beta}} * 0.15\right) + \left(e^{\left(\frac{\rho}{10^9}\right)^{\beta}} * 20\right)\right]/2 \quad (1\text{-}9.2)$$

$$\log\beta = -0.61119 - 0.017638 W_c \quad (1\text{-}9.3)$$

$$\rho = 10^9\left(\frac{C_0}{1-(10^9)^{\beta}}\right)^{\frac{1}{\beta}} = 10^9\left(\frac{-4.89285}{1-(10^9)^{\beta}}\right)^{\frac{1}{\beta}} \quad (1\text{-}9.4)$$

$$C_0 = \ln\left(\frac{a_1 * E^{b_1}}{a_9 * E^{b_9}}\right) = -4.89285 \quad (1\text{-}9.5)$$

where $\varepsilon_p(N)$ is permanent strain for the layer/sub-layer; N is number of traffic repetitions; ε_0, β, and ρ are material properties; ε_r is resilient strain imposed in laboratory test to obtain material properties ε_0, β, and ρ; ε_v is average vertical resilient strain in the layer, which is calculated by a multi-layer elastic pavement response model; β_1 is calibration factor for the unbound granular and subgrade materials; E is resilient modulus; W_c is water content.

On the other hand, MEPDG rutting model does not capture the effect of principal stress axis rotation (PSAR), a phenomenon caused by moving wheel loads and greatly amplified the permanent deformation of base and subgrade layer [Miura et al., 1986; Brown, 1996; Gräbe and Clayton, 2009; Inam et al., 2012; Ishikawa et al., 2011, 2019b], since it is built on traditional repeated loading triaxial test with constant confining pressure and no principal stress axis rotation. To simulate the in-situ stress state in the pavement, Ishikawa et al. [2007] developed a multi-ring shear apparatus for laboratory element tests, which could apply cyclic axial stress and shear stress simultaneously. Furthermore, the NCHRP Project 4-23 pointed out that shear strength but not resilient modulus is one of the most significant mechanical properties influencing pavement performance [Saeed et al., 2001]. Then, the K-T model (Equation (1-10)) [Korkiala-Tanttu, 2009] and UIUC model (Equation (1-11)) [Chow et al., 2014a] use shear strength to construct a predictive model. As a result, the UIUC model shows high accuracy on permanent strain prediction. However, the applicability of UIUC model on materials with variant water contents has not been checked since it is built on test results only with optimum moisture content. Besides, effect of principal stress axis rotation is also not considered in this model. Due to the author, applied deviator stress term is enough to capture the effects of stress levels with constant confining pressure and the effect of confining pressure is indirectly reflected in the calculation for mobilized shearing resistance. Effect of shear strength on permanent deformation is considered by incorporating the *SSR* term. Due to Chow et al. [Chow et al., 2014b], The effects of moisture content on permanent deformation accumulation are not considered because their tests were conducted at optimum moisture content - maximum dry density conditions. Therefore, the accuracy of UIUC model on predicting permanent deformation of aggregates with different moisture content is not verified and the effect of PSAR on permanent deformation is also ignored.

$$\varepsilon_p = C_k N^b \frac{R}{1-R} \quad (1\text{-}10.1)$$

$$b = d\left(\frac{q}{q_f}\right) + c' \quad (1\text{-}10.2)$$

$$R = \frac{q}{q_f} = \frac{\sigma_1 - \sigma_3}{q_o + Mp} \quad (1\text{-}10.3)$$

$$q_o = c\frac{6cos\phi}{3-sin\phi} \quad (1\text{-}10.4)$$

$$M = \frac{6sin\phi}{3-sin\phi} \quad (1\text{-}10.5)$$

where ε_p is the permanent vertical strain; C_k is the permanent strain in the first loading cycle; N is the number of loading cycles; b is the shear ratio parameter depending on the material (Equation (1-10.2)); R is the shear failure ratio (Equation (1-10.3)); q is deviator stress; q_f is the deviator stress in failure; q_0 is the deviator stress when p' equals to zero; c is the cohesion; ϕ is friction angle; M is the slope of the failure line in p'-q space in triaxial test; c' and d are material parameters.

$$\varepsilon_p(N) = AN^B \quad (1\text{-}11.1)$$

$$\varepsilon_p(N) = AN^B {\sigma_d}^C \left(\frac{\tau_f}{\tau_{max}}\right)^D \quad (1\text{-}11.2)$$

$$SSR = \frac{\tau_f}{\tau_{max}} \quad (1\text{-}11.3)$$

$$\tau_f = \sqrt{(\sigma_d/2)^2 - [\sigma_f - (\sigma_3 + \sigma_d/2)]^2} \quad (1\text{-}11.4)$$

$$\sigma_f = \frac{2\sigma_3(1+tan^2\phi) + \sigma_d(1+tan^2\phi) - \sqrt{{\sigma_d}^2 tan^2\phi(1+tan^2\phi)}}{2(1+tan^2\phi)} \quad (1\text{-}11.5)$$

$$\tau_{max} = c + \sigma_f tan\phi \quad (1\text{-}11.6)$$

where $\varepsilon_p(N)$ is permanent strain corresponding to N-load applications; σ_d is applied deviator stress; SSR is shear stress ratio; τ_f is mobilized shearing resistance acting on failure plane; σ_f is normal stress acting on failure plane; τ_{max} is available shear strength obtained through Mohr-Coulomb failure criteria; A to D: regression parameters.

1.3 THESIS OBJECTIVES

To overcome aforementioned limitations, this study modified the present Japanese design guide through two main aspects as 1. Replacing constant base course and subgrade layer elastic modulus to resilient modulus related to stress states and complex climate conditions, it is

defined as the combination of fluctuating water content and freeze-thaw action; 2. Modifying rutting failure criterion structure by considering generally used MEPDG model and also the effect of principal stress axis rotation.

First, this study examines and evaluates the climate effect on resilient modulus of subgrade material through a series of suction-controlled resilient modulus tests (hereafter referred to as the "MR test") with variant freeze-thaw, wheel loads, and water contents conditions.

Second, this study attempts to develop a simple mathematical model of the mechanical response of base course and subgrade materials subjected to variant stress and climate condition, in order to establish a method for evaluating the long-term performance of the unbound granular material layer at pavement structures in cold regions.

Third, this study modified the structure of AI model referring to MEPDG rutting model to improve the applicability and precision of fatigue life prediction.

Last, this study utilizes multi-ring shear test results to examine the amplification of permanent deformation caused by principal stress axis rotation. Such effect is applied to modify the structure of rutting failure criterion used in AI model and UIUC model.

1.4 THESIS ORGANIZATION

Figure 1-2 illustrates the flowchart of this study to show the relation among all chapters. Chapter 1 introduces the background, objective, and organization of this study. Chapter 2 gives the detail of test apparatus, like freeze-thaw triaxial apparatus and medium-size triaxial apparatus, and test material used for resilient modulus test used in this study. Chapter 3 describes the test methods and experimental conditions of resilient modulus test under complex combination of matric suction, freeze-thaw action, and wheel loads. Chapter 4 presents the resilient modulus test results obtained in this study. A modified constitutive model is proposed to capture the synergistic effect between water contents and freeze-thaw action on resilient modulus of subgrade material. Chapter 5 discussed the effect of principal stress axis rotation on permanent deformation of specimen based on previous multi-ring shear test. Chapter 6 gives a modified pavement design guide comes from laboratory element test results shown in Chapter 4 and 5. Predicted fatigue life through modified design method is compared with long-term performance observation data to check the applicability. Chapter 7 summarizes the conclusion obtained in this study.

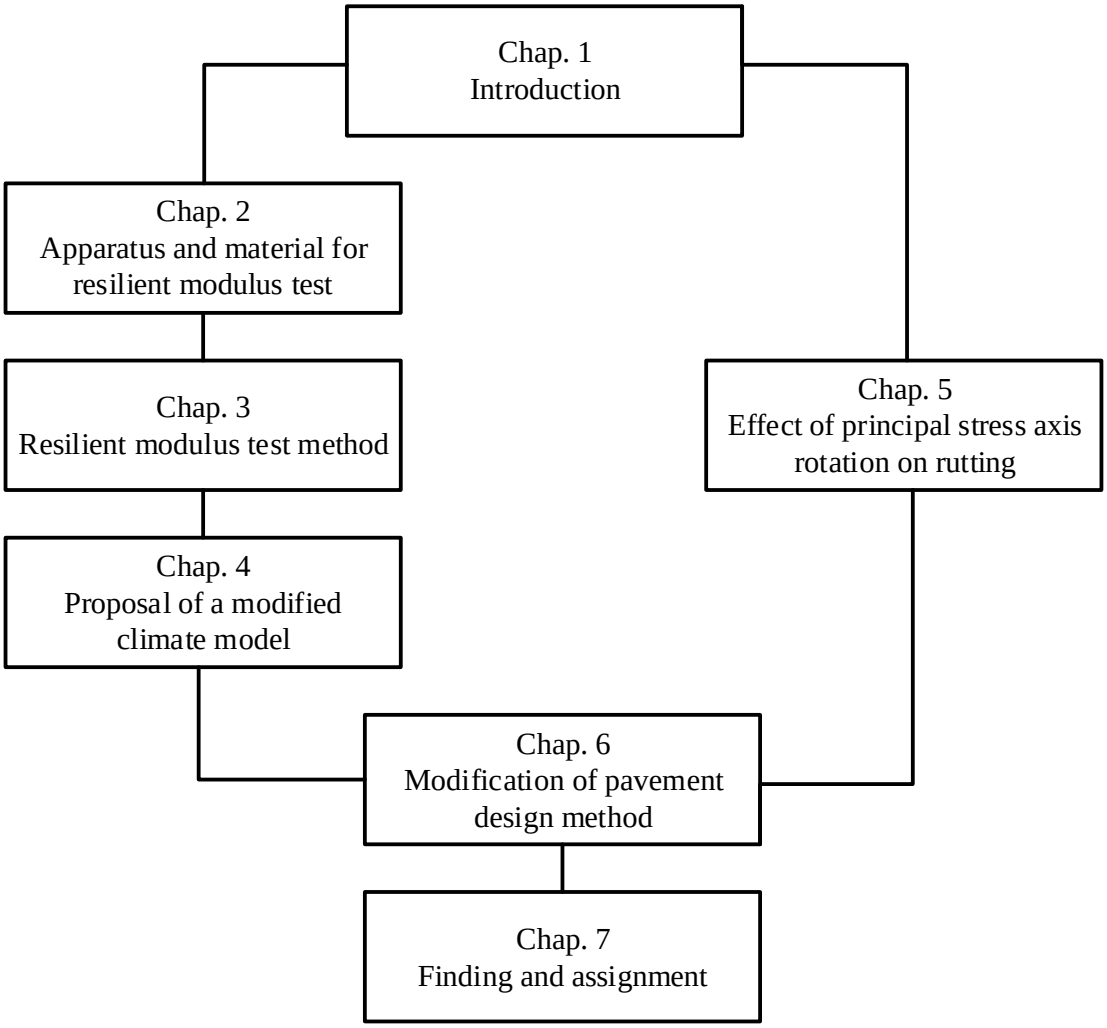

Figure 1-3 Flowchart of this study

2 APPARATUS AND MATERIAL FOR RESILIENT MODULUS TEST

2.1 FREEZE-THAW TRIAXIAL APPARATUS

Figure 2-1 illustrates the schematic diagram of the apparatus used in this study, which consists of a cyclic triaxial test apparatus that can apply cyclic axial loads, and three low-temperature baths which could circulate low-temperature fluids (antifreeze) in the cap, pedestal, and inner cell to control the temperature separately. The size of the specimen is 170 mm in height and 70 mm in diameter. The apparatus can apply the matric suction (ψ) by controlling pore-water pressure (u_w) from the pedestal end and pore-air pressure (u_a) from the cap end (Figure 2-1 (b) and (c)). It is noted that resilient modulus test under variant climate conditions, that is combination of unsaturated condition and freeze-thaw action, are performed through this apparatus. Test method will be explained in next chapter.

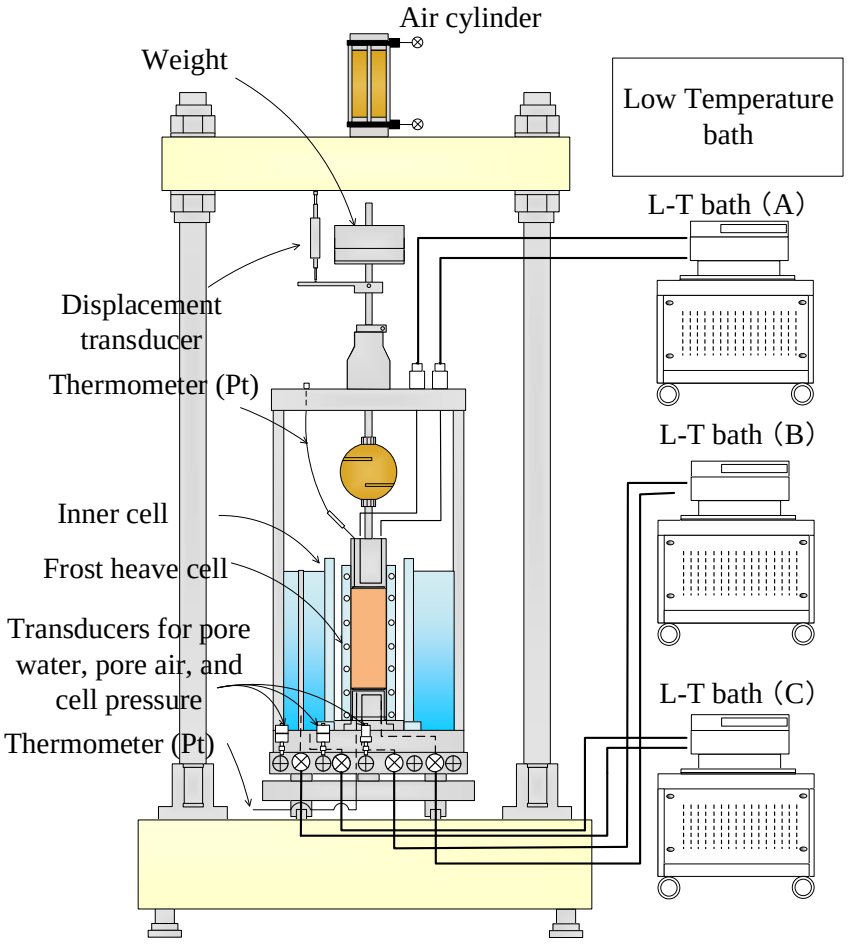

(a) Schematic diagram of freeze-thaw triaxial apparatus

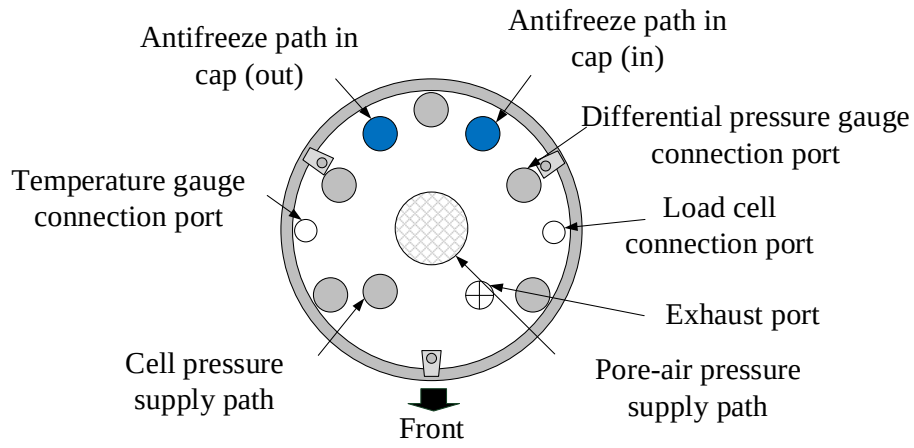

(b) Structual design of cap

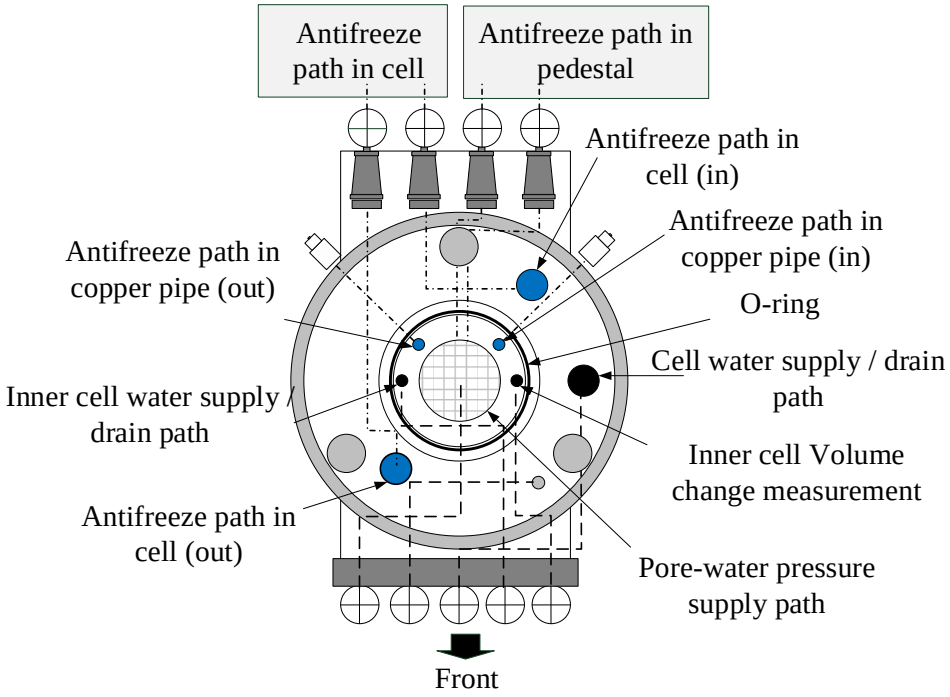

(c) Structural design of pedestal

Figure 2-1 Freeze-thaw triaxial apparatus

2.2 MEDIUM-SIZE TRIAXIAL APPARATUS

A schematic diagram of a suction-controlled medium-size triaxial apparatus for unsaturated soils is shown in Figure 2-2. One key feature of the apparatus is the structural design of the cap and pedestal as shown in Figure 2-2 (b). Here, the versapor membrane filter is a kind of microporous membrane filters made from hydrophilic acrylic copolymer, and polyflon filter is a hydrophobic filter made from polytetrafluoroethylene. Accordingly, the

apparatus adopts the pressure membrane method. The apparatus can apply axial load to a specimen with high accuracy by both strain-controlled method and stress-controlled method with a hybrid actuator. Moreover, the apparatus can perform both monotonic loading tests with very slow loading rate, and cyclic loading tests in which the maximum frequency of cyclic loading is up to about 10 Hz. Since freeze-thaw triaxial apparatus could only apply cyclic load with 0.2 Hz, which is lower than the recommended 10 Hz in AASHTO standard. Medium-size triaxial apparatus will be used to perform resilient modulus test to check the applicability of freeze-thaw triaxial apparatus and study the effect of loading frequency on resilient modulus.

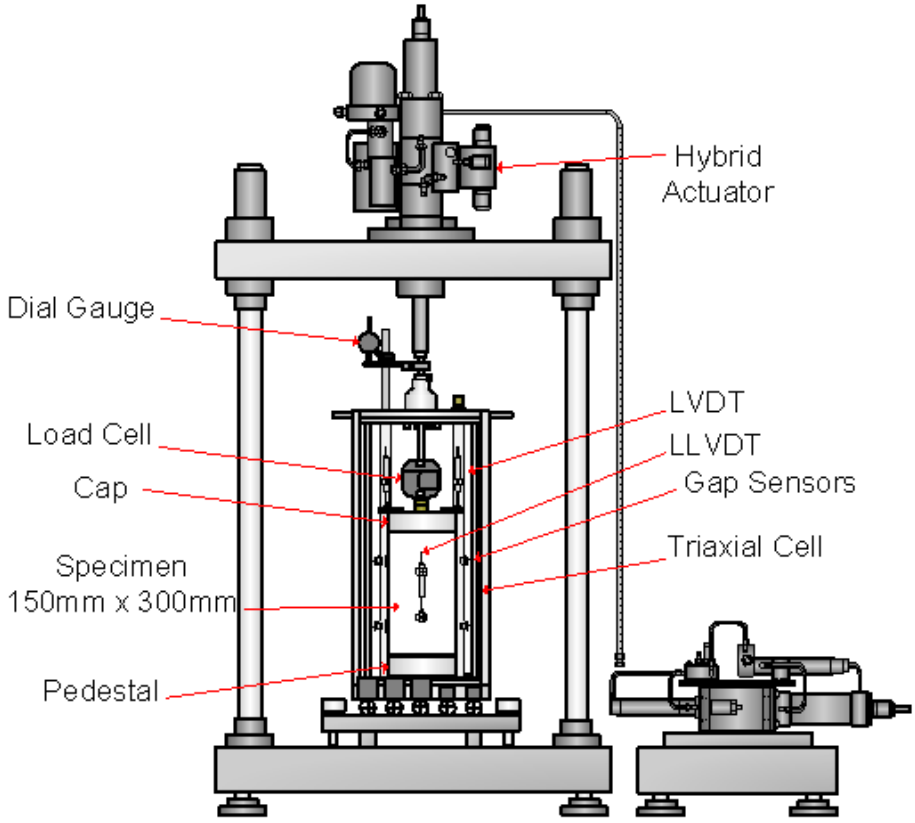

(a) Schematic diagram of test apparatus

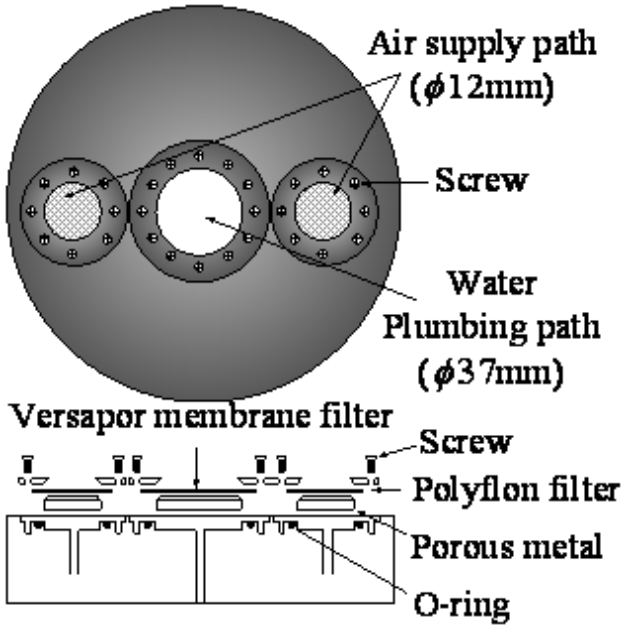

(b) Structural design of cap and pedestal

Figure 2-2 Medium-size triaxial apparatus

2.3 TEST MATERIAL

Toyoura sand is a type of Japanese standard sand, employed as the test material in this study and laboratory element tests by many other researchers. As a non-frost-susceptible material, it is classified as a poorly graded sand (SP) according to ASTM classification. Specimens were prepared by air pluviation method and the degree of compaction is 96% and dry density (ρ_d) is 1.58 g/cm^3 to satisfy the pavement subgrade layer standard provided by Japanese Ministry of Land, Infrastructure, Transport and Tourism [Japan Road Association, 2006].

Figure 2-3 shows the soil-water characteristic curve (SWCC) of Toyoura sand obtained from this apparatus. The SWCC of this soil is S-shaped with an inflection point where the matric suction increased as the volumetric water content decreased, and the shape qualitatively matches the results of previous studies [Ishikawa et al., 2014a]. Besides, the difference in SWCCs between a freeze-thawed specimen and an unfrozen specimen can hardly be recognized. This phenomenon is originated in no particle breakage due to freeze-thaw action, which led to little change in the water retentivity and permeability before and after freeze-thawing [Ishikawa et al., 2016]. Fitting curve for unfrozen specimen through Fredlund and Xing model [1994] is also displayed in the figure.

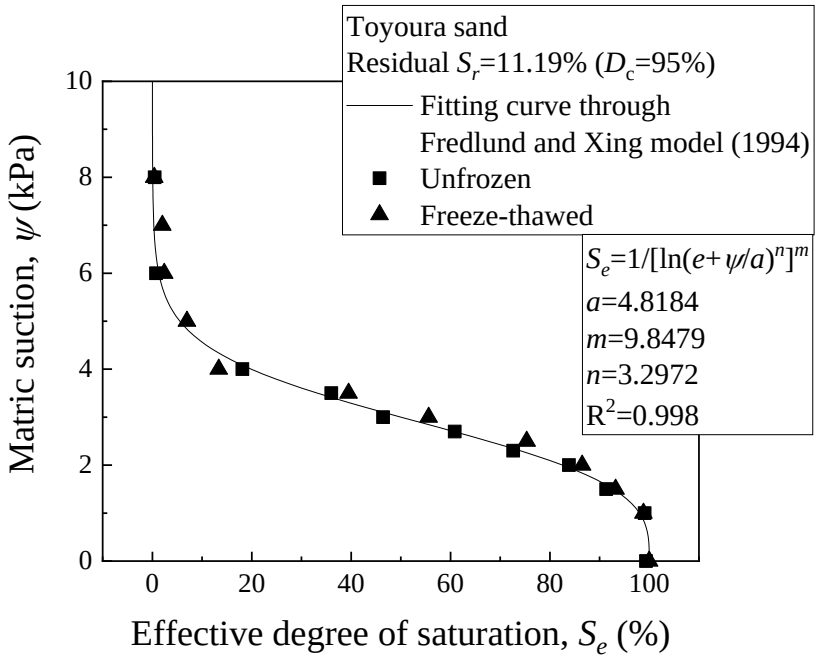

Figure 2-3 Soil-water characteristic curves of Toyoura sand

3 RESILIENT MODULUS TEST METHOD

3.1 LOADING CONDITION IN MR TEST

Resilient modulus is especially important in mechanistic pavement design procedure and considerable researches had been conducted since Seed et al. [1955] proposed the concept of resilient modulus as the ratio of the amplitude of cyclic deviator stress to the amplitude of the resultant recoverable axial strain. In this study, MR test is performed according to AASHTO test standard T307-99 [AASHTO, 2003]. Due to the limitation of the apparatus, this study applied loading pulse with a frequency of 0.2 Hz (Figure3-1 (a)), which is different from the AASHTO standard haversine-shaped loading pulse with a frequency of 10 Hz (Figure3-1 (b)). According to the measured loading data, it is recognized that haversine-shaped load was almost reproduced though the frequency is much lower than the recommended value in AASHTO standard. Examination of this limited loading frequency would be discussed in the latter part.

(a) Loading wave in this study

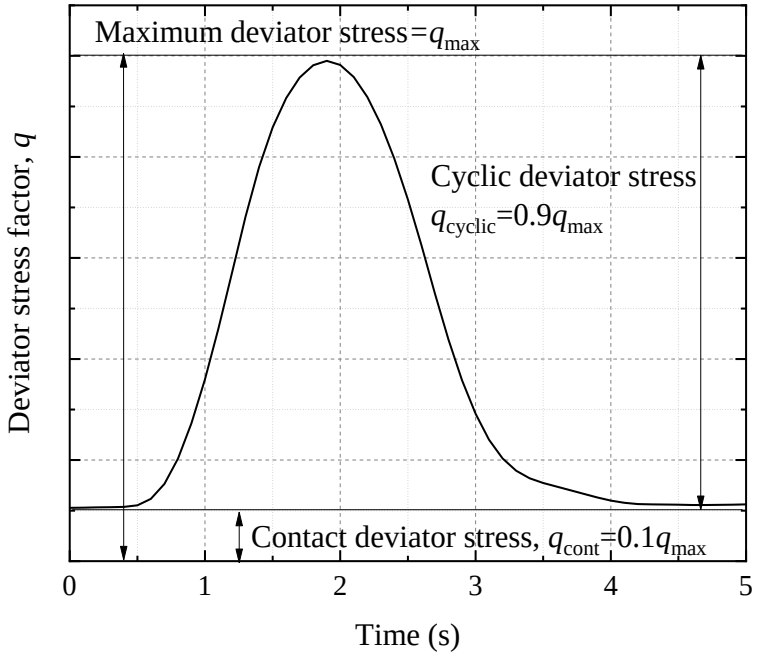

(b) Loading wave in AASHTO study

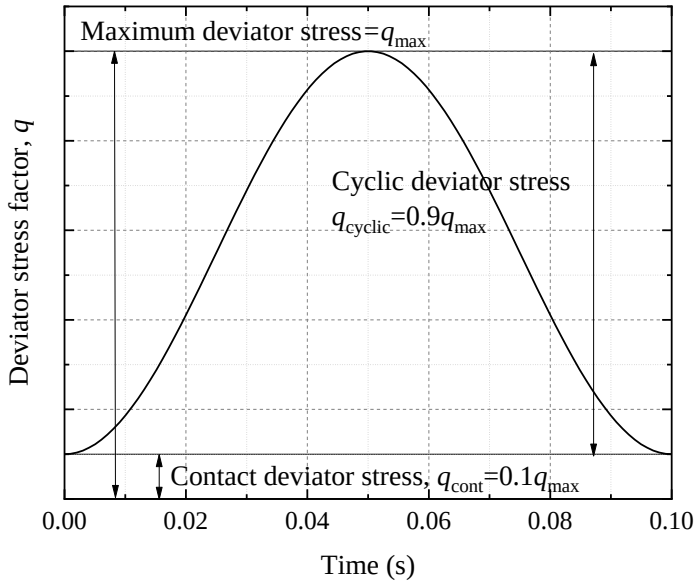

Figure 3-1 Loading wave in (a) this study, (b) AASHTO standard

AASHTO standard has 11 loading steps as MR-0 to MR-10. According to the AASHTO standard, MR-0 aims to make sure the cap completely reaches specimen top end. For this reason, this study prolonged the loading number from 1000 cycles to 2000 cycles to ensure a stable residual strain after MR-0. Besides, the vertical stress in stage MR-4, 5, 9, and 10 are significantly larger than the stress measured at the actual situation in Japan [Kishikawa et al., 2017]. The overstress in MR-4, 5 increased the relative density and the results of MR- 6, 7, 8 cannot be evaluated accurately [Aoki et al., 2018]. To sustain the relative density, this study skipped MR-4, 5, 9, and 10 and inserted MR-1.5, 2.5, 6.5, and 7.5 to keep the total test step as 11. Table 3-1 lists details of applied stress, like confining pressure (σ_c), maximum deviator stress (q_{max}), constant deviator stress to keep positive contact between the cap and the specimen (q_{const}), cyclic deviator stress (q_{cyclic}), and the loading number (N_c). Figure 3-1 illustrates the definitions of q_{max}, q_{cont}, and q_{cyclic} in one loading cycle.

Table 3-1 Loading conditions of MR tests

Name	σ_c (kPa)	q_{max} (kPa)	q_{cont} (kPa)	q_{cyclic} (kPa)	N_c
MR-0	41.4	27.6	2.76	24.84	2000
MR-1	41.4	13.8	1.38	12.42	100
MR-1.5	41.4	20.7	2.07	18.63	100
MR-2	41.4	27.6	2.76	24.84	100

MR-2.5	41.4	34.5	3.45	31.05	100
MR-3	41.4	41.4	4.14	37.26	100
MR-6	27.6	13.8	1.38	12.42	100
MR-6.5	27.6	20.7	2.07	18.63	100
MR-7	27.6	27.6	2.76	24.84	100
MR-7.5	27.6	34.5	3.45	31.05	100
MR-8	27.6	41.4	4.14	37.26	100

3.2 TEST SEQUENCE

This study designed five types of MR test named as Unfrozen test (hereafter referred to as the "U test"), Unfrozen-Wheel loads test (hereafter referred to as the "UW test"), Freeze-Thaw test (hereafter referred to as the "FT test"), Freeze-Thaw-Wheel loads test (hereafter referred to as the "FTW test"), and Freeze-Wheel loads-Thaw test (hereafter referred to as the "FWT test"). Each test was conducted under saturated and unsaturated conditions. It is noted that, U tests measure M_r of subgrade material at unfrozen status which simulates normal season. UW tests condition aims to simulate subgrade material suffered wheel loads at the normal season. FT tests, applied one-dimensional freeze-thaw action on specimen before MR test, aim to detect the resilient modulus just after freeze-thaw action. FTW tests, by applying additional wheel loads process after freeze-thaw action, could simulate a subgrade material suffered wheel loads at thawing season. FWT tests, by applying additional wheel loads process between freeze-thaw action, could simulate a subgrade material suffered wheel loads at the freezing season. All tests start with a fully saturated specimen, by confirming the pore pressure coefficient is 0.96 or more. In this study, a fully saturated specimen for test under saturated condition is prepared as follows: (1) Supplying CO_2 to replace the air in the specimen. (2) Supplying de-aired water through the specimen. As this study uses filter method and axis translation technique to prepare unsaturated specimen from a saturated condition, CO_2 could not be supplied in the specimen. Saturation process for test under unsaturated condition is prepared as follows: (1) Supplying de-aired water through the specimen. (2) Applying back pressure of 200 kPa step by step. The u_w, u_a, and σ_c are 200, 200, and 220 kPa at the end. Table 3-2 summarizes the sequence of each test. For example, the most complicated test, FWT test in unsaturated condition, is performed as follows: (1) Applying consolidation process. Within this process, predetermined consolidation stress of 41.4 kPa, which is the same as the highest confining pressure in the MR test (AASHTO, 2003), is applied on the specimen. The u_w, u_a, and σ_c are set as 200, 200, and 241.4 kPa according to the 200 kPa back pressure. (2) Applying suction process to obtain an unsaturated specimen.

This process is carried out by decreasing u_w while keeping u_a, and σ_c constant. (3) Applying freezing process by lowering specimen temperature. (4) Applying wheel loads process with predetermined cyclic deviator stress. (5) Applying thawing process by raising specimen temperature. (6) Performing MR test. More details like test technique for unsaturated specimen preparation, stress state during wheel loads process, and temperature conditions applied during freeze-thaw process are explained in the next section. It is noted that suction process is applied prior to freezing process in FT, FTW, and FWT tests under unsaturated condition as shown in Table 3-2. This sequence means matric suction is under control during the whole freeze-thaw action, which involves a high level of experimental skill.

Table 3-2 Test sequence for U, UW, FT, FTW, and FWT test

Test name	Test sequence													
	Consolidation process		Suction process		Freezing process		Wheel loads process		Thawing process		Wheel loads process		MR test	
U	→	○	→	○/×	→	×	→	×	→	×	→	×	→	○
UW	→	○	→	○/×	→	×	→	×	→	×	→	○	→	○
FT	→	○	→	○/×	→	○	→	×	→	○	→	×	→	○
FTW	→	○	→	○/×	→	○	→	×	→	○	→	○	→	○
FWT	→	○	→	○/×	→	○	→	○	→	○	→	×	→	○

Note: ○means Applied this progress; × means Skipped this progress.

Another simpler test sequence named as freeze-thaw unsaturated test applies freeze-thaw action on a saturated specimen and controls matric suction after freeze-thaw action. Compared with unsaturated freeze-thaw test, freeze-thaw unsaturated test is far from the actual situation as the subgrade layer hardly to be saturated in winter.

Figure 3-2 shows the volume of water drainage, axial displacement, the temperature of cap and pedestal during the freeze-thaw action. For an unsaturated specimen, the volume of water drainage variates around 0 ml during freeze-thaw process, which is quite different with a saturated specimen. A saturated specimen would drain about 25 ml water when it is frozen. This difference is quite reasonable because a 9% volumetric expansion of water will happen with the formation of ice and water will be squeezed out when the specimen is saturated. However, for an unsaturated specimen, as the existence of air voids, formation of ice may just occupy these voids. Another noticeable difference is axial displacement. Axial displacement of

saturated specimen decreased about 1 mm when it is frozen, which equals to specimen height increased 1 mm. However, when the freeze-thaw action is applied to an unsaturated specimen, there is no increase of the specimen height. At the end of freeze-thaw, unsaturated specimen shows a little bit larger settlement, which causes a relatively higher density and lower void ratio. This difference may cause different mechanical properties.

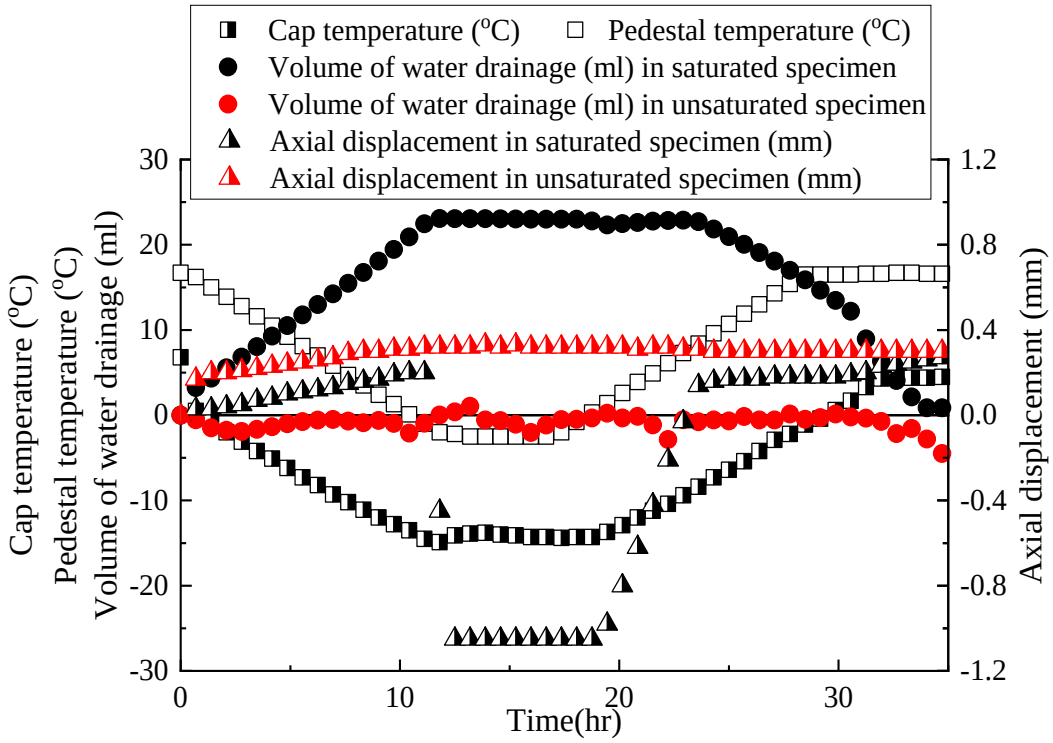

Figure 3-2 Volume of water drainage and axial displacement during freeze-thaw process

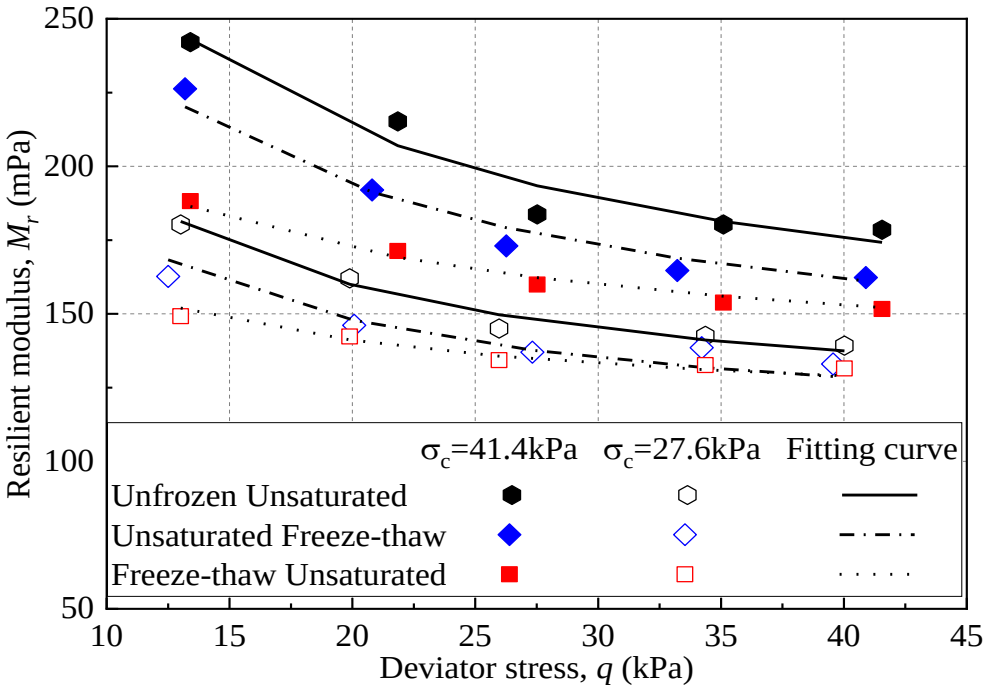

Figure 3-3 Resilient modulus of unfrozen and freeze-thawed specimens

The resilient modulus of the unsaturated freeze-thawed specimen is shown in Figure 3-3. It shows a good dependency of deviator stress and confining pressure. The resilient modulus decreases with larger deviator stress and smaller confining pressure. As shown in Figure 3-3, unfrozen unsaturated Toyoura sand shows higher resilient modulus. It is reasonable to conclude that, the freeze-thaw action decreases the resilient modulus even though the matric suction is kept as the same value before and after the freeze-thaw. Moreover, the resilient modulus of the freeze-thaw unsaturated specimen is the lowest among all tests results, which implies that a decreasing of resilient modulus caused by freeze-thaw is strongly related to the water content before frozen. More water contents exist in a specimen when the freeze-thaw action is applied, the resilient modulus decreases more significantly after a freeze-thaw action.

Consequently, this study applied suction process prior to freezing process as it better reproduces the actual situation that subgrade material meets during freezing season.

3.3 CLIMATE AND WHEEL LOADING CONDITIONS

3.3.1 Suction process

As mentioned in the Introduction part, to examine and evaluate the climate effect on M_r of subgrade material, a series of suction-controlled MR test with two kinds of water content,

saturated and unsaturated, under variant freeze-thaw history and wheel loads condition are performed. The unsaturated specimen used in this study has a 40% degree of saturation, equals to 16% volumetric water content, as the long-term field measurement data [Ishikawa et al., 2012] of the volumetric water content of a subgrade layer in Hokkaido is about 16%. According to SWCC of Toyoura sand, the matric suction (ψ) is set as 3.75 kPa by axis translation technique [Fredlund and Morgenstern, 1977] to obtain this unsaturated specimen. Suction process starts from the fully saturated and isotropic consolidated condition by decreasing pore-water pressure in steps, while keeping both confining pressure and pore-air pressure constant. A decrease of pore-water pressure means an increase of matric suction, which causes the drainage of pore-water from the specimen. Upon attaining an equilibrium condition, the drainage is stopped. The above-described procedure is then repeated for a higher value of matric suction, ψ, until 3.75 kPa to finally obtain an unsaturated specimen. It is noted that, stress condition in Table 3-1 is used in the saturated condition, based on a total stress approach in which the triaxial system measures the mechanical response of the material subjected to different combinations of cyclic deviator stress (q_{cyclic}) and confining pressures (σ_c). From the unsaturated soil mechanics perspective, the air phase becomes important in the measurement and control of matric suction and the total stress is replaced by the net normal stress [Cary and Zapata, 2011], which is the difference between the total stress and the pore-air pressure (σ-u_a). By using the axis translation technique, the confining pressure becomes the net confining pressure (σ_c- u_a) and the axial stress, σ_a, becomes the net axial stress (σ_a- u_a). This approach does not affect the way the deviator stress is defined since the air pressure will affect σ_a and σ_c in the same proportion. Consequently, stress value in Table 3-1 is the same for an unsaturated test when the confining pressure becomes the net confining pressure.

3.3.2 Freezing and thawing process

Temperatures of cap and pedestal during freeze-thaw process are shown in Figure 3-2. One-dimensional freeze-thaw action is achieved in the following steps. The initial temperature of cap and pedestal were set and kept to 0 ℃ and 16.8 ℃ respectively and a frost heave cell is mounted to restrict the radial deformation during freeze-thaw process. The thermal shock is applied at the top end of the specimen prior to freezing to avoid supercooling. Then, the temperature of cap and pedestal are lowered to -18.9 ℃ and -2.1 ℃ respectively with a constant cooling rate of 1.67 ℃/hr. In the similar way as the previous research [Aoki et al., 2018], a constant cooling rate of 1.67 ℃/hr is used in this study to avoid supercooled state, caused by too large rate, or excessive test time, caused by too small rate. Next, the temperature of cap and

pedestal are kept for 5 hours to ensure the uniformity of unfrozen water. The thawed status is achieved by raising the temperature of cap and pedestal to 5 ℃ and 16.8 ℃ with a heating rate of 1.67 ℃/hr. Open-system freeze-thaw process is used in this test by opening the pedestal water plumbing path during the freeze-thaw process, which means the specimen could drain in or out water freely. Referring to JGS 0172-2009 [Japanese Geotechnical Society, 2009], applied axial stress during the freeze-thaw process is set as 10 kPa.

3.3.3 Wheel loads process

The wheel loads in this study could be classified as three types: loads on the unfrozen specimen (UW test), loads on the frozen specimen (FWT test), and loads on the thawed specimen (FTW test). Loading cycles of wheel loads in UW, FTW, and FWT tests are 1000 times. Loading frequency and pulse shape are same with them in MR test loading (Figure 3-1 (a)). Constant deviator stress (q_{const}) and cyclic deviator stress (q_{cyclic}) during wheel loads process should be determined through an appropriate method to simulate actual stress state of the subgrade layer during normal or freezing seasons. General Analysis of Multi-layered Elastic Systems (GAMES) [Maina and Matsui, 2004] is used to determine the q_{const} and q_{cyclic} on the subgrade layer caused by a 49-kN wheel load on a typical pavement structure in the Japanese design guide. Figure 3-4 illustrates the pavement structure and parameters like Young's modulus, E, and Poisson's ratio, v, used in this study. These values come from the Japanese design guide recommended value [Japan Road Association, 2006]. It is noted that these moduli are rough estimated values, which may have a large difference with in-situ measured data. Besides, the design guide sets moduli of base, subbase, and subgrade layers as constant, which implies a necessity of modification. A modification with variant E caused by climate effect will be realized and introduced in the latter part. According to GAMES calculation results, the q_{const} and q_{cyclic} of wheel loads process in UW and FTW, which simulate wheel loads in normal and thawing season, are set as 9.6 and 26.2 kPa. The q_{const} and q_{cyclic} of wheel loads process in FWT, which simulate wheel loads in freezing season, are set as 9.6 and 24.5 kPa. In FWT test, removing frost heave cell before applying wheel loads process is necessary as it restricts the specimen in a radial direction. Then, a copper pipe, which could circulate antifreeze, is installed around the specimen to keep the frozen status during the whole wheel loads process. When the wheel loads process is finished, the copper pipe is removed, and the thawing period is started.

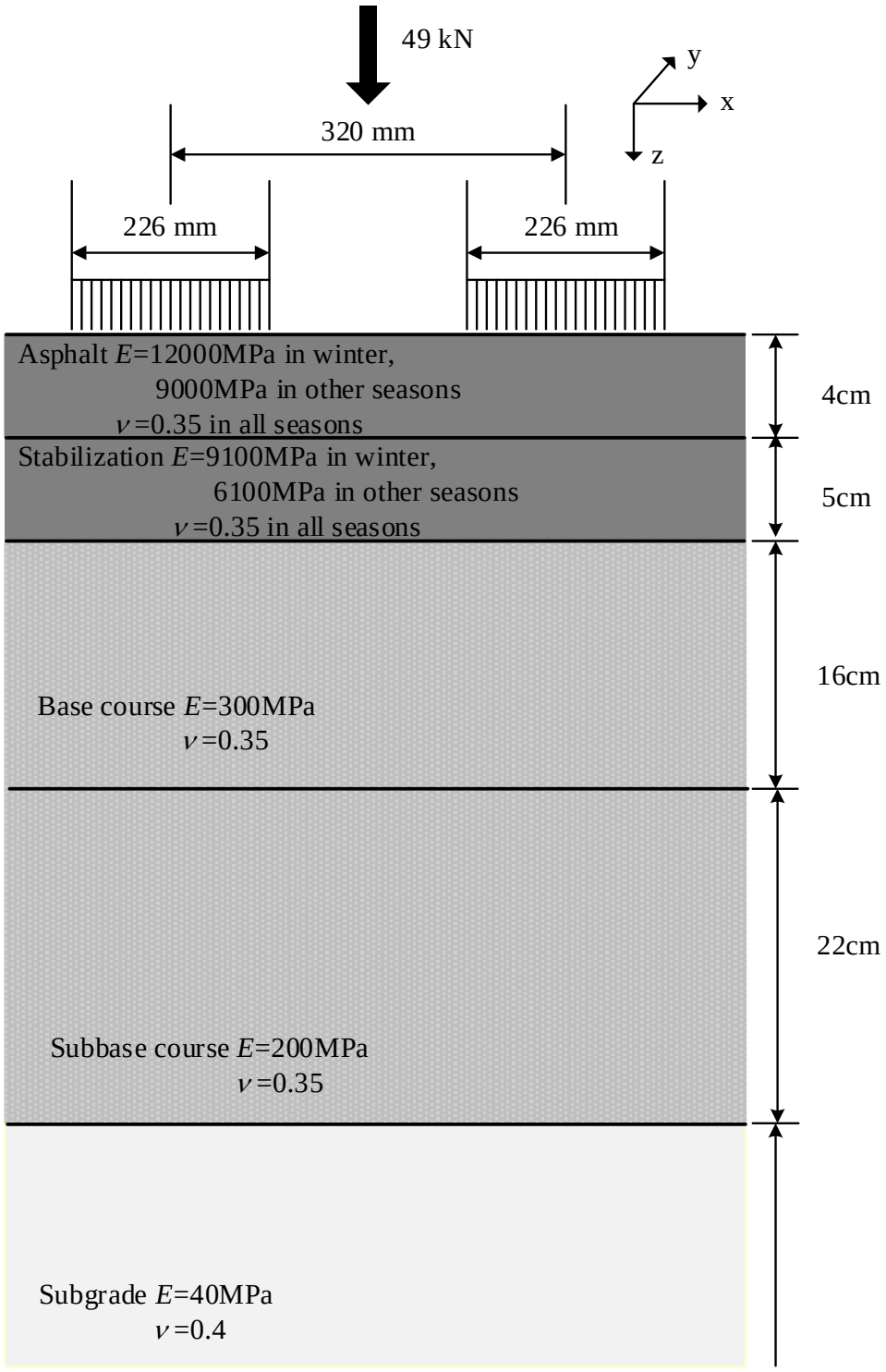

Figure 3-4 Pavement structure used in GAMES to determine wheel loads

4 PROPOSAL OF A MODIFIED CLIMATE MODEL

4.1 RESILIENT MODULUS TEST RESULTS

4.1.1 Effects of loading frequency

Examining the influence of loading frequency is necessary to check the reliability of test results, and the usefulness and generality of the proposed testing method, as the loading frequency used in AASHTO standard is 10 Hz. Toyoura sand specimens with three water content (40%, 70%, and 100% degree of saturation, matric suction for such degree of saturation is 3.75kPa, 3 kPa, and 0 kPa respectively) are prepared to perform MR test with two different apparatus, freeze-thaw triaxial apparatus and medium-size triaxial apparatus. Medium-size triaxial apparatus could apply loading frequencies of 10 Hz. Figure 4-1 plots the average resilient modulus ratio between M_r of MR-1 to MR-8 with high frequency and low frequency under different matric suction conditions. The fitting curve shown in Figure 4-1 is obtained through Equations (4-2) and (4-3) and will be explained later. First of all, all ratios are higher than 1, means that higher loading frequency always leads to a higher modulus regardless of the degree of saturation. Figure 4-1 also illustrates that matric suction influences the average resilient modulus ratio between different loading frequencies. To be precise, the average resilient modulus ratio increases with ψ, which also implies that the frequency effect is more significant for a specimen with higher matric suction.

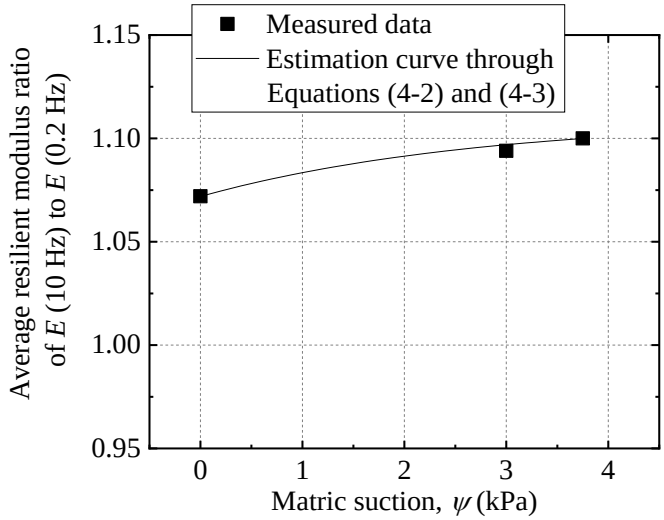

Figure 4-1 Average resilient modulus ratio under different matric suction conditions

Equation (4-1) was proposed to quantitively describe the frequency effect on the resilient modulus (Kim et al., 1997).

$$\frac{E(f)}{E(0.5\ Hz)} = 1 + F(\psi) * Log(f) \quad (4\text{-}1)$$

where f is loading frequency; $E(0.5\ Hz)$ is resilient modulus obtained at f=0.5 Hz; $E(f)$ is predicted resilient modulus at any frequency, f; $F(\psi)$ is referred as the frequency effect, which is affected by matric suction, ψ.

Based on Equation (4-1), the average resilient modulus ratio between 10 Hz and 0.2 Hz could be expressed as follows:

$$\frac{E(10\ Hz)}{E(0.2\ Hz)} = \frac{\frac{E(10\ Hz)}{E(0.5\ Hz)}}{\frac{E(0.2\ Hz)}{E(0.5\ Hz)}} = \frac{1+F(\psi)*Log(10)}{1+F(\psi)*Log(0.2)} = \frac{1+F(\psi)}{1-0.6989F(\psi)} \quad (4\text{-}2)$$

Based on Equation (4-2) and measured average resilient modulus ratio, the value of $F(\psi)$ under three matric suction values could be determined as shown in Figure 4-2.

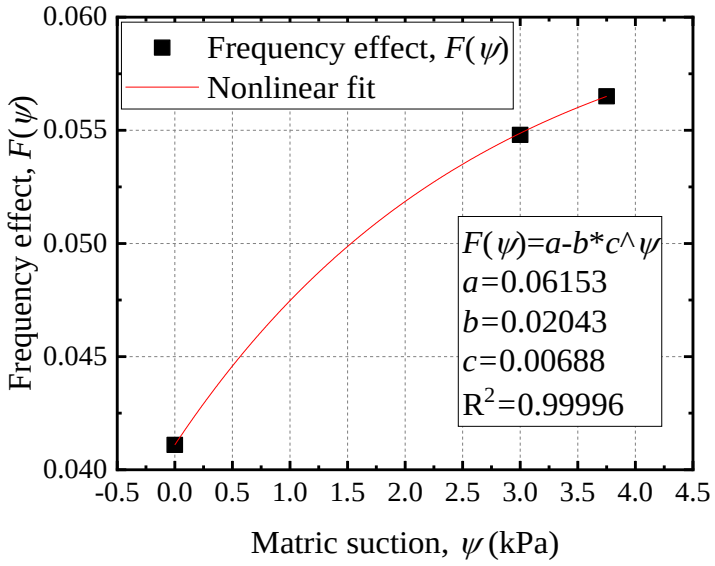

Figure 4-2 Frequency effect under different matric suction conditions

A nonlinear equation ($F(\psi)=a-b*c^{\psi}$) is chosen as the fitting model because it would not meet such question that $F(\psi)$ increases to an unrealistic level when the ψ is extremely large. Besides, parameters in this nonlinear equation have a clearer physical meaning. When ψ goes to an infinite value or zero, $F(\psi)$ equals to a or a-b. As a result, a means upper limit of $F(\psi)$ and a-b means $F(\psi)$ when the specimen is fully saturated. Substituting fitted frequency effect,

$F(\psi)$, into Equation (4-2), predicted average resilient modulus ratio with high accuracy could be obtained (see the black line in Figure 4-1).

Consequently, M_r obtained through freeze-thaw triaxial apparatus with limited loading frequency could be converted to general AASHTO standard M_r through Equations (4-2) and (4-3).

$$F(\psi) = 6.15343 - 2.04343 * 0.68826^{\psi} \quad (4\text{-}3)$$

4.1.2 Effects of matric suction

Aiming to quantitively analyze the effect of stress state, freeze-thaw action, matric suction on the M_r, this study performs regression analysis with Ng model (Equation (1-7)) to obtain the value of k_1, k_2, k_3, k_4 from a series of MR tests and investigate how freeze-thaw action and fluctuating water content affect these values. Figures 4-3 to 4-7 illustrate M_r of U, UW, FT, FTW, and FWT test respectively. The red dot is measured M_r and the fitting surface is obtained through Ng model. It is noted that these results are converted data through Equations (4-2) and (4-3) and seen as general AASHTO standard resilient modulus. Table 4-1 lists regression analysis results through Ng model. Regression analysis here is performed regardless of the degree of saturation. In other words, saturated and unsaturated U tests are treated as one group to perform regression analysis. UW, FT, FTW, and FWT tests are regression analyzed in the same method. High R^2 value validates the applicability of Ng model.

It is well known that M_r highly relates to stress variables. To be specific, M_r increases with lower deviator stress (q) or higher confining pressure (σ_c) and matric suction (ψ). This is because a higher σ_c leads to increasing of frictional force, which helps resist soil deformation. This trend could be found during all test results as shown in Figure 4-3 to 4-7. As shown in Figures 4-3 to 4-7, all unsaturated tests have a higher M_r than saturated tests regardless of freeze-thaw and wheel loads history. Additionally, M_r obtained from unsaturated specimen through all tests has a more slanting surface, in other words, q and σ_c have a more significant influence on the M_r when the specimen is unsaturated. Consequently, suddenly rising water content, induced by the inflow of snowmelt water and the thawing of ice lenses at thawing season or heavy rainfall at summertime, greatly degrades the subgrade layer stiffness.

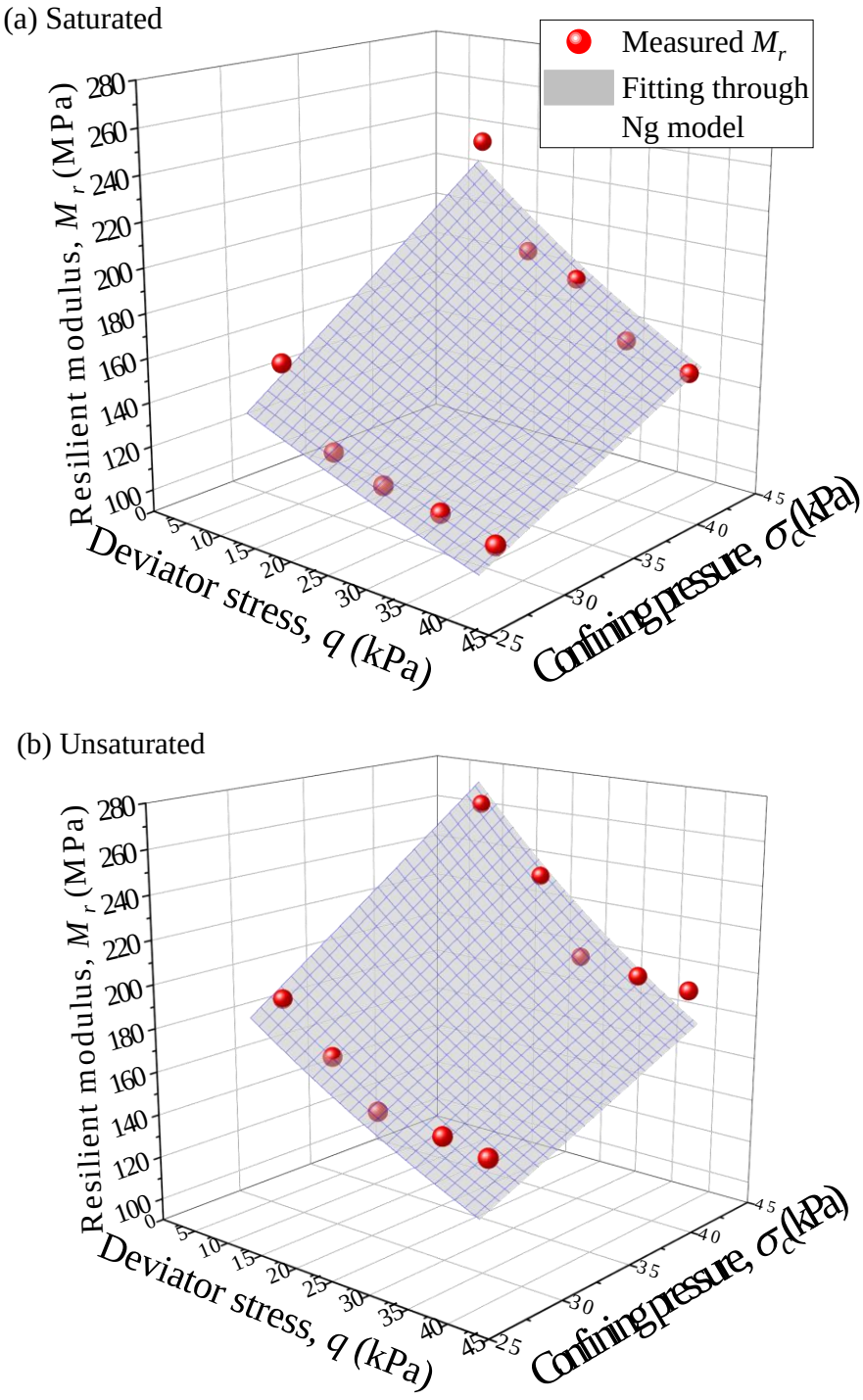

Figure 4-3 Resilient modulus of U test under saturated and unsaturated condition

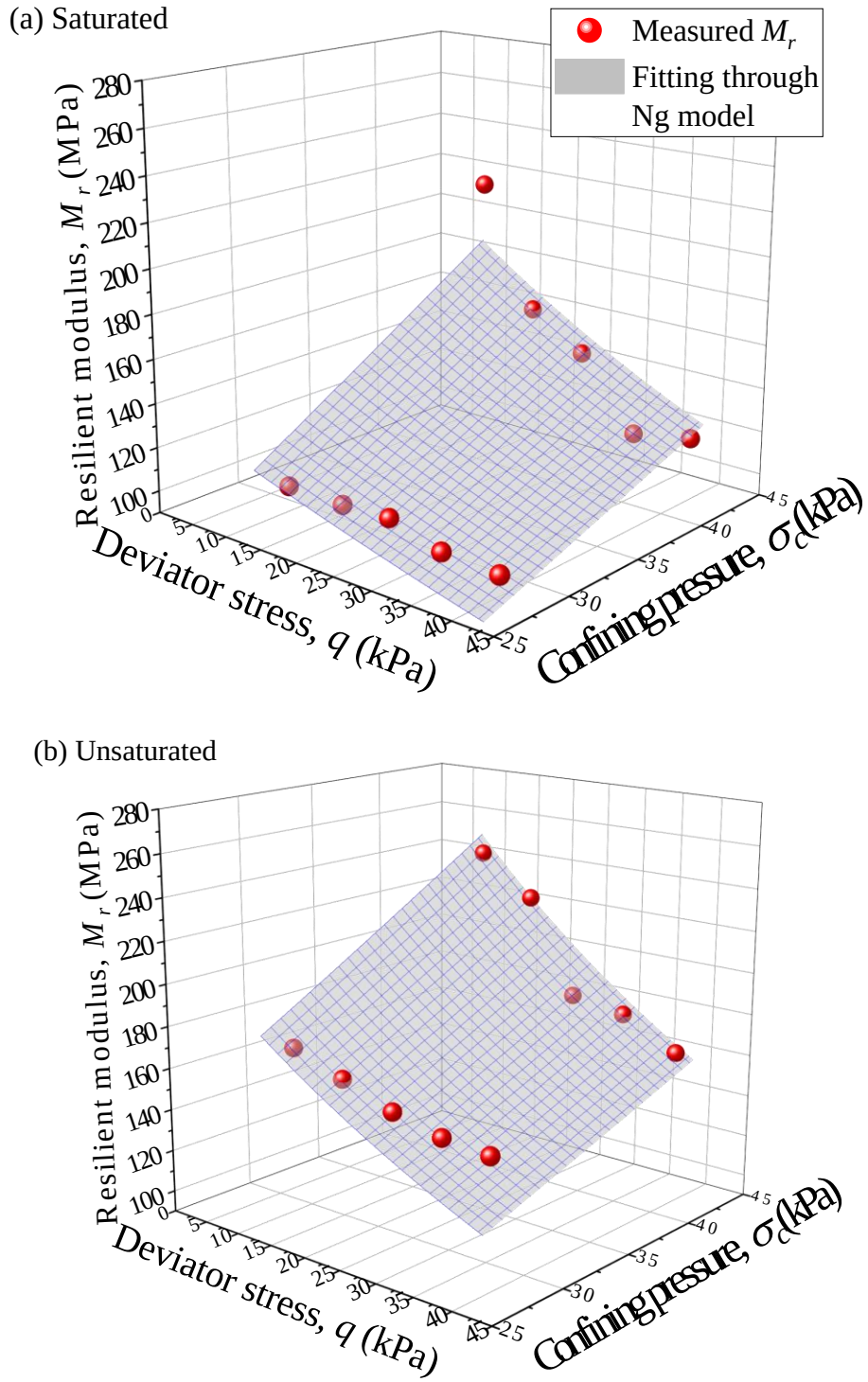

Figure 4-4 Resilient modulus of UW test under saturated and unsaturated condition

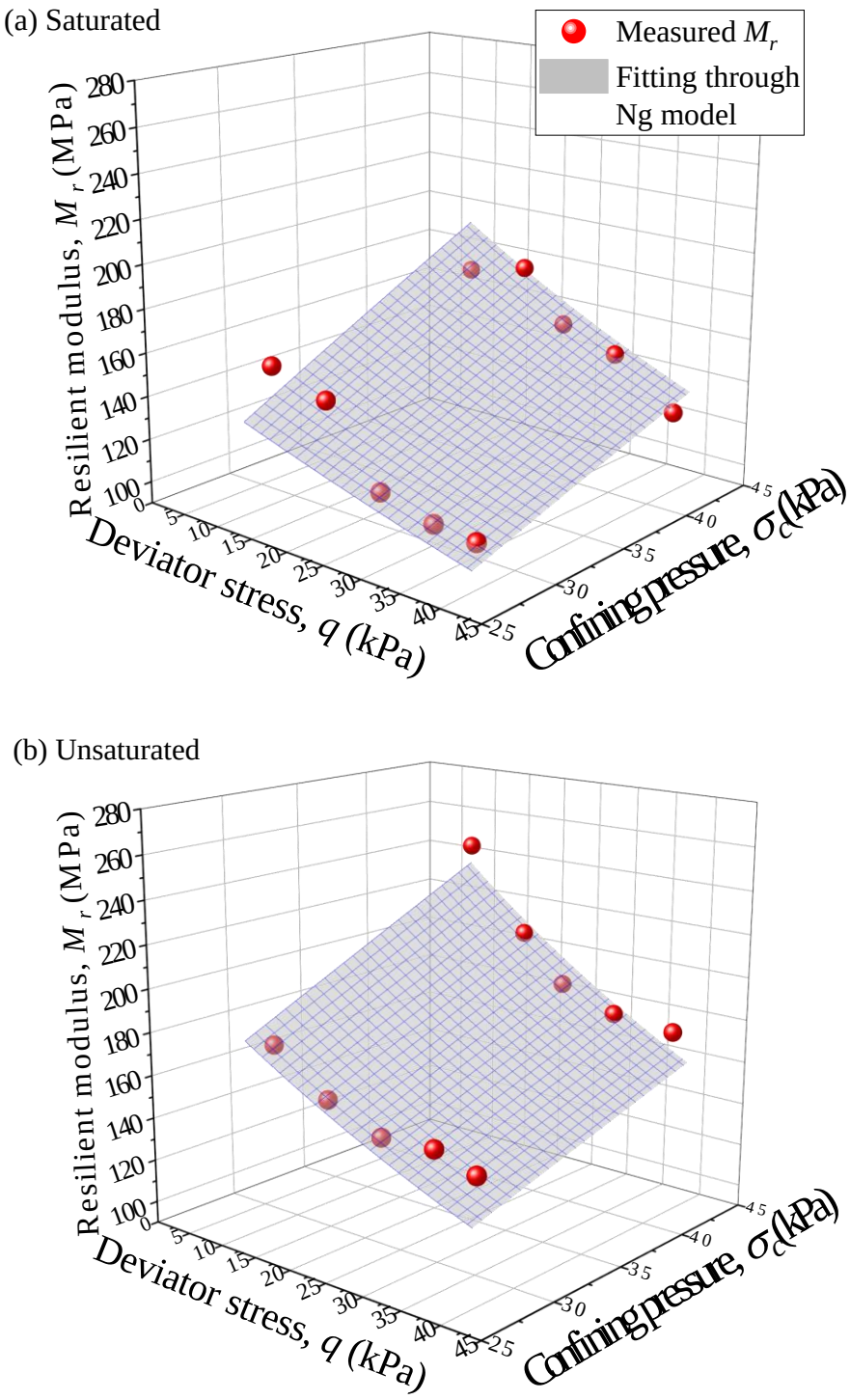

Figure 4-5 Resilient modulus of FT test under saturated and unsaturated condition

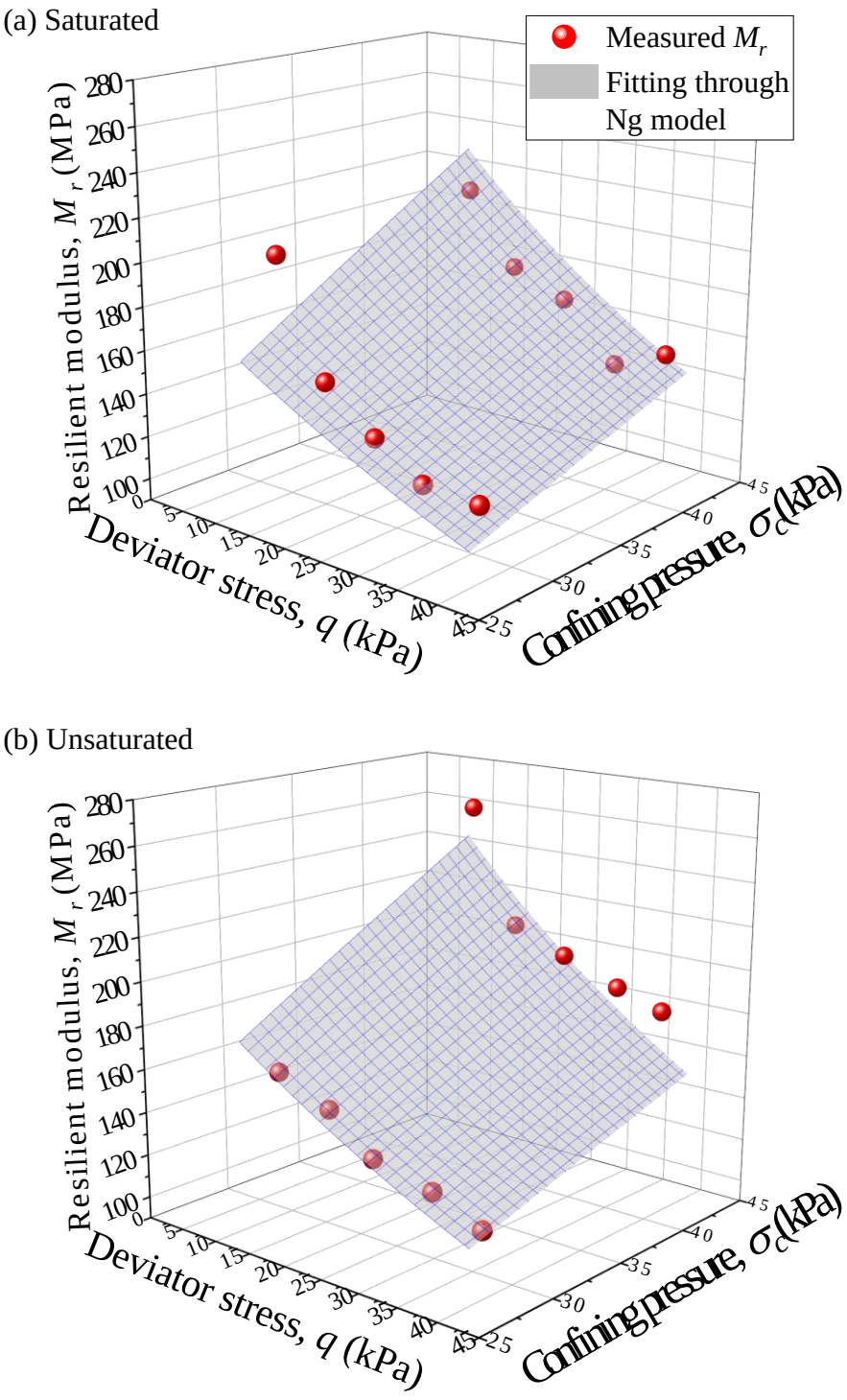

Figure 4-6 Resilient modulus of FTW test under saturated and unsaturated condition

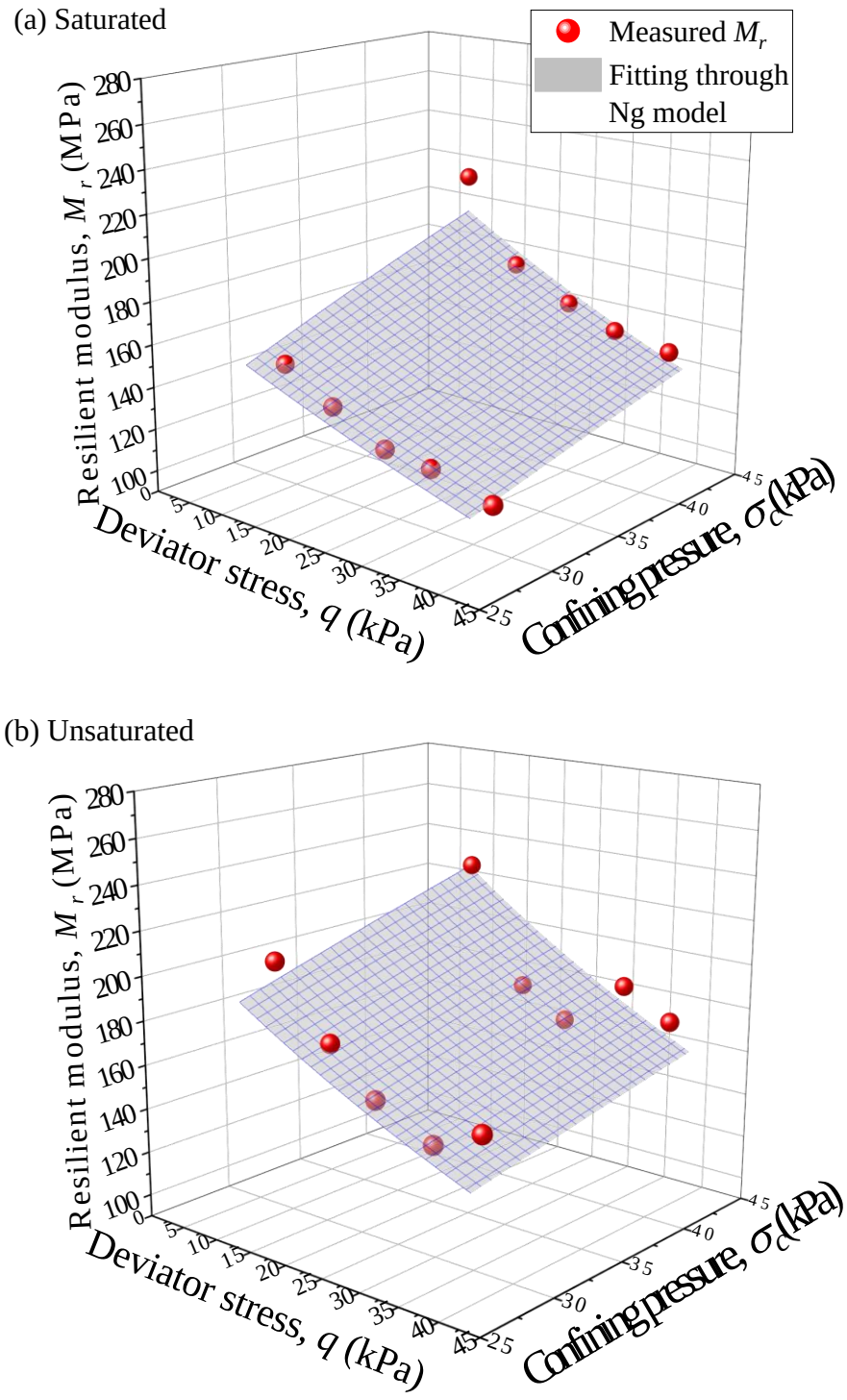

Figure 4-7 Resilient modulus of FWT test under saturated and unsaturated condition

Table 4-1 Regression analysis results through Ng model

Test name	k_1	k_2	k_3	k_4	R^2
U	2.103	1.065	-4.843	2.740	0.949
UW	1.750	1.088	-4.916	3.639	0.905

FT	1.873	0.844	-4.111	2.474	0.910
FTW	2.328	0.823	-4.967	0.845	0.803
FWT	2.011	0.538	-3.382	1.766	0.805

4.1.3 Effects of freeze-thaw action

Freeze-thaw action decreases the M_r when other test conditions are the same as revealed by the comparison between U and FT tests or UW and FTW tests no matter under saturated or unsaturated condition. Besides, freeze-thaw also lowers the sensitive of M_r to stress variables like q or σ_c. In other words, when the σ_c increase the same amount in both unfrozen test (U or UW) and freeze-thawed test (FT or FTW), the M_r of the unfrozen specimen would increase more significantly. Besides, when q increases the same amount in both unfrozen test (U or UW) and freeze-thawed test (FT or FTW), the M_r of the unfrozen specimen would decrease more significantly. In the geometry view, all M_r surfaces in the freeze-thawed test are lower and flatter compared with those surfaces in the unfrozen test. These findings indicate that only attribute thaw weakening to suddenly rising water content is not sufficient for modeling the M_r. Even without rising water content, freeze-thaw action could also degrade the stiffness of subgrade material. It is reasonable to suggest that the freeze-thaw process deteriorates the uniformity of particle skeleton structure and finally leads to worse mechanical properties. Thaw weakening is more like a synergistic effect between freeze-thaw and fluctuating water content.

4.1.4 Effects of wheel loads

For unfrozen specimen, the wheel loads reduce M_r, as indicated in Figures 4-3 and 4-4 (U test and UW test), partly due to the disturbance of soil particle skeleton structure uniformity caused by wheel loads. Whereas, the wheel loads after the freeze-thaw process elevate M_r a little, as illustrated in Figures 4-5 and 4-6 (FT test and FTW test). In this case, the role of wheel loads for freeze-thawed soil is some kind of consolidation to help the specimen regain the uniformity of particle skeleton structure. On the other hand, wheel loads applied on a frozen specimen does not affect M_r greatly, as shown through the comparison between results from FT test and FWT test (see Figures 4-5 and 4-7). A reasonable explanation for such phenomenon is that frozen specimen has a much higher stiffness than thawed specimen. Figures 4-8 and 4-9 demonstrate the relationship between the loading number, N_c, and axial strain, ε_a, and Secant Young's modulus, E_s, during wheel loads process in FWT test and FTW test separately. It is noted that the Secant Young's modulus (E_s) in this study is defined as the ratio of cyclic deviator stress to the maximum axial strain, $(\varepsilon_a)_{max}$, during one loading cycle, which consists of

recoverable axial strain, $(\varepsilon_a)_r$, and permanent axial strain, $(\varepsilon_a)_p$. The smallest axial strain during one loading cycle is defined as $(\varepsilon_a)_p$. It is obvious that a frozen specimen has a larger modulus than unfrozen specimen when the degree of saturation is the same. To be specific, the stiffness of frozen saturated or unsaturated specimen is 6 or 3 times that of the thawed specimen. Within all frozen specimen, though saturated one has a much larger stiffness than unsaturated one as more ice is formed in the saturated specimen, axial strains in these two specimens are both at a very low level. Despite frost-susceptibility of the soil, freezing action significantly amplifies the stiffness of the specimen since ice has a much larger stiffness as compared with soils. Consequently, the axial strain of frozen specimen, no matter maximum axial strain, $(\varepsilon_a)_{max}$, or permanent axial strain, $(\varepsilon_a)_p$, will be a very small value compared with those of thawed specimen. An extremely low ε_a for saturated frozen specimen causes the variation in measured stiffness as the axial displacement transducer fluctuates when measuring such low value. Besides, through comparing Figure 4-9 (a) and (b), unsaturated specimen shows a larger E_s and smaller ε_a than those of saturated specimen, which implies that matric suction strengthens the mechanical properties of a thawed specimen.

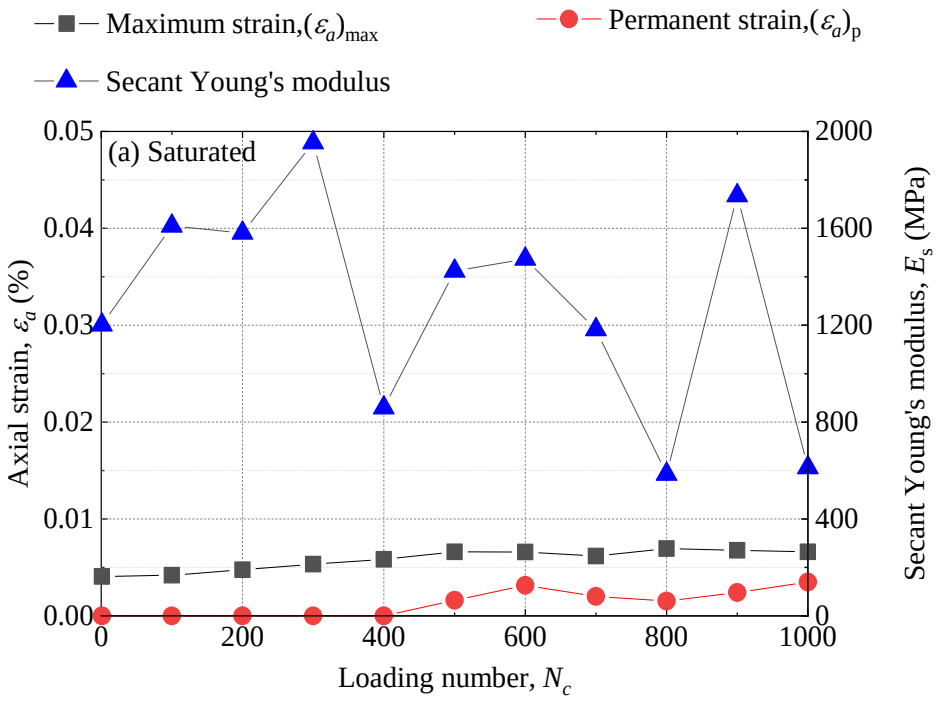

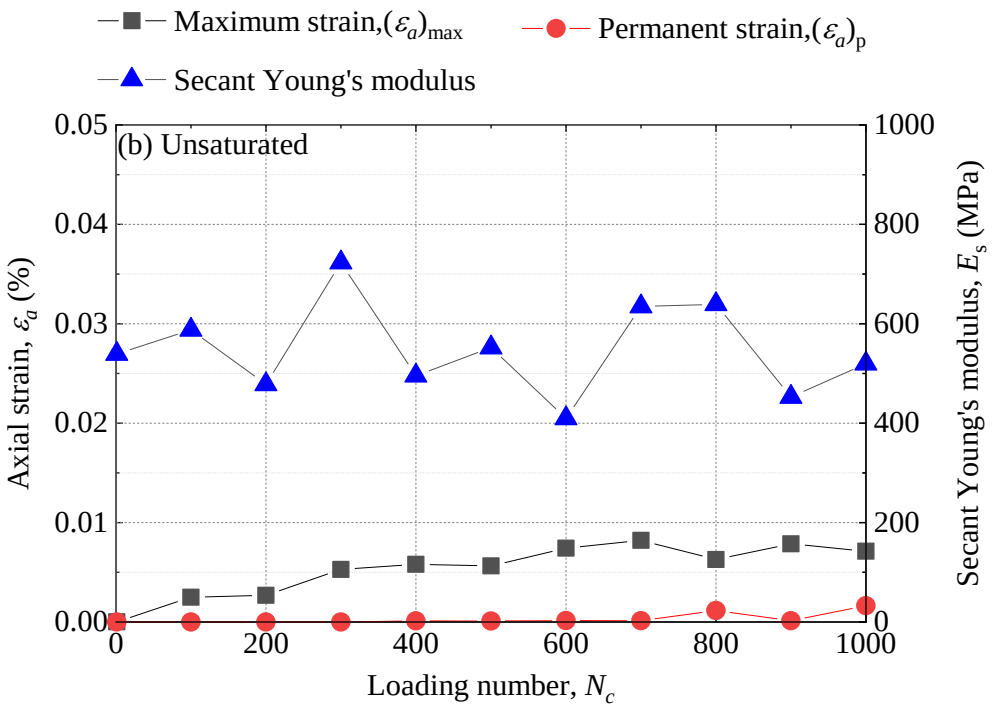

Figure 4-8 Axial strain and Secant Young's modulus during wheel loads process in FWT test

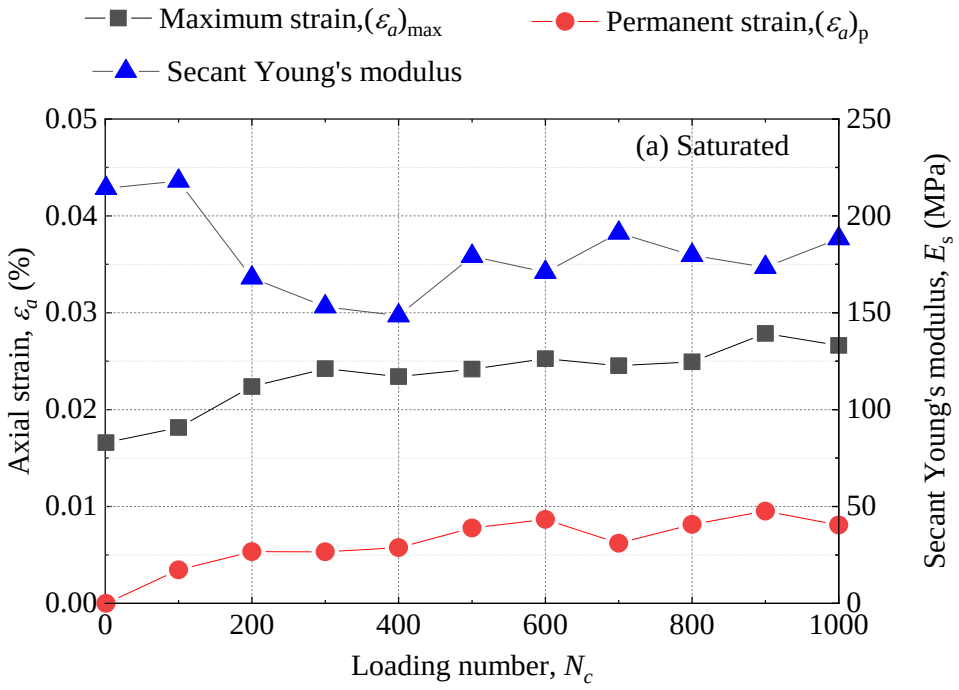

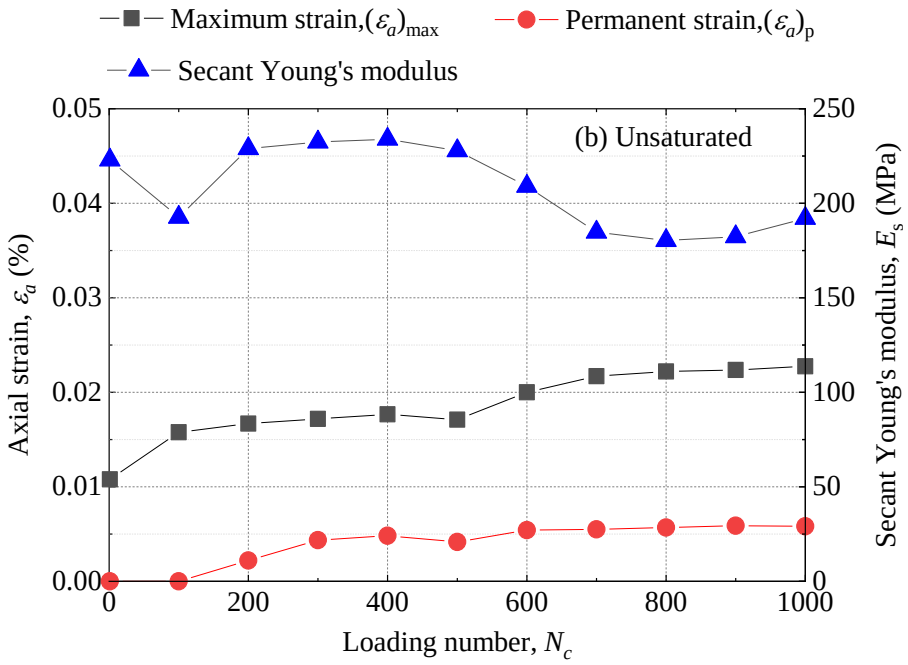

Figure 4-9 Axial strain and Secant Young's modulus during wheel loads process in FTW test

4.2 A MODIFIED CLIMATE MODEL

4.2.1 Applicability of EICM

As above mentioned, both freeze-thaw and rising water content have a negative influence on the resilient modulus. In general, these two factors both contribute to the thaw weakening illustrated by comparing M_r of unsaturated unfrozen (Figure 4-3 (b)) and saturated freeze-thawed test (Figure 4-5 (a)). This synergistic effects of water content and freeze-thaw on M_r has a more complicated mechanism. By comparing Figures 4-3 and 4-5, decreasing amount of M_r is more significant in a saturated condition, which implies that a decrease in M_r caused by freeze-thaw is strongly related to the water content before freezing. More water contents exist in a specimen when the freeze-thaw action is applied, the M_r decreases more significantly after a freeze-thaw action. It is reasonable to assume that the amount of ice formed during the freezing period has a positive relationship with the change of particle skeleton structure and the decreasing amount of M_r.

Ng model (Equation (1-7)) uses the regression constants k_2, k_3, and k_4 to reflect the influence of bulk stress, θ, octahedral shear stress, τ_{oct}, and matric suction, ψ, on M_r separately. Since M_r increases with larger θ and ψ, k_2 and k_4 are positive values. Besides, as M_r decreases with larger τ_{oct}, k_3 is a negative value. As a result, a larger absolute value of k_2,

k_3, and k_4 means a higher effect of θ, τ_{oct}, and ψ on M_r. As shown in Table 4-1, k_2, k_3, and k_4 of the FT test have smaller absolute values comparing with them in the U test, which is consistent with observations that freeze-thaw weakens the influence of θ, τ_{oct}, and ψ.

Regression analysis for FT and FTW tests through EICM (Equation (1-8)) is performed to check its applicability and validity. To extend this model into unsaturated condition, F_{env} in EICM model is added on the Ng model in a similar way as shown in Equation (4-4). As mentioned before, EICM estimates the reduction of M_r caused by freeze-thaw action with an adjustment factor, F_{env}. To examine whether this parameter could fully capture the climate effect, regression analysis is conducted with one variable, F_{env}, and four fixed parameters, k_1, k_2, k_3, and k_4. k_1 to k_4 are determined by regression analysis results of U and UW tests obtained by Ng model.

$$M_r = F_{env} \cdot k_1 p_a \left(\frac{\theta}{p_a}\right)^{k_2} \left(\frac{\tau_{oct}}{p_a} + 1\right)^{k_3} \left(\frac{\psi}{\sigma_{net}} + 1\right)^{k_4} \quad (4\text{-}4)$$

Table 4-2 lists the regression analysis results of FT and FTW tests through EICM model (Equation (4-4)). A decreasing R^2 value compared with R^2 shown in Table 4-1 implies the conventional model cannot fully capture the climate effect. Structure in Equation (4-4) indicates that k_2, k_3, and k_4 are not influenced by F_{env}, as EICM assumes the climate effect only raise or lower the M_r surface but not change the surface shape. However, as shown in Figures 4-3 to 4-7, it is so obvious that this assumption is not consistent with test results in this study, that is climate effect not only raise or lower the M_r surface but also change the surface shape.

Table 4-2 Applicability of EICM and modified Ng models

Test name	k_1	k_2	k_3	k_4	F_{env}	F_{clim}	R^2
U test	2.103	1.065	-4.843	2.740	—	—	0.949
FT test (EICM)	2.103	1.065	-4.843	2.740	0.897	—	0.872
FT test (Modified)	2.103	1.065	-4.843	2.740	—	0.885	0.901
UW test	1.750	1.088	-4.916	3.640	—	—	0.905
FTW test (EICM)	1.750	1.088	-4.916	3.640	0.680	—	0.506
FTW test (Modified)	1.750	1.088	-4.916	3.640	—	0.668	0.619

4.2.2 Modified Ng model

To overcome this drawback, this study assumes the climate effect could be expressed by an adjusting factor that decreases k_1, k_2, k_3, and k_4 with the same ratio. This assumption is

quite reasonable as k_1, k_2, k_3, and k_4 all have a smaller absolute value by the similar degree when the specimen is subjected to freeze-thaw action, indicated by regression analysis results of U test and FT test in Table 4-1. Based on this assumption, Ng model is modified by adding a new parameter, F_{clim}, into all regression parameters (k_1, k_2, k_3, and k_4), as shown in Equation (4-5). Same as before, it is noted that only F_{clim} is variable and k_1 to k_4 are fixed as the value obtained through regression analysis results of U or UW test.

$$M_r = F_{clim} \cdot k_1 p_a \left(\frac{\theta}{p_a}\right)^{F_{clim} \cdot k_2} \left(\frac{\tau_{oct}}{p_a} + 1\right)^{F_{clim} \cdot k_3} \left(\frac{\psi}{\sigma_{net}} + 1\right)^{F_{clim} \cdot k_4} \quad (4\text{-}5)$$

Regression analysis results of FT and FTW tests shown in Table 4-2 proved that modified Ng model has a better performance and accuracy compared with EICM. Figure 4-10 illustrates the fitting surface for FT test results through EICM and modified Ng model. It is obvious that fitting surface through modified Ng model better matches test results compared with fitting surface through EICM. Consequently, the assumption is validated that freeze-thaw action lowers the influence of stress variables like bulk stress, octahedral shear stress, and matric suction and decreases k_1, k_2, k_3, and k_4 with the same ratio. It is noted that R^2 value of tests with wheel loads process, UW and FTW tests, are all lower than R^2 of tests without wheel loads process, U and FT tests. As discussed before, wheel loads process presents a complicated effect on the mechanical properties of specimen when it is applied on a frozen, thawed, or unfrozen specimen. Such a complicated effect decreases the accuracy of all models. A further and comprehensive study on wheel loads, especially how does it affect pavement fatigue life, is necessary.

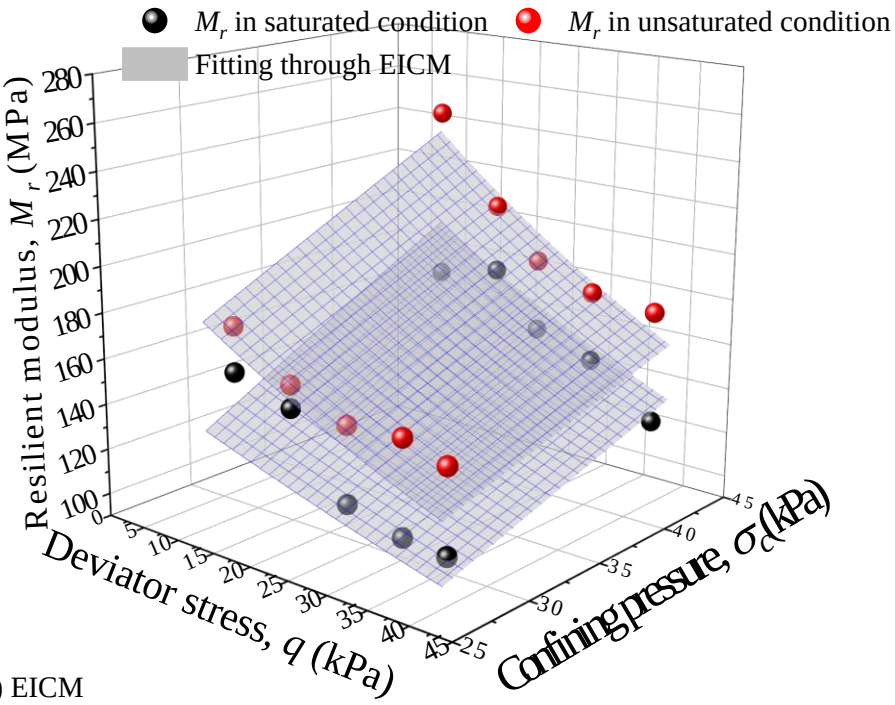

(a) EICM

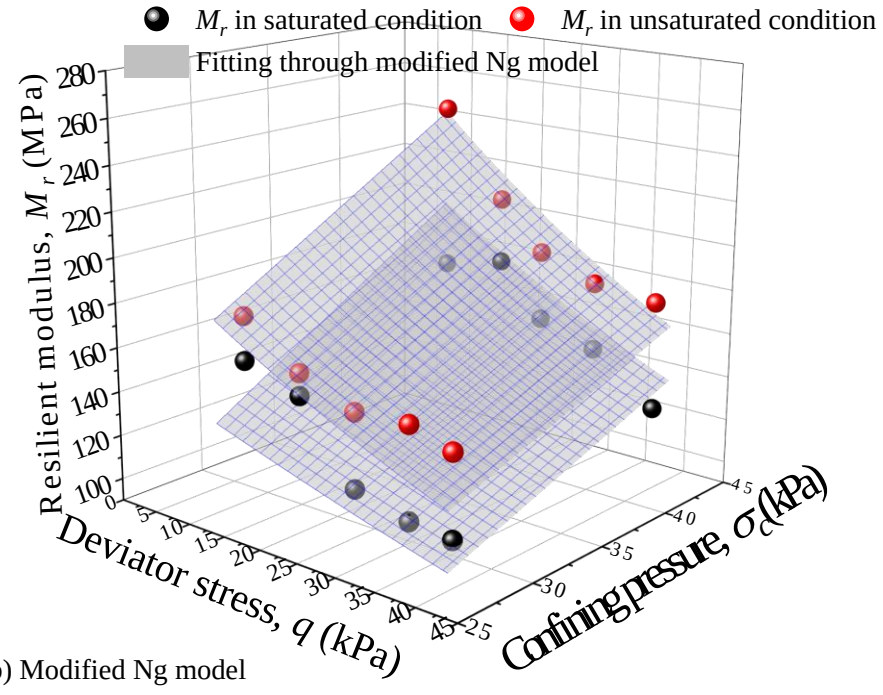

(b) Modified Ng model

Figure 4-10 Fitting surfaces of FT test results through (a) EICM (b) modified Ng model

4.3 APPLICATION TO JAPANESE PAVEMENT DESIGN GUIDE

4.3.1 Fatigue life analysis of asphalt pavement

To evaluate the climate effect on the degradation of subgrade layer, this chapter discusses the fatigue life of the asphalt pavement in cold regions. Japanese design guide provides fatigue failure criteria to calculate allowable number of equivalent 49-kN wheel loads against rutting (N_{fs}) and fatigue cracking (N_{fa}), which are calculated by a theoretical design method [Asphalt Institute, 1982] using a simplified three-layers model which consists of As layer, base layer, and subgrade layer as shown in Figure 4-11. In general, the Japanese pavement design guide assumes the elastic moduli of base layer (E_2) and subgrade layers (E_3) are constant throughout a whole year. However, Ishikawa et al. (2019a) discussed the influences of the seasonality in E_2 on the fatigue life of the asphalt pavement in cold regions by considering freeze thaw action and seasonal fluctuation in water content through combining in-situ measured stiffness and laboratory tested stiffness data. In this chapter, to capture the seasonality of the E_3 and its effect on pavement fatigue life, E_2 is kept as a constant and E_3 varies considering freeze-thaw action and the associated seasonal fluctuation in water content. Moreover, since E_3 does not have a significant effect on the N_{fa} calculation model employed in the Japanese pavement design guide (see Equation (1-2)), only N_{fs} is calculated in this study using Equation (1-1) (Japan Road Association, 2006).

It is noted that the three-layers model shown in Figure 4-11 is simplified by combining asphalt / stabilization into As layer and base / subbase into base layer. Such simplification is recommended since this study focuses on the effect of the seasonality of the E_3 on pavement fatigue life, N_{fs}. Clear distinguishing between asphalt and stabilization or base and subbase does not greatly affect the calculated N_{fs} with changing E_3. Besides, three-layers model helps achieve consistency when performing case study since only asphalt, base, and subgrade layer are essential in actual flexible pavement structure while stabilization and subbase layer are not always set (Figure 4-12).

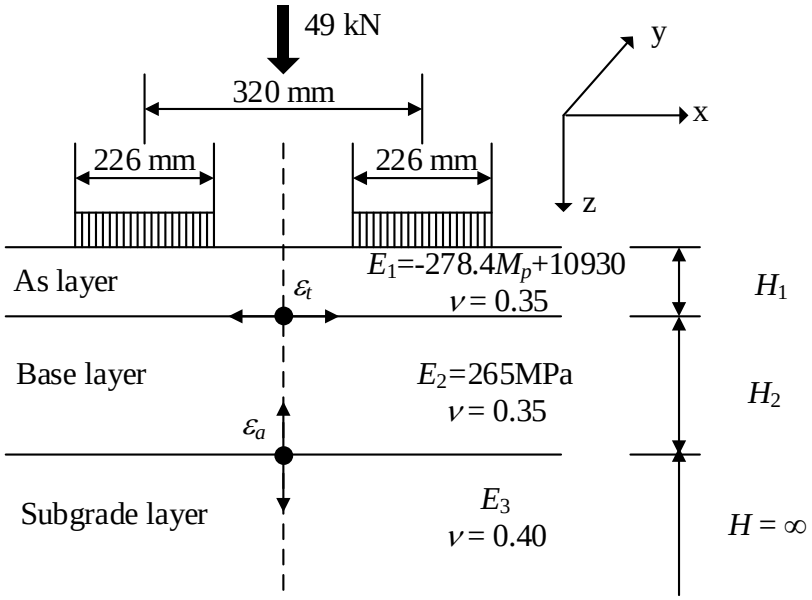

M_p: Monthly mean temperature of As layer.

Figure 4-11 Cross section used in GAMES

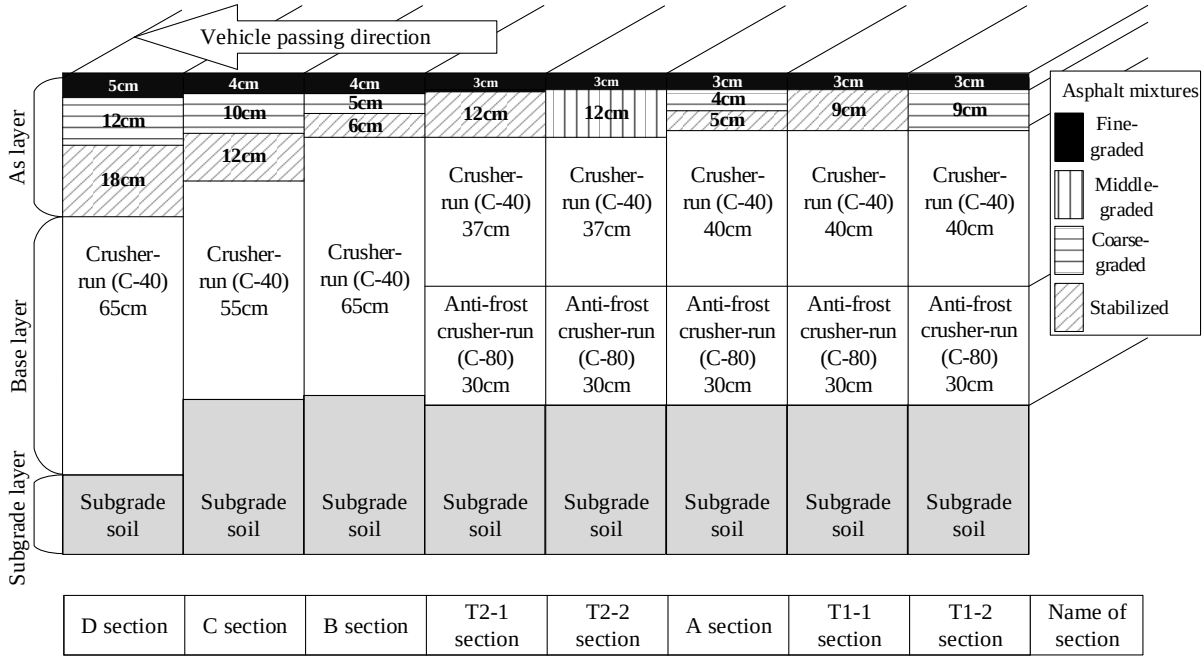

Figure 4-12 Test pavement structures

This study performed fatigue-life analysis against eight test pavement structures located at Hokkaido, Japan. Civil Engineering Research Institute for Cold Region (CERI) designed and constructed eight test pavements [Maruyama et al., 2006]. Figure 4.12 illustrates the structures and length of each test pavement. All eight pavement structures consist of asphalt mixture, base

layer, and subgrade layer with multiple materials and thickness. Four types of asphalt mixtures are used in test pavement. Fine-graded asphalt mixture has a 0 - 13 mm gradation distribution. Middle-graded asphalt mixture has the same range of gradation distribution but more coarse aggregate. Coarse-graded and stabilized asphalt mixture have a 0 - 20 mm and 0 - 30 mm gradation distribution separately. Two types of base layer material are used as C-40, crusher-run with maximum 40 mm gradation distribution, and C-80, anti-frost crusher-run with maximum 80 mm gradation distribution. The asphalt mixtures, crusher-run materials, and subgrade soil in one section are simplified into the As layer, base layer, and subgrade layer separately in GAMES analysis (Figure 4-11). Consequently, all eight sections could be simplified into three layers models with different layer thickness to estimate ε_a through GAMES analysis. Then, monthly fatigue life against rutting, $N_{fs,i}$, is calculated with monthly representative layer moduli. The total fatigue life against rutting, $N_{fs,d}$, is calculated through Equation (4-6).

$$N_{fs,d} = 12/\sum_{i=1}^{12} \frac{1}{N_{fs,i}} \quad (4\text{-}6)$$

Stiffness of asphalt mixture (E_1) is determined through the following equations [Japan Road Association, 2006; Maruyama et al., 2008].

$$E_1 = -278.4M_p + 10930 \quad (4\text{-}7)$$

$$M_p = M_a \left[1 + \frac{2.54}{h_1+10.16}\right] - \frac{25.4}{9(h_1+10.16)} + \frac{10}{3} \quad (4\text{-}8)$$

where M_p is the monthly mean temperature of asphalt mixture at depth of h_1 (℃); M_a is monthly mean air temperature (℃); h_1 is the depth equals to one-third of the height of asphalt mixture (cm).

Constant stiffness of base layer (E_2) through the year is set as 265MPa referring to previous research [Maruyama et al., 2008].

When considering the climate effect, freeze-thaw action and seasonal fluctuation in water content, on the stiffness of subgrade layer, the monthly representative elastic moduli were divided into three types of seasonal E_3 values (E_3 for freezing season, thawing season, and regular season except for freezing and thawing seasons) for the simplicity of the fatigue life analysis. The E_3 value for freezing season is set as 200 MPa, according to back analysis of Falling Weight Deflectometer (FWD) test results [Ishikawa et al., 2019a]. Though Young's modulus of freezing unsaturated specimen is detected around 600 MPa as shown in Figure 4-8, this test result was obtained under fully frozen status, which may be different from in-situ

condition that only top of subgrade layer is frozen during winter season. Consequently, a 200 MPa modulus from in-situ FWD test is treated as a more suitable value for the E_3 to represent whole subgrade layer during freezing season. In addition, this study assumes that when the average frost-penetration depth for the month gets into the subgrade layer regardless of deep or shallow, the E_3 increases due to freezing. Here, the average frost-penetration depth (z) was calculated by substituting the freezing index calculated from the daily mean air temperatures measured by AMeDAS (Automated Meteorological Data Acquisition System) into the modified Berggren formula [Aldrich Jr, 1956] shown below:

$$z = \alpha \sqrt{\frac{172800F}{(L/\lambda)_{eff}}} \quad (4\text{-}9)$$

where α is a correction coefficient; F is a freezing index which is the average air temperature during freezing season multiplied by its duration in days; $(L/\lambda)_{eff}$ is an effective ratio of L to λ; L is the latent heat of soil; λ is a thermal conductivity of the soil.

The E_3 value for the regular season is estimated by substituting the value of k_1, k_2, k_3, and k_4 into Ng model as shown in Equation (4-10). The principal stress ratio is equal to 4 under 5 kPa confining pressure to determine bulk stress and octahedral shear stress. It is noted that this stress condition was selected so that M_r at normal season matches layer stiffness determined in previous research [Maruyama et al., 2008].

$$M_r = 2.103 \cdot p_a \left(\frac{\theta}{p_a}\right)^{1.065} \left(\frac{\tau_{oct}}{p_a} + 1\right)^{-4.843} \left(\frac{\psi}{\sigma_{net}} + 1\right)^{2.74} \quad (4\text{-}10)$$

The matric suction in subgrade layer is also necessary to estimate E_3. Ishikawa et al. [2012] performed long-term field measurement of frost-penetration depth, daily precipitation, and degree of saturation in each layer of the pavement. Figure 4-13 illustrates the long-term field measured degree of saturation, S_r, of subgrade layer through a year. The subgrade material is a sandy soil, named as Tomakomai soil, composed of 8% clay, 13% silt, 51% sand, 28% gravel. This study uses Toyoura sand to represent the subgrade layer since the mechanical and hydraulic properties of Tomakomai soil is under investigation. It is assumed that effective degree of saturation, S_e, would be same in Toyoura sand subgrade and Tomakomai soil subgrade under same climate condition. S_e of subgrade layer illustrated in Figure 18 was calculated by using a residual degree of saturation (S_{rr}) of 25.67%, which was determined through the SWCC estimated with grain-size distribution of Tomakomai soil [Fredlund et al., 2002]. Consequently, monthly average S_e is selected to determine matric suction of subgrade layer in each month through SWCC of Toyoura sand, and monthly representative M_r is calculated by Equation (4-10).

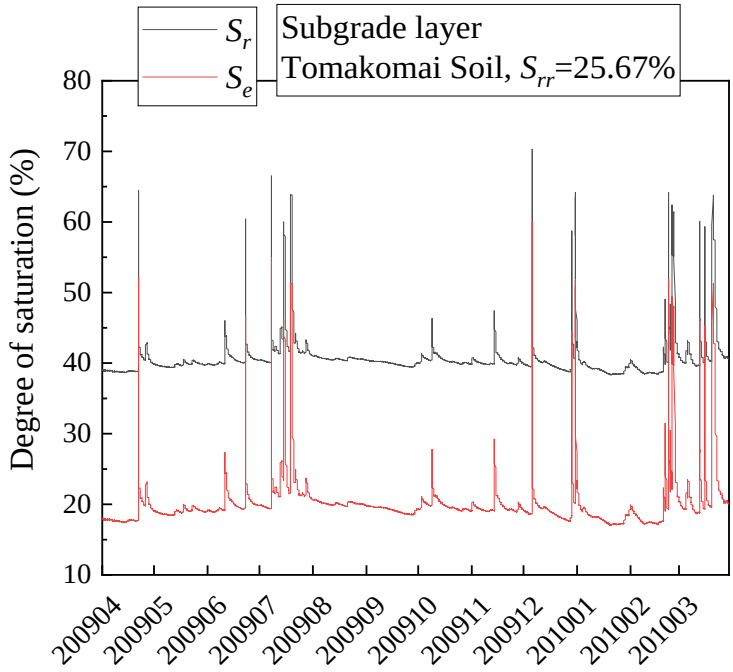

Figure 4-13 Long-term field measured degree of saturation of subgrade layer

The E_3 value for thawing season is estimated by modified Ng model with considering climate effect, F_{clim}. By substituting F_{clim} and the value of k_1, k_2, k_3, and k_4 into Equation (4-5), the M_r of the thawed season could be estimated as shown in Equations (4-11) and (4-12). It is noted that matric suction used here corresponds to the highest water content during thawing season. In other words, E_3 value for thawing season stands for the worst situation and the recovering period from thawing season to regular season is not considered in this chapter. A furthermore comprehensive model will be shown in Chapter 6.

$$M_r = F_{clim} \cdot 2.103 \cdot p_a \left(\frac{\theta}{p_a}\right)^{F_{clim} \cdot 1.065} \left(\frac{\tau_{oct}}{p_a} + 1\right)^{F_{clim} \cdot -4.843} \left(\frac{\psi}{\sigma_{net}} + 1\right)^{F_{clim} \cdot 2.74} \quad (4\text{-}11)$$

$$F_{clim} = 0.885 \quad (4\text{-}12)$$

Table 4-3 Monthly representative elastic moduli of subgrade layer

Month		1	2	3	4	5	6	7	8	9	10	11	12
Original design guide		76	76	76	76	76	76	76	76	76	76	76	76
Water content fluctuation	10 Hz	77	75	61	76	76	71	69	76	76	76	76	75
	0.2 Hz	71	69	55	70	70	65	63	70	70	70	70	69
Climate effect	10 Hz	77	200	50	76	76	71	69	76	76	76	76	75

0.2 Hz	71	200	45	70	70	65	63	70	70	70	70	69

Consequently, Table 4-3 lists the estimated monthly representative E_3 through a year with consideration of climate effect under different loading frequency. E_3 (f=0.2 Hz) are estimated with original MR test data, while E_3 (f=10 Hz) are estimated with converted MR test data through Equations (4-2) and (4-3). As the climate effect is a synergistic effect between water content fluctuation and freeze-thaw action, it is essential to check climate effect step by step. For this reason, monthly representative E_3 only considering water content fluctuation under different loading frequency are also calculated through Equation (4-10) and shown in Table 4-3. Besides, referring to previous research [Maruyama et al., 2008], a constant E_3 through the year is set as 76MPa and applied in the original design guide condition. Poisson's ratio of As layer, base layer, and subgrade layer are set as 0.35, 0.35, and 0.4 separately, which come from design guide recommend value.

From Table 4-3, it is recognized that compared with the original design guide condition, E_3 drops at early spring (Mar) and summertime (Jun and Jul) when the water content fluctuation is considered since snowmelt water and the thawing of ice lenses at thawing season and heavy rainfall at summertime increases the water content in subgrade layer and finally decreases the stiffness. When freeze-thaw action is also considered, E_3 drops furthermore at Mar due to the thaw weakening and increases to 200 MPa at Feb due to the freezing action. Besides, moduli decrease with loading frequency.

4.3.2 Loading frequency effect on fatigue life of the pavement

To discuss the influence of loading frequency on fatigue life against rutting, E_3 (f=0.2 Hz) and E_3 (f=10 Hz) listed in Table 4-3are used to calculate N_{fs} in all eight test pavement structures. Figure 4-14 displays the N_{fs} with variant E_3 considering water content fluctuation (named as "N_{fs}-Water content fluctuation") and climate effect (named as "N_{fs}-Climate effect") under different loading frequency. It is obvious that N_{fs} (f=10Hz) are always larger than N_{fs} (f=0.2Hz) no matter only consider water content fluctuation or synergistic climate effect on E_3. To clearly discuss the loading frequency effect on the fatigue life, the ratio of N_{fs} (R_{Nf}) for different pavement structures are also plotted in the Figure 4-14. The R_{Nf} considering loading frequency with water content fluctuation or climate effect is determined through dividing the N_{fs} (f=0.2Hz) by the N_{fs} (f=10Hz) when considering water content fluctuation or synergistic climate effect on E_3. R_{Nf} in all pavement structures are around 0.861, implies that fatigue life decreases about

13.9% when loading frequency lowers from 10Hz to 0.2Hz. Conclusively, converting E_3 (f=0.2Hz) to E_3 (f=10Hz) is necessary as loading frequency effect could not be ignored.

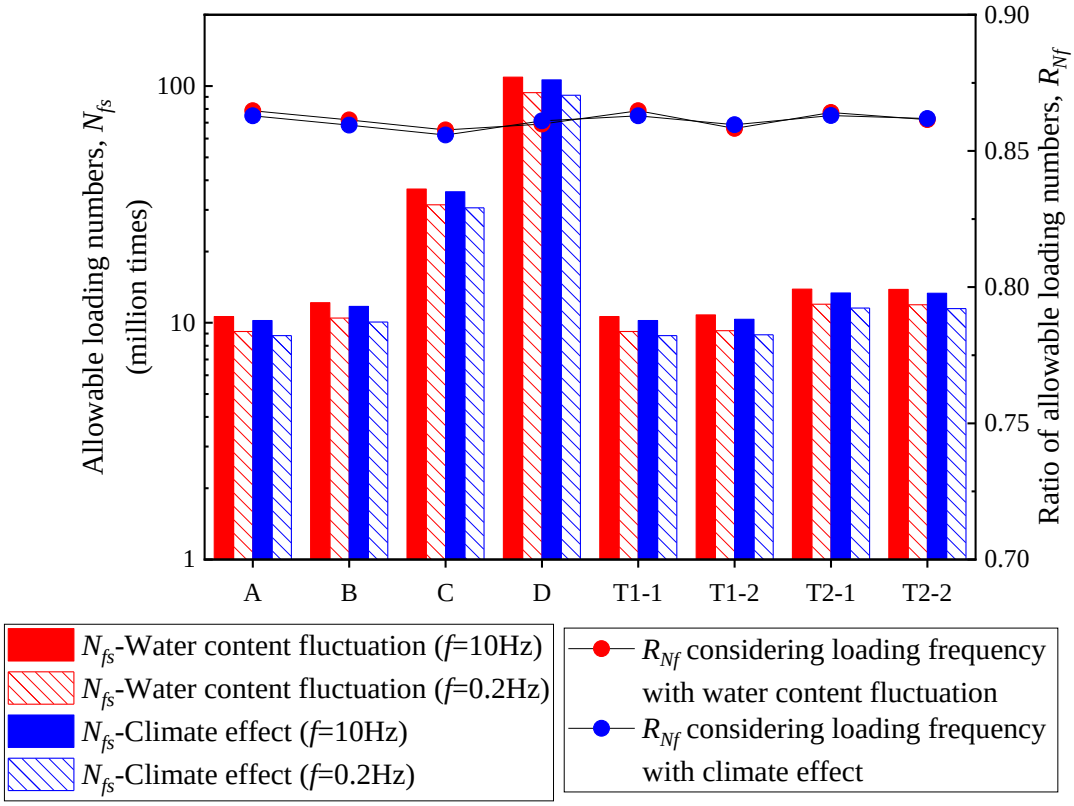

Figure 4-14 Loading frequency effect on fatigue life against rutting

4.3.3 Climate effect on fatigue life of the pavement

To discuss the climate effect, Figure 4-15 displays the N_{fs}-Water content fluctuation and N_{fs}-Climate effect under 10Hz loading frequency. N_{fs} with constant E_3 of 76 MPa (named as "N_{fs}-Original") is also shown here. It is obvious that N_{fs}-Water content fluctuation is smaller than N_{fs}-Original but larger than N_{fs}-Climate effect, implies that reduced E_3 caused by sudden increasing water content decreases N_{fs} and freeze-thaw action decreases N_{fs} further as the reduced E_3 during thawing season has a stronger influence on the N_{fs} than the increasing E_3 during the freezing season. To clearly discuss the influence of water content fluctuation, freeze-thaw action, and climate effect on the fatigue life, R_{Nf} for different structures are also plotted in the Figure 4-15. The R_{Nf} considering water content fluctuation or climate effect are determined through dividing the N_{fs}-Water content fluctuation or N_{fs}-Climate effect by the N_{fs}-Original, while the R_{Nf} considering freeze-thaw action is determined through dividing the N_{fs}-Climate

effect by the N_{fs}-Water content fluctuation. All ratios are lower than 1, indicates that influence of water content fluctuation, freeze-thaw action, and climate effect on E_3 all decrease the fatigue life. R_{Nf} caused by water content, freeze-thaw action, and climate effect are around 0.938, 0.965, and 0.905 separately. In other words, the N_{fs} decreases 6.2% when changing E_3 caused by water content fluctuation is considered and it would further decrease 3.5% when effect of freeze-thaw action on E_3 is also considered. A synergistic climate effect on E_3 decreases N_{fs} about 9.5%.

These results suggest that for improving the applicability and validity of the current Japanese design standard, the introduction of the theoretical design method for pavement structures, which can take account of the effects of the freeze-thaw actions and the concurrent seasonal fluctuation in water content on the subgrade layer stiffness, is effective in the asphalt pavements for cold regions.

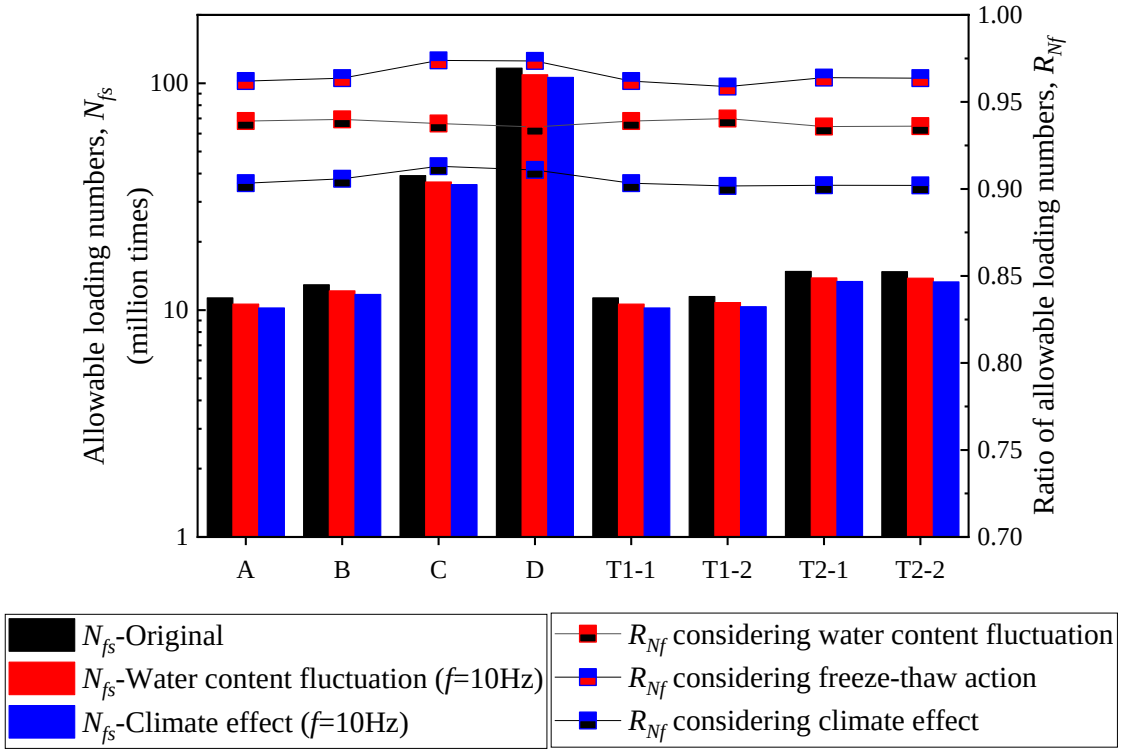

Figure 4-15 Climate effect on fatigue life against rutting

4.4 SUMMARY

The following findings can be mainly obtained in this chapter:

1. Through performing a series of suction-controlled resilient modulus tests for a subgrade material with variant freeze-thaw, wheel loads, and water contents conditions, the effects of freeze-thaw actions and the concurrent seasonal fluctuations in water content (named as climate effect in this study) are examined and evaluated. As a consequence, climate effect degrades the resilient deformation characteristics of subgrade materials.

2. Climate effect not only reduces the resilient modulus, but also weakens the influences of stress variables like bulk stress, octahedral shear stress, and matric suction on resilient modulus. Besides, the decreasing amount of resilient modulus caused by climate effect is more significant in a saturated condition, which implies that a synergistic effect of water content and freeze-thaw on the resilient modulus. The degradation in resilient modulus caused by freeze-thaw relates to the water content before the specimen is frozen. It is reasonable to assume that the amount of ice formed during the frozen period has a positive relationship with the change of particle skeleton structure uniformity and degradation of the mechanical properties of subgrade materials.

3. A new parameter representing the climate effect, F_{clim}, is added into Ng model to quantitatively evaluate resilient modulus for the subgrade material under complex freeze-thaw, fluctuating water content, and variant stress states. A better performance compared with EICM proved the applicability and reliability of newly proposed modified Ng model.

4. To modify current Japanese design guide by replacing constant subgrade layer moduli with a variant relating to water content fluctuation and freeze-thaw history, newly pro-posed modified Ng model, long-term measured in-situ subgrade layer water content, and laboratory obtained SWCC are used. Calculated fatigue life against rutting proves that both water content fluctuation and freeze-thaw action degrade stiffness of subgrade layer and finally decrease the fatigue life of asphalt pavements in cold regions. Accordingly, when developing a design method with high prediction accuracy for the asphalt pavements in cold regions, it is important to consider the change in the stiffness of sub-grade layer caused by the climate conditions.

5 EFFECT OF PRINCIPAL STRESS AXIS ROTATION ON RUTTING

5.1 MATERIALS AND MULTI-RING SHEAR TESTING PROGRAM

Permanent deformation of base layers caused by traffic wheel loads is one of primary pavement failure mechanisms because the main function of the base layer is to provide structural support to the top layer of the pavement. Permanent deformation of unbound aggerate materials is influenced by many factors like particle size distribution, density, water contents, the strength of materials, loading history, the stress level, the number of loading, principal stress axis rotation, etc.

Many predictive models have been proposed based on more or fewer factors listed above. The Mechanistic-Empirical Pavement Design Guide (MEPDG) model (Equation (1-9)) [NCHRP, 2004] relates the permanent strain to the resilient modulus. On the other hands, NCHRP Project 4-23 [Saeed et al., 2001] pointed out that shear strength but not resilient modulus is one of the most significant mechanical properties influencing pavement performance. Then, K-T model (Equation (1-10)) [Korkiala-Tanttu, 2009] and UIUC model (Equation (1-11)) (Chow et al., 2014a) use shear strength to construct a predictive model. As a result, UIUC model shows high accuracy on permanent strain prediction.

However, the applicability of UIUC model on materials with different moisture contents has not been verified. Besides, all these models are based on results from repeated loading triaxial test, which has a constant confining stress, and do not consider the effect of principal stress axis rotation (PSAR), which is always encountered under in-situ conditions and has a great effect on permanent deformation [Miura et al., 1986; Chan et al., 1994; Brown, 1996; Gräbe et al., 2009].

The objective of this chapter is to implement all these limitations mentioned above. To simulate the in-situ stress state in the pavement, Ishikawa et al. [Ishikawa et al., 2007] developed a multi-ring shear apparatus for laboratory element tests, which could apply cyclic axial load and shear stress. This study utilizes multi-ring shear test results obtained by Inam [Inam, 2012] to check which one between resilient modulus and shear strength is more significant factor on permanent deformation. Then, UIUC model was modified by considering

the effect of PSAR on permanent strain. Modified UIUC model was validated at various moisture contents and stress states.

Materials used in this research include natural crusher-run with 40 mm maximum particle size (C-40) and recycled crusher-run which is obtained from demolished concrete structure with 40 mm maximum particle size (C-40). As the width of the specimen is 60 mm and minimum diameter of the mould sizes to fabricate specimens should be equal or greater than five times the maximum particle size [AASHTO, 2003], the maximum particle size selected in this research was 9.5 mm. After screening out particles larger than 9.5 mm, test materials are named as C-9.5 (natural crusher-run) and RC-9.5 (recycled crusher-run) in this study. As fine particles may enter the small gaps of the rings of the multi-ring shear apparatus, materials were washed inside the 0.075 mm sieve to remove the fine particles. Besides, these two materials are parallel grading materials. More property details about these materials, like grain size distribution and SWCC curve, are shown by Inam [Inam et al., 2012].

Ishikawa et al. [Ishikawa et al., 2007] developed a multi-ring shear apparatus for laboratory element tests, which could apply cyclic axial loading and shear stress simultaneously. The width of the specimen is 60 mm and the height is 60 mm. Shear strain and axial strain is calculated through transducers. The schematic diagram of the multi-ring shear apparatus is shown in Figure 5-1.

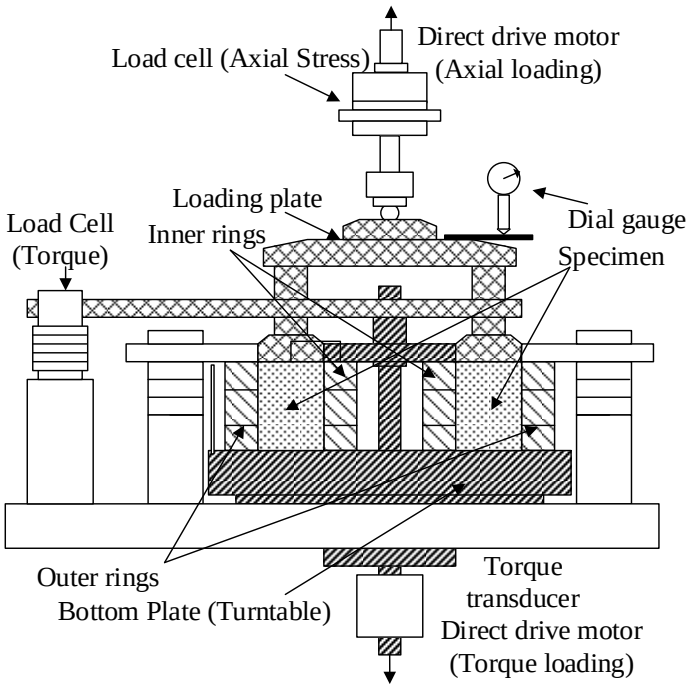

(a) schematic diagram of the multi-ring shear apparatus

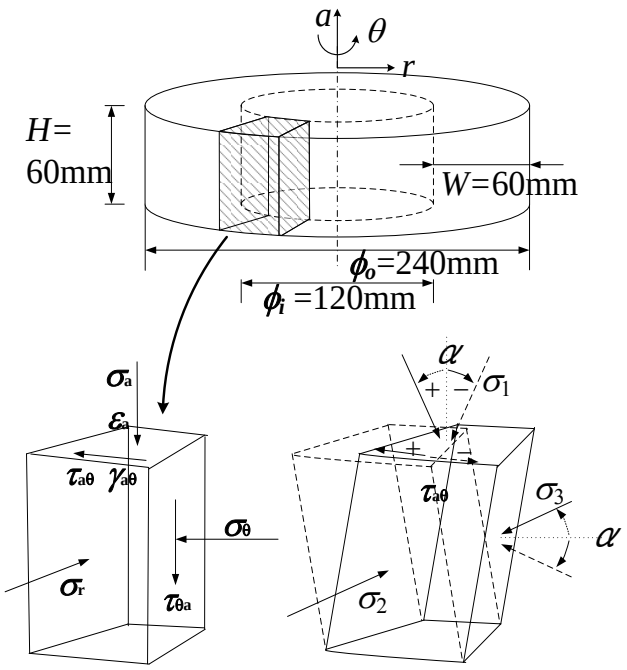

(b) definition of stress and deformation

Figure 5-1 Multi-ring shear apparatus (after Ishikawa et al., 2011)

Inam [2012] performed a series of monotonic and cyclic loading tests. The degree of saturation (S_r) of the specimen was selected as S_r=19%, 33%, and 48% based on the field data obtained from the Tomakomai, Japan. An oven-dried sample was also selected to compare the results with those of the unsaturated specimen. A dry density of 1.581–1.583 g/cm^3 was selected for the multi-ring shear tests. The stress states for the multi-ring shear tests were determined based on a stress analysis of a Japanese paved road model by the General Analysis Multi-layered Elastic Systems (GAMES) [Maina and Matsui, 2004]. The multi-ring shear apparatus simulates the field loading conditions by applying the axial load and the shear load in a sinusoidal waveform. The loading frequency in this study was 0.02 Hz due to the limitation of the apparatus.

Three types of tests were performed as monotonic shearing test, cyclic axial loading test, and cyclic axial and shear loading test. In monotonic shearing tests, keeping axial stress constant, shear stress increased monotonically at the rate of a shear strain of $\gamma_{a\theta}$=0.1%/min until the shear strain reaches 3%. In cyclic axial loading test, only apply axial load in the sinusoidal waveform to the specimen, which is similar to repeated loading triaxial test without rotation of the principal stress axis. In this research, the cyclic axial tests are referred to as fixed-place loading tests (FL tests). In cyclic axial and shear loading test, the axial load and the shear load, both in the sinusoidal waveform, are cyclically applied to the specimen. The shear load is

cyclically applied for bidirectional loading, similar to two-way traffic on pavement, by changing the phase angle of 180° for every succeeding loading cycle. This test is considered as moving-wheel loading tests (ML tests), in which the rotation of the principal stress axis occurs similarly to in-situ traffic loading conditions. The number of loading cycles of FL test and ML test were both 400. Several tests under identical condition were performed and the coefficient of variation (CoV) is 8.89%, which could validate the accuracy of the test method and apparatus. Based on this accuracy, each type of experiment was performed once and the test results are treated as accurate and precise. The experimental conditions for the multi-ring shear tests performed in this research are summarized in Table 5-1.

Table 5-1 Experimental conditions of multi-ring shear tests for aggregate

Test material	S_r (%)	ρ_{dc} (g/cm^3)	Monotonic shearing tests		FL tests		ML tests	
			σ_a (kPa)	$\gamma_{a\theta}$ (%/min)	$(\sigma_a)_{max}$ (kPa)	$(\tau_{a\theta})_{max}$ (kPa)	$(\sigma_a)_{max}$ (kPa)	$(\tau_{a\theta})_{max}$ (kPa)
C-9.5	Oven dried	1.58	114.2	0.1	114.2	0	114.2	30/15
	19	1.58	114.2	0.1	114.2	0	114.2	30/15
	33	1.58	114.2	0.1	114.2	0	114.2	30/15
	48	1.58	114.2	0.1	114.2	0	114.2	30/15
RC-9.5	Oven dried	1.47	114.2	0.1	114.2	0	114.2	30
	19	1.47	114.2	0.1	114.2	0	114.2	30
	33	1.47	114.2	0.1	114.2	0	114.2	30
	48	1.47	114.2	0.1	114.2	0	114.2	30

5.2 DEPENDENCY OF PERMANENT STRAIN ON SHEAR STRENGTH

A higher resilient modulus leads to a smaller average vertical resilient strain (ε_v) and finally lower permanent strain in MEPDG as shown in Equation (1-9). Besides, the water content just affects the curve shape of permanent strain with number of loading cycles but will not affect the ratio between permanent strain and resilient strain as shown in Equation (1-9). However, from the multi-ring shear test results, these dependencies are not always true. Figure

5-2(a) indicates the resilient and permanent strain in the last loading cycle of FL test and ML test. The solid and dash line connect the scatter by the sequence of permanent strain of C-9.5 and RC-9.5 respectively. C-9.5 shows smaller permanent deformation than that of RC-9.5 when the water content and applied stress are same, which illustrates that these two materials have different mechanical properties, though they share similar grain size distribution. In Figure 5-2(a), the tendency that permanent strain increases with increasing resilient strain only exist in RC-9.5 in FL test and all other test results did not show this tendency. Besides, the effect of water content on permanent strain is significant. For example, Oven-dried and 19% degree of saturation RC-9.5 in ML test show similar resilient strain around 0.05, but the permanent strain of them variates a lot. Moreover, the dependency of permanent strain on test material could also be observed. Oven-dried C-9.5 and RC-9.5 in FL test share the same water content and similar resilient strain, but the permanent strain is different. In addition, permanent strain in ML test is 3 to 4 times than it in FL test, which illustrates the great effect of PSAR on permanent strain and this effect should be considered. As a result, it is obvious that the dependency between resilient modulus and permanent strain variates a lot and a prediction of permanent strain based on MEPDG model may not be accurate.

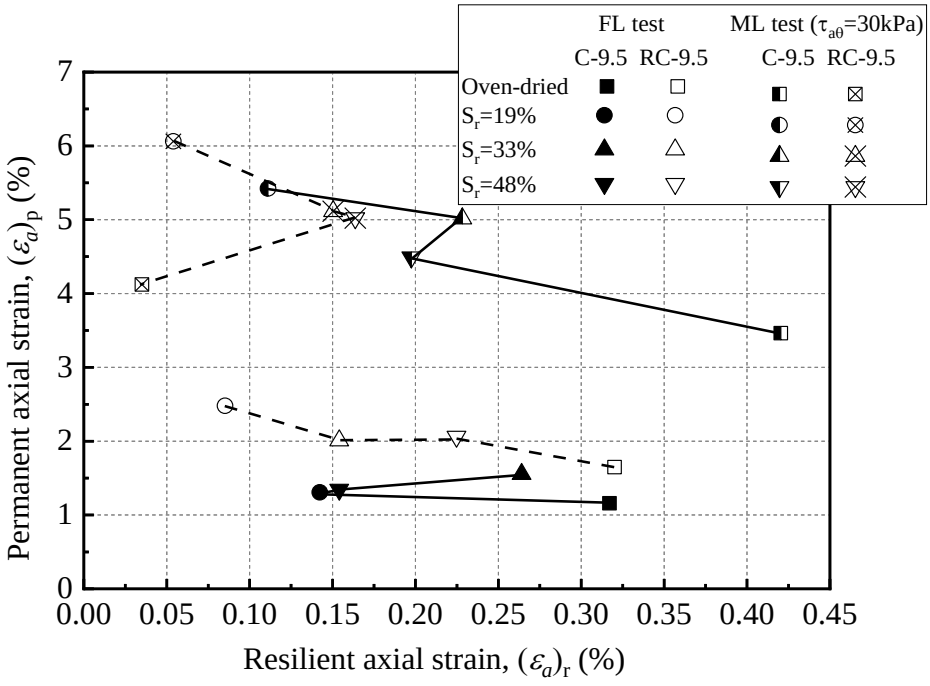

(a) Resilient and permanent axial strain

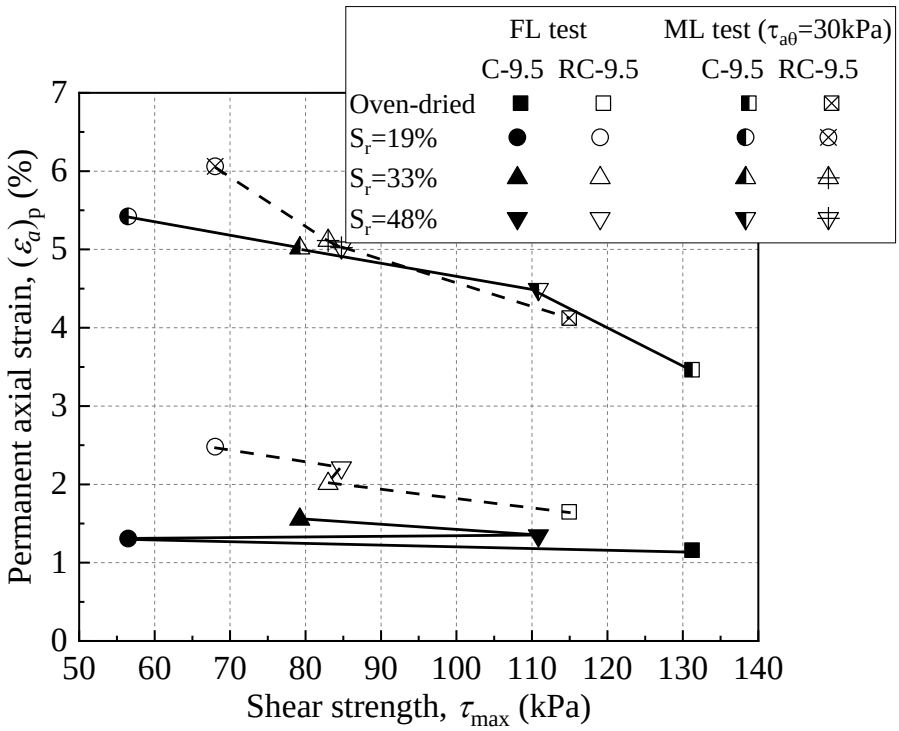

(b) Shear strength and permanent axial strain

Figure 5-2 Relations between permanent, resilient axial strain, shear strength

On the other hands, the shear strength has a strong effect on permanent deformation in UIUC model as shown in Equation (5-13). In this study, Shear strength of the C-9.5 and RC-9.5 is estimated by applying Duncan-Chang model [Duncan and Chang, 1970], shown in Equations (5-1) and (5-2), to test results of the monotonic shearing test.

$$\sigma_1 - \sigma_3 = \frac{\varepsilon}{a+b\varepsilon} \tag{5-1}$$

$$(\sigma_1 - \sigma_3)_{ult} = \frac{1}{b} \tag{5-2}$$

where *a* and *b* are material constants, reciprocal of *a* is the initial tangential Young's modulus and the reciprocal of *b* is the failure value of stress difference

For monotonic shearing test performed by multi-ring shear apparatus, above equations change to following forms. The regression analysis result is shown in Figure 5-3 and Table 5-2.

$$\tau_{a\theta} = \frac{\gamma_{a\theta}}{a+b\gamma_{a\theta}} \tag{5-3}$$

$$\tau_{max} = (\tau_{a\theta})_{ult} = \frac{1}{b} \tag{5-4}$$

Figure 5-2(b) shows the relation between estimated shear strength and permanent axial strain of the last loading cycle. The solid and dash line connect the scatter by the sequence of permanent strain of C-9.5 and RC-9.5 respectively. The tendency is significant that higher shear strength leads to smaller permanent axial strain regardless of the type of materials only except C-9.5 with S_r=19% and RC-9.5 with S_r=33% in FL test, which may due to some experimental error happened during the tests. Compare Figure 5-2(a) and (b), it is reasonable to conclude that the dependency between shear strength and permanent strain is more significant than the dependency between resilient strain and permanent strain, which is the reason to choose UIUC model but not MEPDG model to predict the permanent strain.

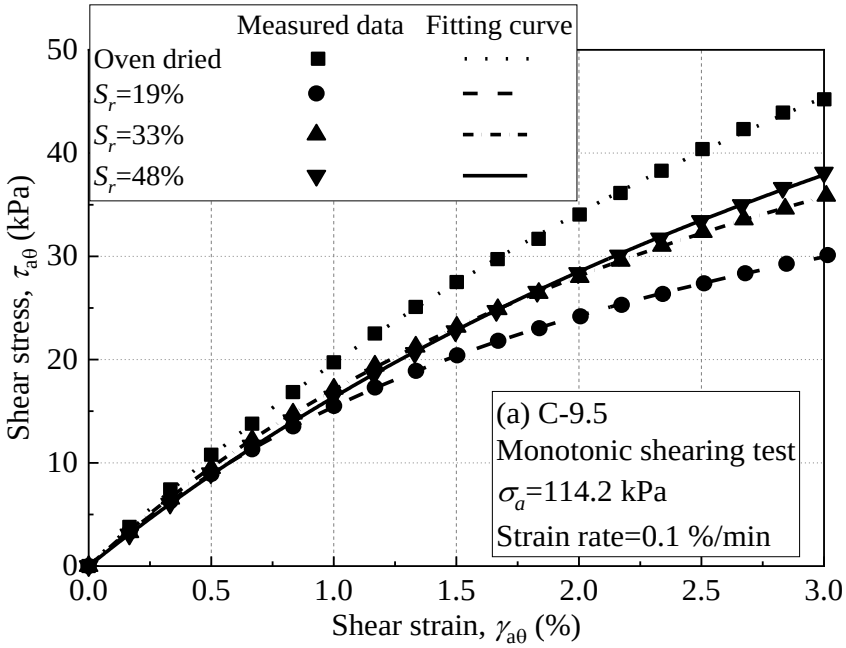

(a) C-9.5

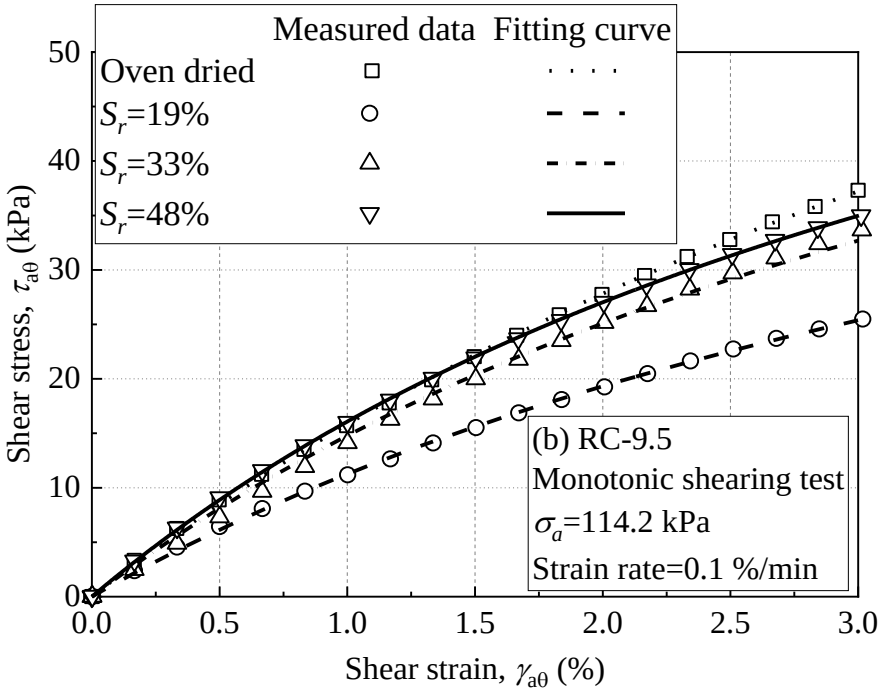

(b) RC-9.5

Figure 5-3 Shear stress-strain curve in monotonic shearing test

Table 5-2 Regression analysis results with Duncan-Chang model

Materials	S_r (%)	a	b	R^2	τ_{max}(kPa)
C-9.5	Oven dried	0.04322	0.00762	0.999	131.23
	19	0.04711	0.01770	0.999	56.50
	33	0.04599	0.01262	0.999	79.24
	48	0.05210	0.00902	0.999	110.86
RC-9.5	Oven dried	0.05449	0.00870	0.999	114.94
	19	0.07411	0.01470	0.999	68.03
	33	0.05562	0.01205	0.998	82.99
	48	0.05040	0.01180	0.999	84.75

5.3 PROPOSAL AND APPLICATION OF MODIFIED UIUC MODEL

To capture the effect of PSAR on permanent deformation, a parameter, $(R_s)_{ave}$, proposed by Ishikawa et al. [2014b] is used. $(R_s)_{ave}$ means the average ratio of axial strain between specimen with and without principal stress axis rotation. Besides, $(R_s)_{ave}$ could be roughly approximated by the following equation.

$$(R_s)_{ave} = exp\ (A\frac{(\tau_{a\theta})_{max}}{(\sigma_a)_{max}}) \tag{5-5}$$

where $(\sigma_a)_{max}$ is maximum of applied axial stress; $(\tau_{a\theta})_{max}$ is maximum of applied shear stress; A is material constant.

As the definition of stress is not the same in triaxial compression tests and multi-ring shear tests, the Shear Stress Ratio (*SSR*) is transferred to modified *SSR* ($SSR=(\tau_{a\theta})_{max}/(\tau_{max})$. However, this ratio cannot be used in FL test because applied shear stress is zero and modified *SSR* also equals to zero. Besides, the maximum shear stress, $(\tau_{a\theta})_{max}$, already exists in $(R_s)_{ave}$. Based on above reasons, the shear stress ratio is modified to Equation (5-6).

$$SSR = \frac{1}{\tau_{max}} \tag{5-6}$$

where τ_{max} is shear strength.

Adding modified *SSR* and $(R_s)_{ave}$ to UIUC model, modified UIUC model for multi-ring shear tests (both ML test and FL test) is obtained (Equation (5-7)).

$$\varepsilon_p(N) = AN^B{(\sigma_a)_{max}}^C(\frac{1}{\tau_{max}})^D exp\ (E\frac{(\tau_{a\theta})_{max}}{(\sigma_a)_{max}}) \tag{5-7}$$

Before applied this equation on predicting permanent deformation of unbound aggregate materials, normalization should be finished. A normalized equation is shown in Equation (5-8).

$$\varepsilon_p(N) = AN^B\left(\frac{(\sigma_a)_{max}}{p_a}\right)^C(\frac{p_a}{\tau_{max}})^D\ exp\left(E\frac{(\tau_{a\theta})_{max}}{(\sigma_a)_{max}}\right) \tag{5-8}$$

where p_a means the atmospheric pressure, equals to 101 kPa in this study.

All necessary input parameters, stress state and shear strength, for regression analysis with modified UIUC model are shown in Table 5-1 and 5-2. Noticed that, during regression analysis, real stress condition which is detected by transducer but not the proposed stress condition was used.

Regression analysis results with this model are shown in Table 5-3. The R^2 value is high enough to prove the applicability of modified UIUC model. As a supplement to the R^2, the value of Root Mean Square Error (RMSE) is also calculated. The value of RMSE is also low enough to validate the accuracy of this model. Figure 5-4 and 5-5 compare the measured experimental data and the permanent deformation model predictions.

Table 5-3 Results of regression analysis through modified UIUC model

Test materials	Test types	A	B	C	D	E	R^2	RMSE
C-9.5	FL	0.55174	0.12753	1.31838	0.78153	—	0.951	0.059
	ML (15kPa)	0.85226	0.11425	1.11295	1.09863	2.72659	0.959	0.148
	ML (30kPa)	0.57746	0.15822	1.73123	0.67476	3.02101	0.900	0.428
RC-9.5	FL	0.99402	0.09052	0.68875	0.86966	—	0.932	0.097
	ML (30kPa)	1.60651	0.13132	0.88051	0.95224	0.29498	0.980	0.162

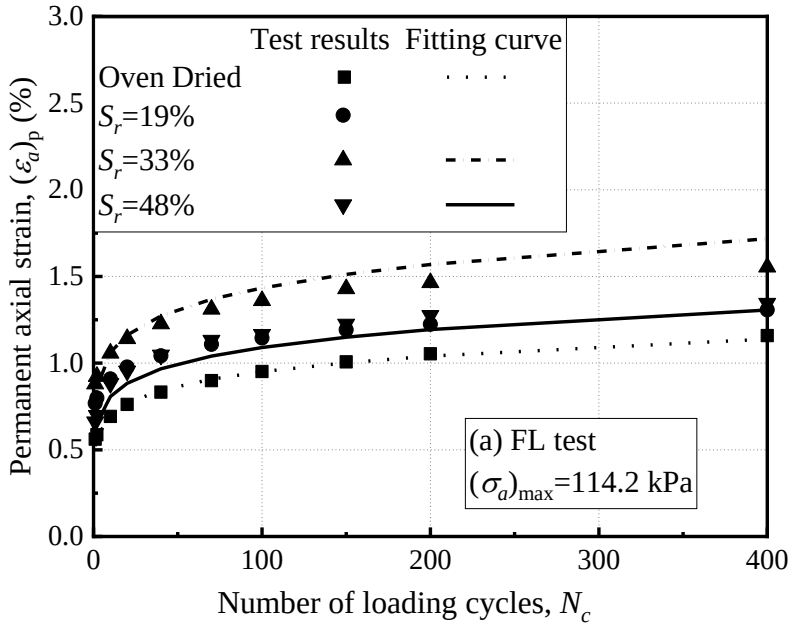

(a) FL test

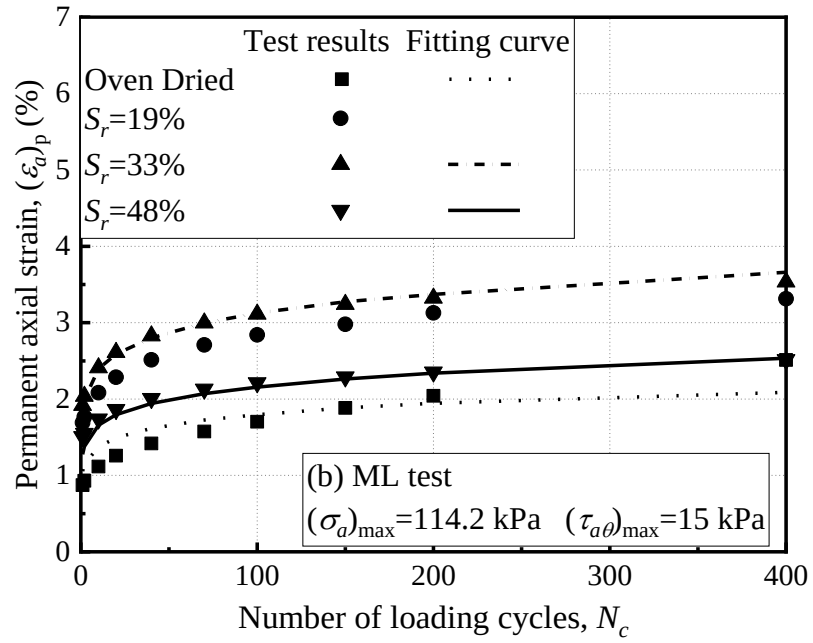

(b)ML test ($(\tau_{a\theta})_{max}$ =15 kPa)

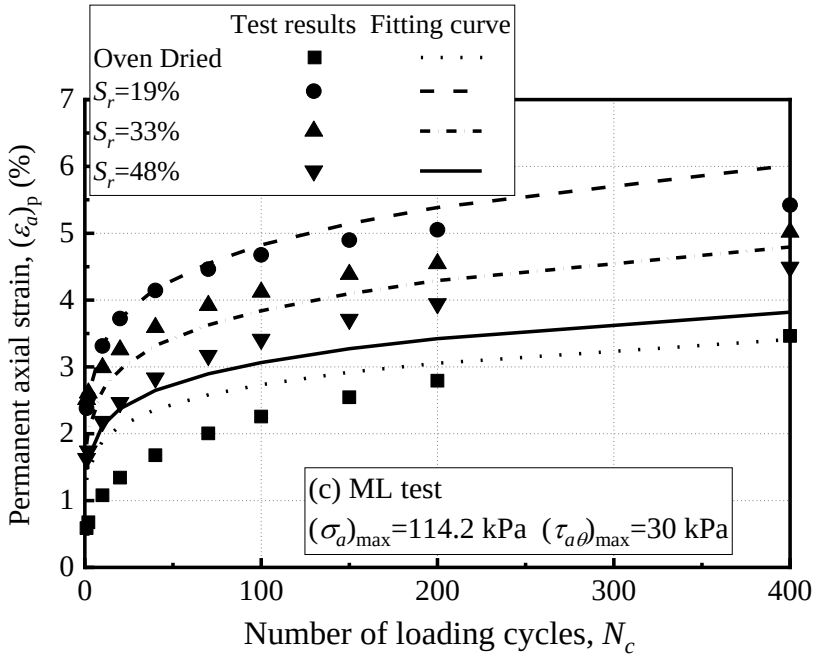

(c)ML test ($(\tau_{a\theta})_{max}$ =30 kPa)

Figure 5-4 Estimation of the permanent axial strain of C-9.5

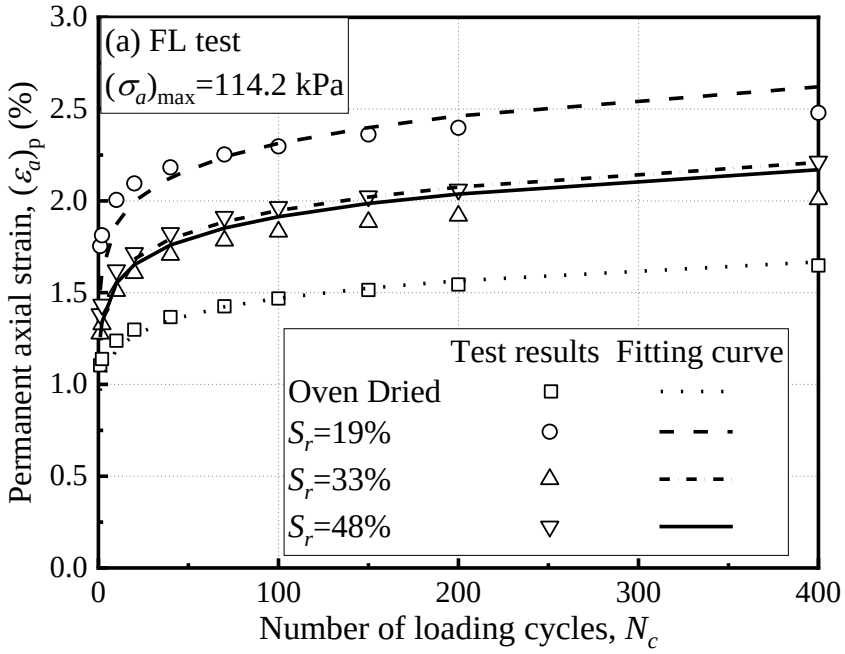

(a) FL test

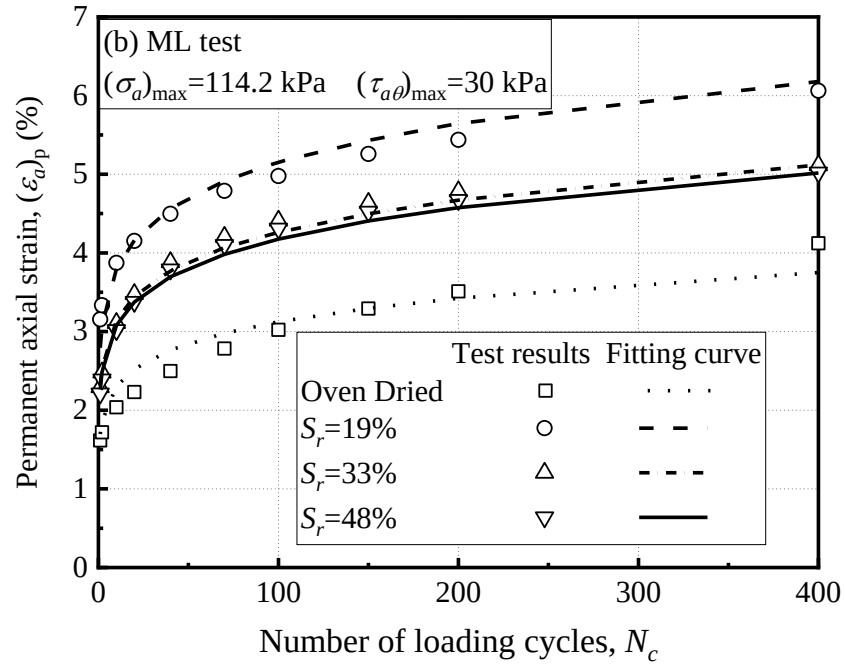

(b)ML test

Figure 5-5 Estimation of the permanent axial strain of RC-9.5

In Figure 5-4(a) and (b), there is only three approximation line but not four, the curve of S_r=19% is excluded. For materials with lowest shear strength, they should have the largest deformation. This phenomenon may due to some experimental errors. For example, the suction

cannot be controlled in this apparatus and the uniformity of water may not be ensured. Except these two (C-9.5 with S_r=19% in FL test and ML test with 15 kPa maximum shear stress), all other fitting curve through modified UIUC model shows good consistency with test results.

Moreover, if the newly added parameter, $(R_s)_{ave}$, could connect regression analysis results between FL test and ML test, then it should also be capable to connect regression analysis results between repeated loading triaxial test and ML test, because FL test is similar with repeated loading triaxial test. In other words, when test results obtained from laboratory test without PSAR times this new parameter, it can be treated as test results with PSAR. A large amount of test data obtained from traditional repeated loading triaxial test could be closer to an in-situ condition.

To check the applicability of this newly added parameter, when conducting regression analysis for ML test results, the value of A, B, C, and D were fixed to the same value obtained from FL regression analysis results. The results are shown in Figure 5-6 and Table 5-4.

Table 5-4 Results of regression analysis through modified UIUC model with fixed parameters

Test materials	Test types	A	B	C	D	E	R^2	RMSE
C-9.5	FL	0.55174	0.12753	1.31838	0.78153	—	0.951	0.059
	ML (15kPa)	0.55174	0.12753	1.31838	0.78153	5.60922	0.910	0.213
	ML (30kPa)	0.55174	0.12753	1.31838	0.78153	3.77173	0.866	0.460
RC-9.5	FL	0.99402	0.09052	0.68875	0.86966	—	0.932	0.097
	ML (30kPa)	0.99402	0.09052	0.68875	0.86966	2.91403	0.922	0.310

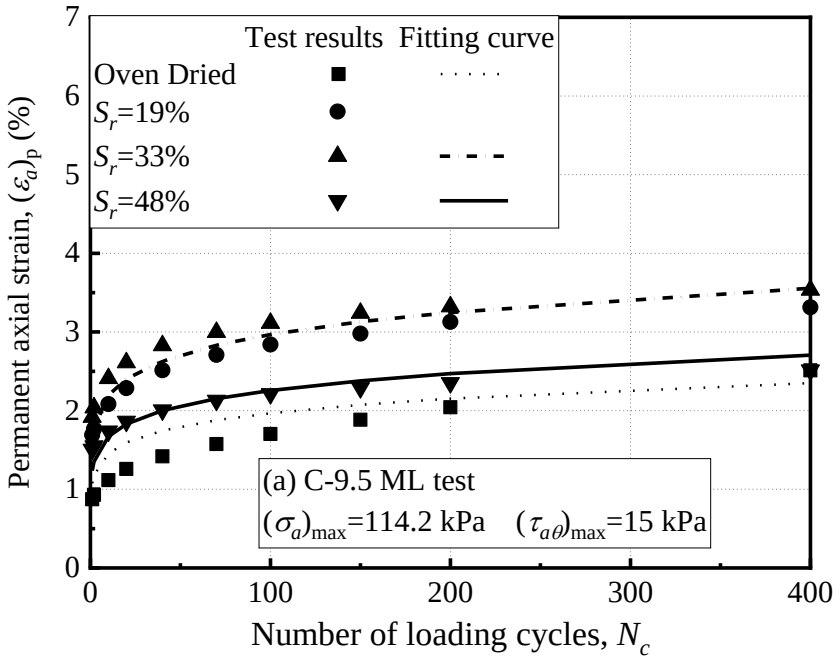

(a)C-9.5 in ML test ($(\tau_{a\theta})_{max}$ =15 kPa)

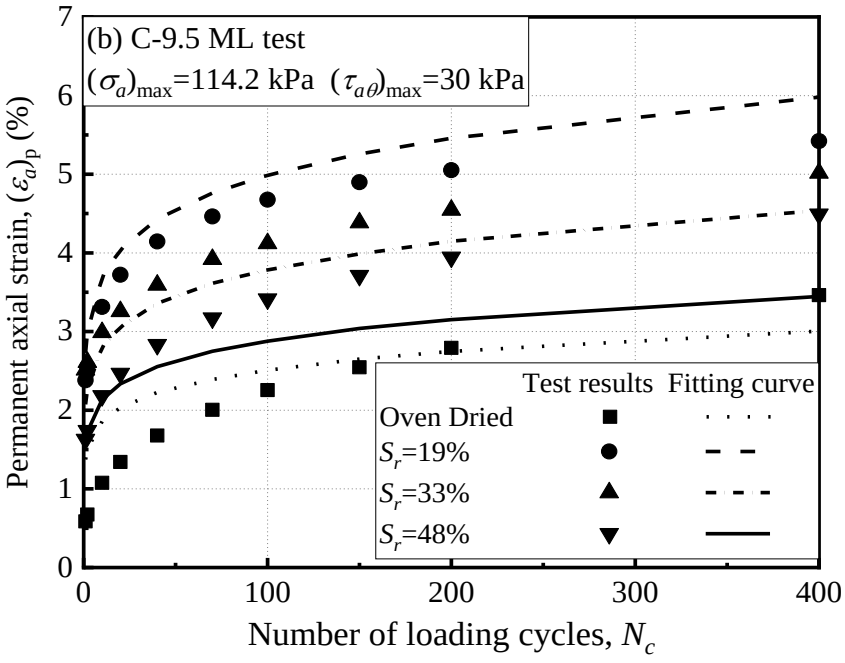

(b)C-9.5 in ML test ($(\tau_{a\theta})_{max}$ =30 kPa)

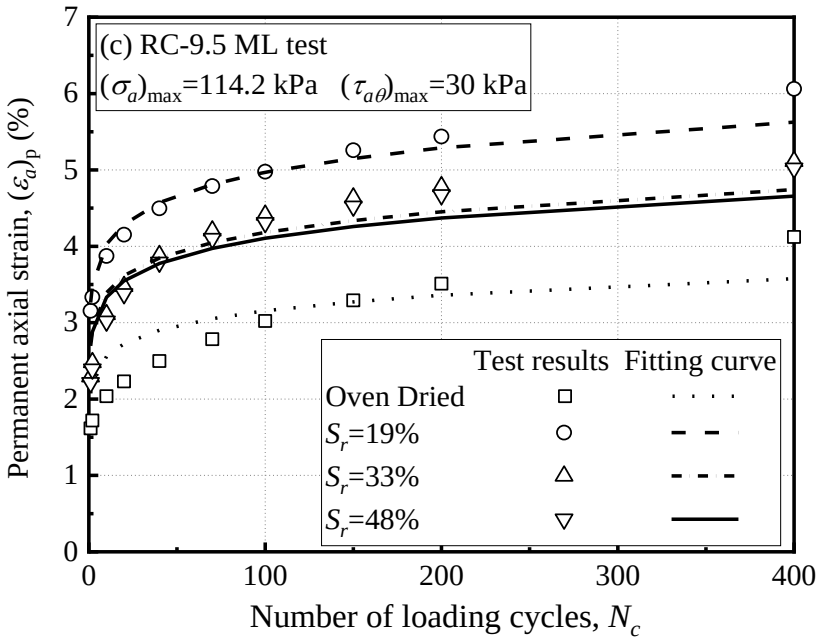

(c) RC-9.5 in ML test

Figure 5-6 Estimation of the permanent strain of C-9.5 and RC-9.5 with fixed A, B, C, D

Compare with Table 5-4 and 5-5, the R^2 value decreases a little but still higher than 0.9, except ML test (maximum shear stress of 30 kPa) of C-9.5. Small variance of RMSE value proves the reliability of this fixed-parameter model, though this value increases a little. This result illustrates the applicability of $(R_s)_{ave}$.

As a result, modified UIUC model displays good applicability on test results of multi-ring shear test. Moreover, all parameters have clear physical significance, parameter *A* represents the initial permanent strain. Parameter *B* represents the development of permanent strain with the number of loading cycles. Parameters *C* reflects the effect of applied axial stress on permanent strain. Parameter *D* captures the effect of shear strength on permanent strength. Parameter *E* represents the effect of principal stress axis rotation on permanent strain. Especially parameter *E*, this value connects test results obtained from laboratory test with and without PSAR. After calibration of these five parameter values, this new model could be used in engineering design.

As this apparatus applies both axial stress and shear stress directly, principal stresses can be calculated through Equations (5-9) to (5-12).

$$\sigma_1 = \frac{\sigma_a + K_0\sigma_a}{2} + \frac{\sqrt{(\sigma_a - K_0\sigma_a)^2 + 4\tau_{a\theta}{}^2}}{2} \quad (5\text{-}9)$$

$$\sigma_2 = K_0\sigma_a \tag{5-10}$$

$$\sigma_3 = \frac{\sigma_a + K_0\sigma_a}{2} - \frac{\sqrt{(\sigma_a - K_0\sigma_a)^2 + 4{\tau_{a\theta}}^2}}{2} \tag{5-11}$$

$$K_0 = 1 - \sin\phi' \text{ (Jáky's formula)} \tag{5-12}$$

where K_0 is coefficient of earth pressure at rest; ϕ' is effective internal friction angle; σ_a is applied axial stress; $\tau_{a\theta}$ is applied shear stress.

As the effective friction angle varies with moisture content, the value of K_0 also varies with moisture content. As a result, the principal stresses also vary with moisture content. To clearly show the level of principal stress axis rotation, three parameters could be calculated as the direction of major principal stress (Equation (5-13)), stress ratio (Equation (5-14)), and principal stress parameter (Equation (5-15)).

$$\alpha = \sin^{-1}\sqrt{\frac{\sigma_2 - \sigma_3}{\sigma_1 - \sigma_3}} \tag{5-13}$$

$$\eta = \frac{q}{p'} \tag{5-14}$$

$$b = \frac{\sigma_2 - \sigma_3}{\sigma_1 - \sigma_3} \tag{5-15}$$

where η is stress ratio, which is composed of two stress invariants, mean normal stress, p', and deviator stress, q. b is the principal stress parameter, which describes the relative magnitudes of the three principal stresses. α is the angle of principal stress axis rotation. Mean normal stress, p', and deviator stress, q, are calculated through Equations (5-16) and (5-17).

$$p' = \frac{\sigma_1 + \sigma_2 + \sigma_3}{3} \tag{5-16}$$

$$q = \sqrt{\frac{1}{2}\{(\sigma_1 - \sigma_2)^2 + (\sigma_2 - \sigma_3)^2 + (\sigma_1 - \sigma_3)^2\}} \tag{5-17}$$

As mentioned before, the effective friction angle and K_0 vary with moisture content. As a result, the principal stresses and three parameters also vary with moisture content. It is reasonable to conclude that, the effect of principal stress axis rotation is also influenced by moisture content.

Figure 5-7 shows how moisture content affects the direction of major principal stress. It is noted that the sequence of η from high to low is oven-dried, S_r=48%, S_r=33%, S_r=19% when other test conditions are same. Besides, this sequence is also the narrowest amplitude of α to widest. Moreover, as shown in Figure 5-4, this sequence of the smallest permanent strain to the largest is same as oven-dried, S_r=48%, S_r=33%, S_r=19%. As a result, it is reasonable to conclude that η and

α are affected by moisture content when test material and applied stress are same. Moreover, the greater α, the greater the permanent strain.

As shown in Figure 5-8 (a), increasing shear stress amplitude from 15 kPa to 30 kPa, the magnitudes of α for specimens with different moisture contents becomes similar and the value of E decreases, which implies that the effect of moisture content on α is also influenced by the stress state. To be specific, α for specimens with different moisture contents varies from 24.74° to 30.16° with 15 kPa shear stress amplitude whereas it only varies from 33.48° to 36.86° with 30 kPa shear stress. As shown in Figure 5-8 (b), the value of E in modified UIUC model has a positive relation with increment of α (difference between maximum and minimum α under the same shear stress amplitude). Consequently, a smaller E equals to a smaller range of α, which indicates that the synergistic effect of principal stress axis rotation and change in moisture content is less significant at higher shear stress amplitude.

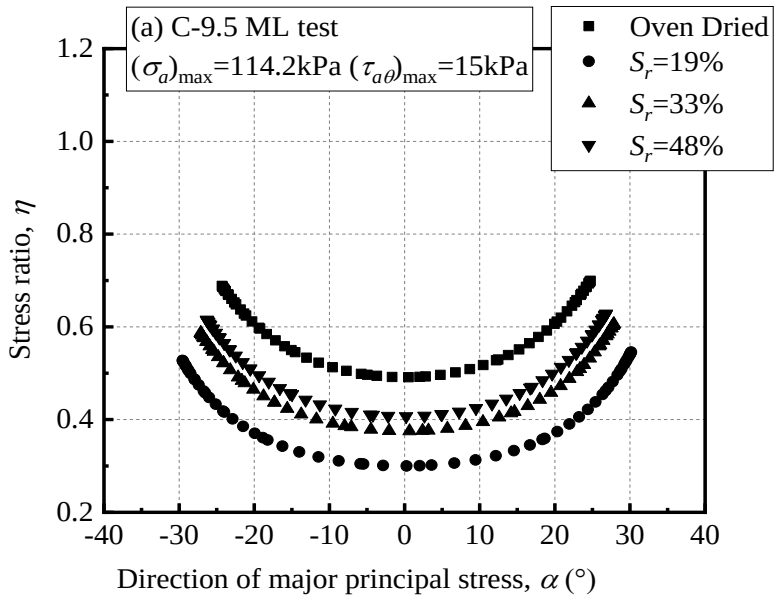

(a) C-9.5 ML test ($(\tau_{a\theta})_{max}$ =15 kPa)

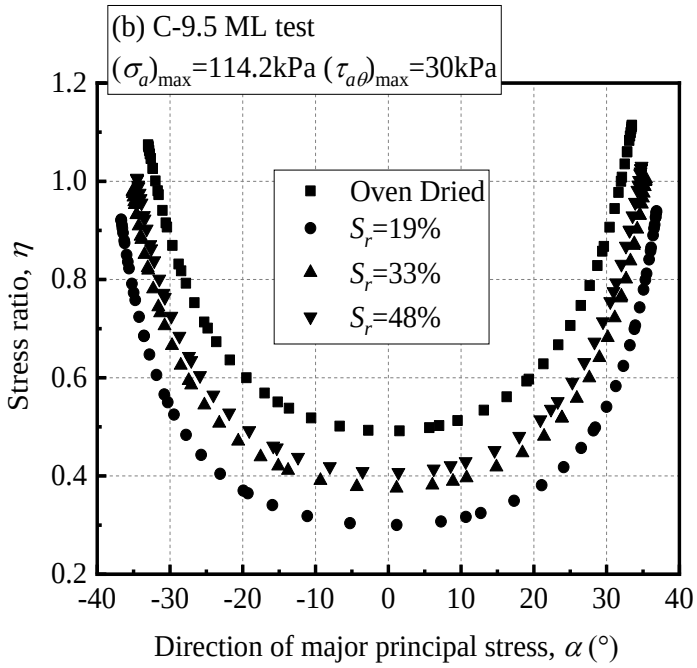

(b) C-9.5 ML test ($(\tau_{a\theta})_{max}$ =30 kPa)

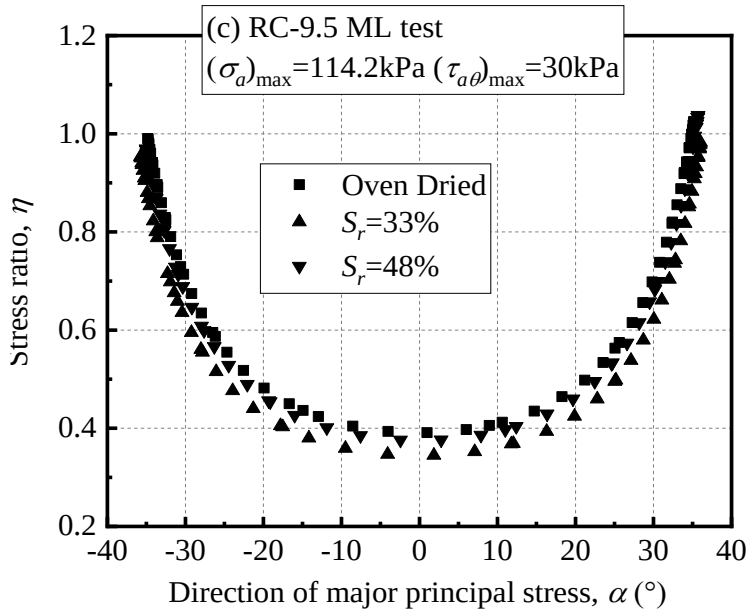

(c) RC-9.5 ML test ($(\tau_{a\theta})_{max}$ =30 kPa)

Figure 5-7 Stress paths involves principal stress axis rotation

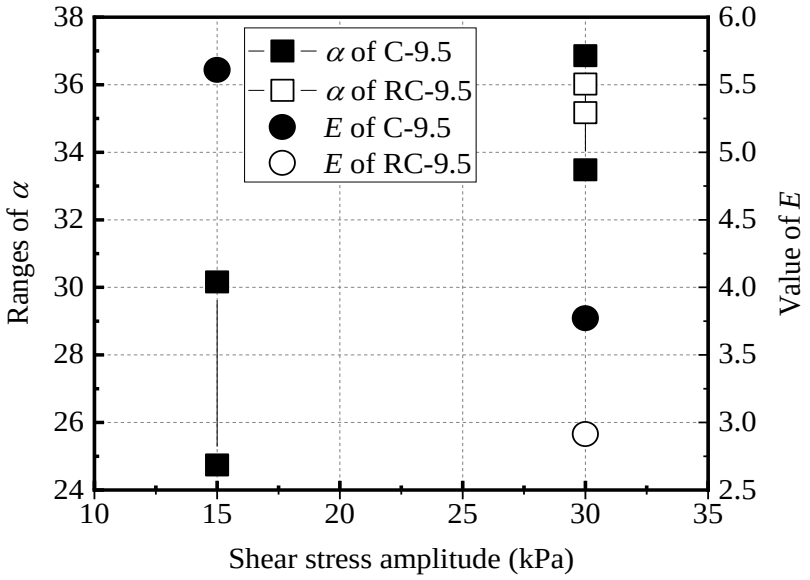

(a) Relation between shear stress amplitude and α

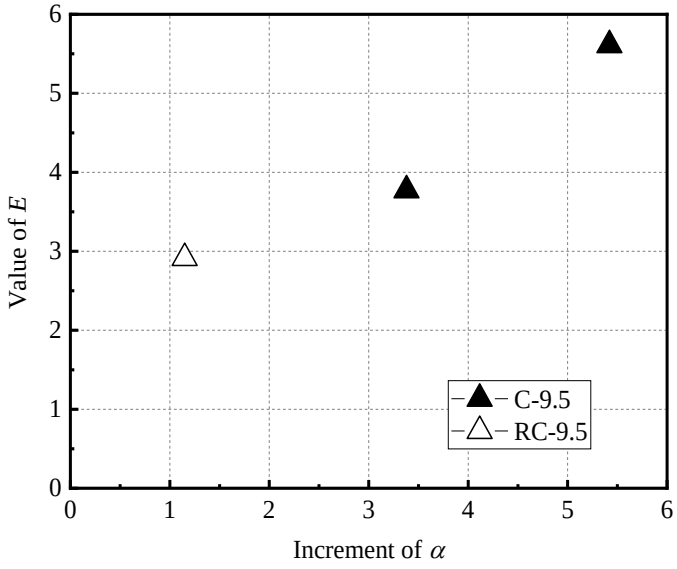

(b) Relation between E and increment of α

Figure 5-8 Synergistic effect of principal stress axis rotation and change in moisture content

5.4 MODEL IMPLEMENTATION FOR PREDICTING RUTTING DEPTH OF FLEXIBLE PAVEMENT

The first step of predicting rutting depth of base layer in flexible pavement structure through modified UIUC model is determining the stress state in base layer. In this research, the stress state in pavement flexible pavement structure is determined by the GAMES. In this

regard, a Japanese paved road model under standard design wheel loads is selected, as shown in Figure 5-9. The properties of the pavement layers, which include elastic coefficient *E* and Poisson's ratio *v*, the standard wheel load, the wheel diameter and the distance between wheels, shown in Figure 5-9, are also indicated in the Pavement Design Manual for Japanese paved roads [Japan Road Association, 2006].

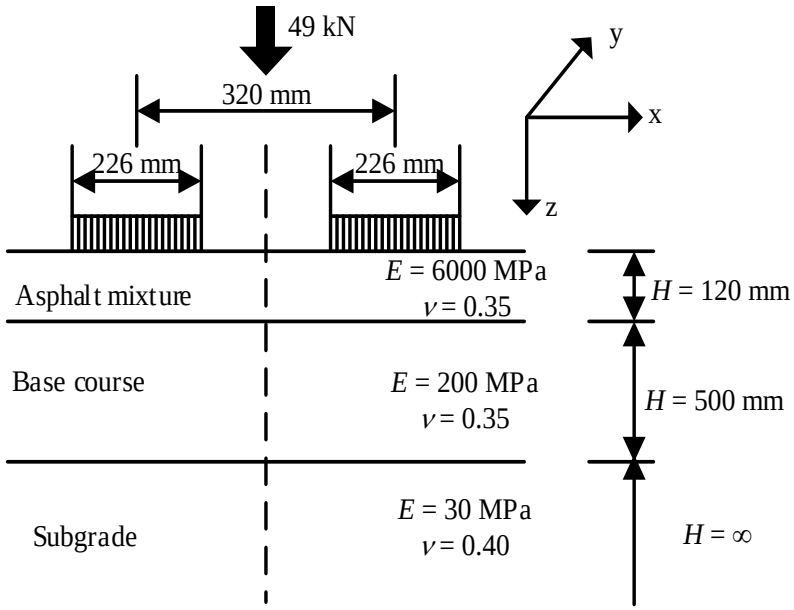

(a) Cross section

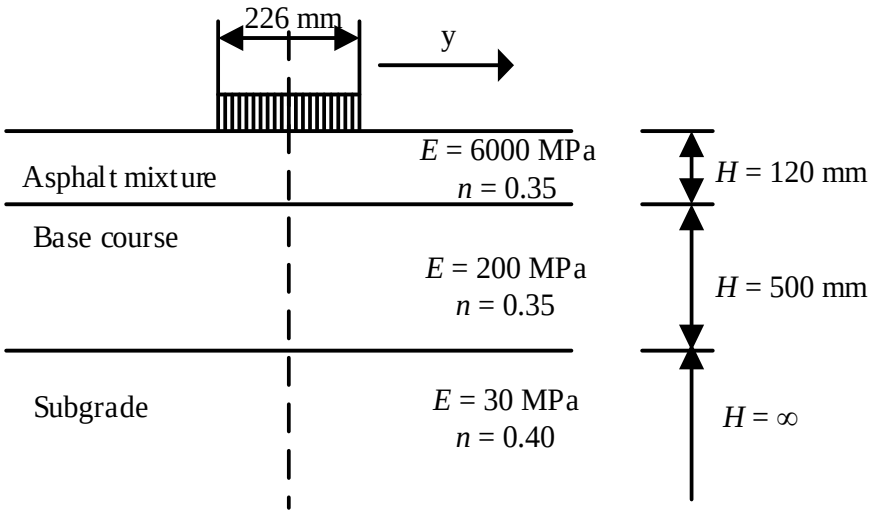

(b) Longitudinal section

Figure 5-9 Games model for stress analysis

After obtaining the stress distributions in the base layer, the multilayered incremental approach is employed to compute the total rutting depth. The following equation explains how the total rutting depth of the base layer is computed using the modified UIUC model.

$$\delta_p(N) = \int_0^h AN^B \frac{[(\sigma_a)_{max}(z)}{p_a}]^C (\frac{p_a}{\tau_{max}})^D \exp\,(E \frac{[(\tau_{a\theta})_{max}(z)]}{[(\sigma_a)_{max}(z)]}) \, dz \quad (5\text{-}18)$$

where $\delta_p(N)$ is rutting depth of base course, h is total height of base course, and z is depth within the base layer.

Figure 5-10 shows the predictive rutting depth at 100,000 cycles through modified UIUC model. The rutting depth of oven-dried material is smallest and material with 19% degree of saturation has the largest deformation regardless of the type of materials. Besides, the predictive rutting depth through UIUC model and MEPDG model are also shown in Figure 5-10. MEPDG gives smallest rutting depth and the predictive rutting depth of C-9.5 with different water contents are almost same, which is not consistent with test results. Predictive rutting depth through UIUC model is much larger than that of MEPDG and variates with water content. However, it gives similar rutting depth for two materials regardless of water contents, which is also not consistent with test results. Noted that modified UIUC model gives much larger rutting depth than other models. Besides, predictive rutting depth through modified UIUC model variates with different water content and materials, which is consistent with test results. One reason for this difference is that modified UIUC considers the great effect of PSAR on permanent strain and this effect is ignored by other models. As discussed before, PSAR greatly improves the permanent strain accumulation. Besides, the rutting depth of RC-9.5 with 33% and 48% degree of saturation shows small difference, though they have different estimated shear strength. This phenomenon implies a synergistic effect of change in water content and PSAR on permanent strain of unbound aggregate materials. In other words, the effect of PSAR on permanent strain accumulation may also be influenced by change in water content and this synergistic effect still needs further investigation.

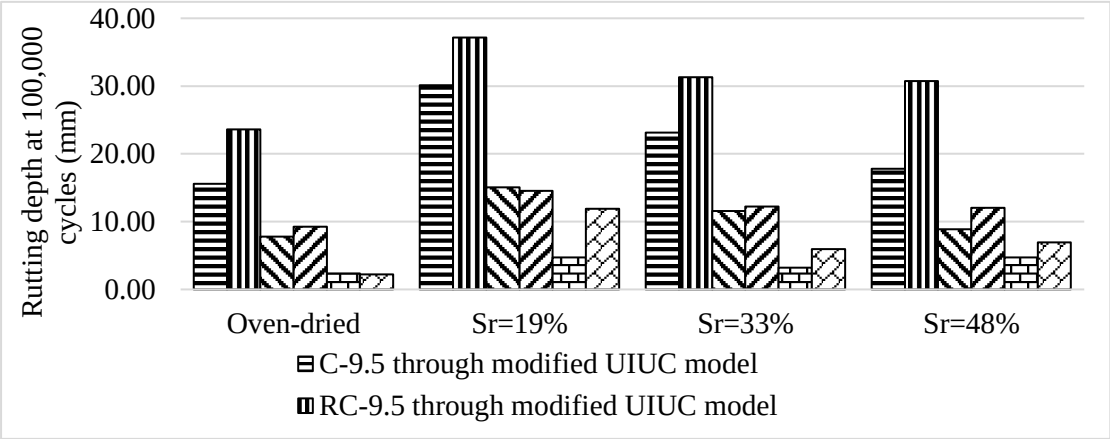

Figure 5-10 Computation of rutting depth using modified UIUC model

5.5 SUMMARY

The following findings can be mainly obtained in this chapter:

1. Shear strength has a more significant influence on permanent deformation of unbound aggregate materials rather than resilient properties.

2. Principal stress axis rotation greatly increases the permanent deformation behaviour and newly added parameter, $(R_s)_{ave}$, could connects permanent deformation behaviour with and without principal stress axis rotation.

3. Modified UIUC model show good applicability on prediction of permanent deformation of unbound aggregates with different water contents and stress states.

4. A simple framework is proposed to predict rutting depth of base layers in flexible pavement structures based on the regression analysis results obtained from modified UIUC model.

6 MODIFICATION OF PAVEMENT DESIGN METHOD

6.1 TEST PAVEMENTS

6.1.1 Pavement structures

As discussed in Introduction part, current Japanese design guide has some limitations like lacking consideration the climate effect on base course and subgrade layer, lacking consideration the effect of principal stress axis rotation and so on. To overcome such limitations, this chapter replaces constant base course and subgrade layer elastic modulus to resilient modulus related to stress states and complex climate conditions based on series of resilient modulus test under variant water contents and freeze-thaw action. Then, the rutting failure criterion structure is modified by considering generally used MEPDG model and also the effect of principal stress axis rotation through the multi-ring shear test. The applicability of modified design method is checked through comparing predicted fatigue life with actual measured fatigue performance observed from test pavements.

Civil Engineering Research Institute for Cold Region (CERI) designed and constructed eight test pavements in Hokkaido [Maruyama et al., 2006]. Figure 6-1 illustrates the structures and length of each test pavement. All eight pavement structures consist of asphalt mixture, base layer, and subgrade layer with multiple materials and thickness. Four types of asphalt mixtures are used in test pavement. Fine-graded asphalt mixture has a 0 - 13 mm gradation distribution. Middle-graded asphalt mixture has the same range of gradation distribution but more coarse aggregate. Coarse-graded and stabilized asphalt mixture have a 0 - 20 mm and 0 - 30 mm gradation distribution separately. Two types of base layer material are used as C-40, crusher-run with maximum 40 mm gradation distribution, and C-80, anti-frost crusher-run with maximum 80 mm gradation distribution. The subgrade material is a sandy soil, named as Tomakomai soil, composed of 8% clay, 13% silt, 51% sand, 28% gravel.

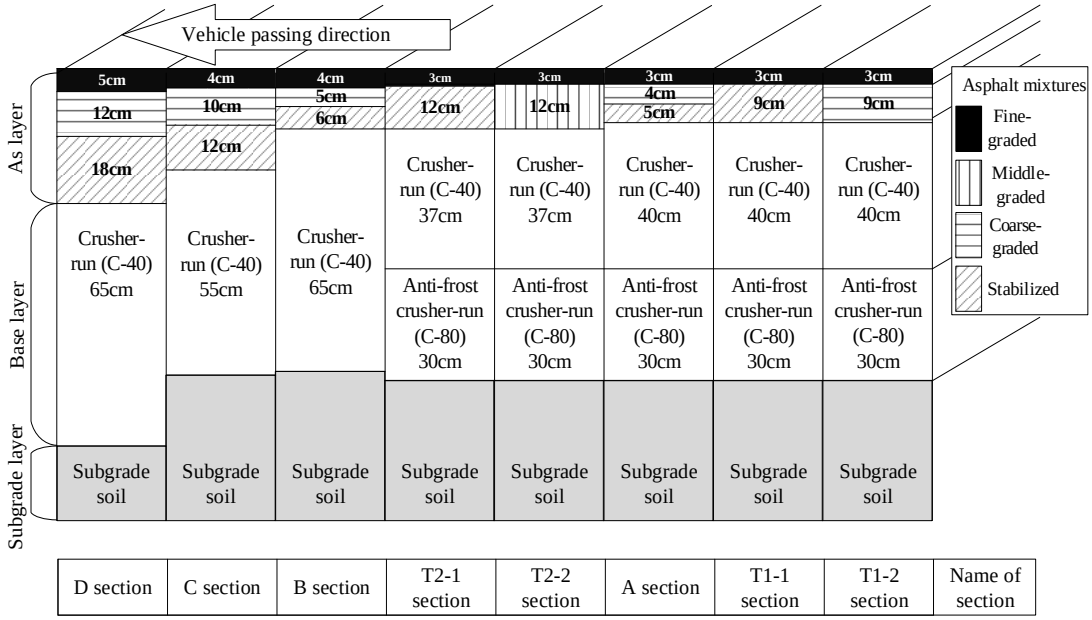

Figure 6-1 Test pavement structures

6.1.2 Traffic volume observation

CERI observed traffic volume of test road during the whole life (from 1990 to 2004). Total traffic volume, that is average annual daily vehicle (car and truck) number in one lane, is 4974 per day per lane. Truck volume, that is average annual daily truck number in one lane, is 1714 per day per lane. Wheel loads for all vehicles are in accordance with the normal distribution that ranges from 15 to 80 kN. As Japanese design guide calculate the allowable number of equivalent 49-kN wheel loads against rutting and fatigue cracking. CERI transferred the traffic volume to a 49-kN wheel loads number as 2398 per day per lane during the whole life of test pavement.

6.1.3 Climate data

Climate data are collected from Automated Meteorological Data Acquisition System (AMeDAS). Figure 6-2 plots the average monthly representative air temperature during the whole life from 1990 to 2004. These climate data are used to determine the stiffness of the asphalt layer in current Japanese design guide through Equation (3). Besides, monthly representative temperature is also used in modified design method to determine the frost-penetration depth, which highly relates to the stiffness of base and subgrade layer as frozen soil has a much larger stiffness. Determination of variant base and subgrade layer stiffness related to climate condition will be introduced in latter part.

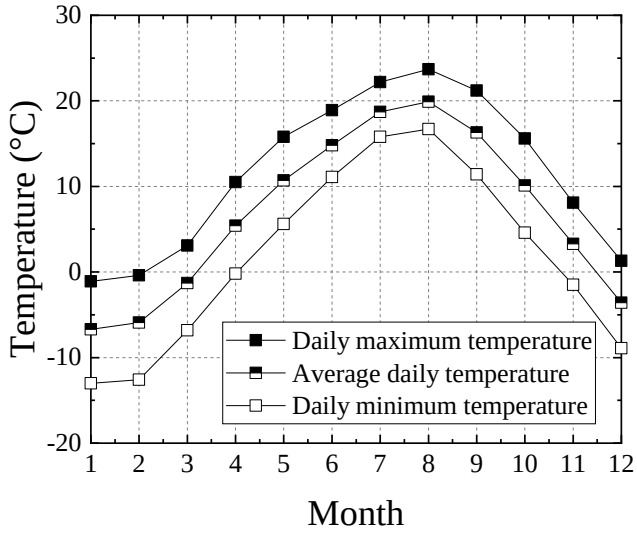

Figure 6-2 Average monthly representative air temperature

6.1.4 Predicted fatigue life with present Japanese design guide

To predict the fatigue life of eight test pavements, all eight test pavements are simplified to three-layers model in GAMES with layer thickness shown in Figure 6-1 and layer mechanical properties. Stiffness of As layer is determined through Equation 3 and monthly representative air temperature shown in Figure 6-2. Constant stiffness of base layer (E_2) and subgrade layer (E_3) through the year is set as 265MPa and 76 MPa referring to previous research (Maruyama et al., 2008). Poisson's ratio of As layer, base layer, and subgrade layer are set as 0.35, 0.35, and 0.4 separately, which come from design guide recommend value. Figure 6-3 compared predicted N_{fs} and N_{fa} through Equations (1-1) and (1-2) with actual measured failure loading number. Since Section C, D, and T2-2 did not meet fatigue cracking failure until the end, there is no actual measured N_{fa} for these sections. It is noted that, present AI model over-estimates the fatigue life, especially fatigue life against rutting. Such over-estimation is attributed to the drawbacks discussed in Introduction part.

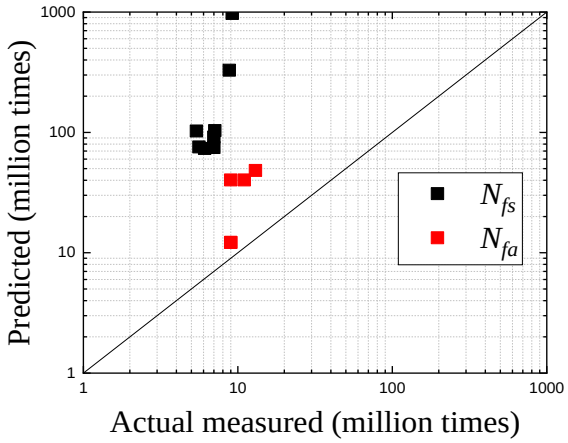

Figure 6-3 Predicted fatigue life through current Japanese design guide

6.2 VARIANT LAYER MODULI

6.2.1 Climate effect

6.2.1.1 Water content fluctuation

Since the universal model (Equation (1-6)) cannot reflect the effect of moisture content. To overcome such shortcoming, several modified models [Cary and Zapata, 2011; Liang et al., 2008; Ng et al., 2013] are proposed based on the universal model to capture the effect of moisture content on resilient modulus. Within these models, Ng model shown in Equation (6-1) adds an independent stress state variable that incorporates matric suction effects into the universal model and shows good applicability on predicting resilient modulus of unsaturated unbound granular materials through the relatively higher coefficient of determination (R^2) value than other models [Han and Vanapalli, 2016]. Monthly representative E_2 and E_3 are estimated through Ng model (Equation (6-1)) and field-measured data of water content and SWCC of base material and subgrade material.

$$M_r = k_1 p_a \left(\frac{\theta}{p_a}\right)^{k_2} \left(\frac{\tau_{oct}}{p_a} + 1\right)^{k_3} \left(\frac{\psi}{\sigma_{net}} + 1\right)^{k_4} \quad (6\text{-}1)$$

where k_1, k_2, k_3, k_4 are regression constants; p_a is atmospheric pressure and set as 101 kPa; θ is bulk stress; τ_{oct} is octahedral shear stress; σ_{net} is net mean stress (kPa), defined as [θ /3-u_a]; ψ is matric suction (kPa).

Matric suction, ψ in Equation (6-1), is determined by combining SWCC and measured long-term field measurement of degree of saturation. SWCC of C-40, composed material for base layer, and long-term field measured water content of base layer are plotted in Figure 6-4.

The effective degree of saturation, S_e, of subbase layer illustrated as the red line in Figure 6-4 (a) was calculated by using a residual degree of saturation, S_{rr}, of 32.3%, which was determined through the SWCC measured in laboratory water retentivity test and fitted curve through LG-A model [Mori et al., 2009]. Monthly average S_e is selected to determine monthly matric suction of base course. Then, monthly representative E_2 is estimated with these monthly matric suction values. It is noted that S_r during freezing season is lower than residual S_r and S_e during freezing season is consequently lower than zero. This is due to functional features of the soil moisture sensor used in the measurement. For this reason, unrealistic measured low water content during freezing season is not used. The water content just before freezing is used as representative water content for freezing season.

(a) Field measured saturation

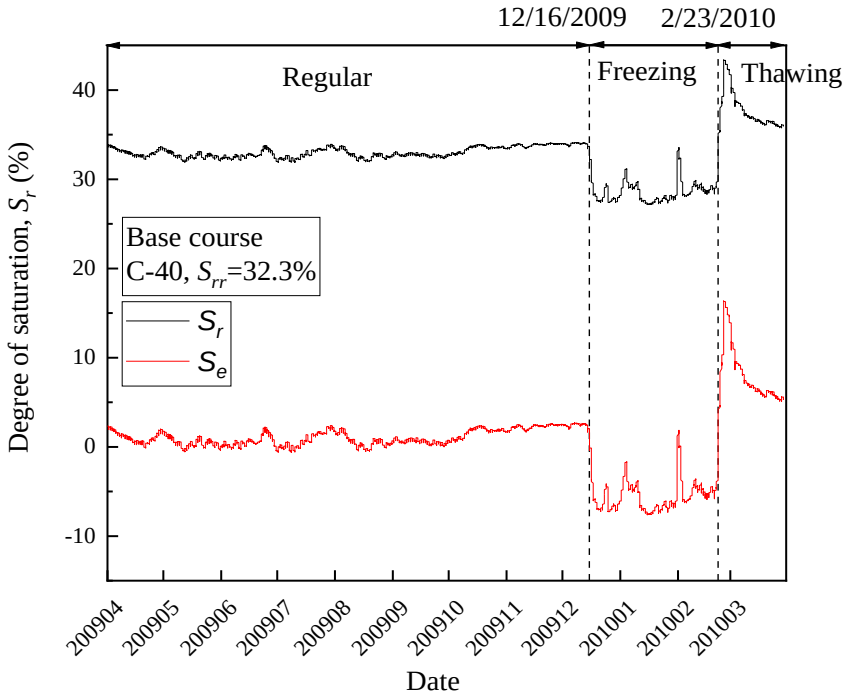

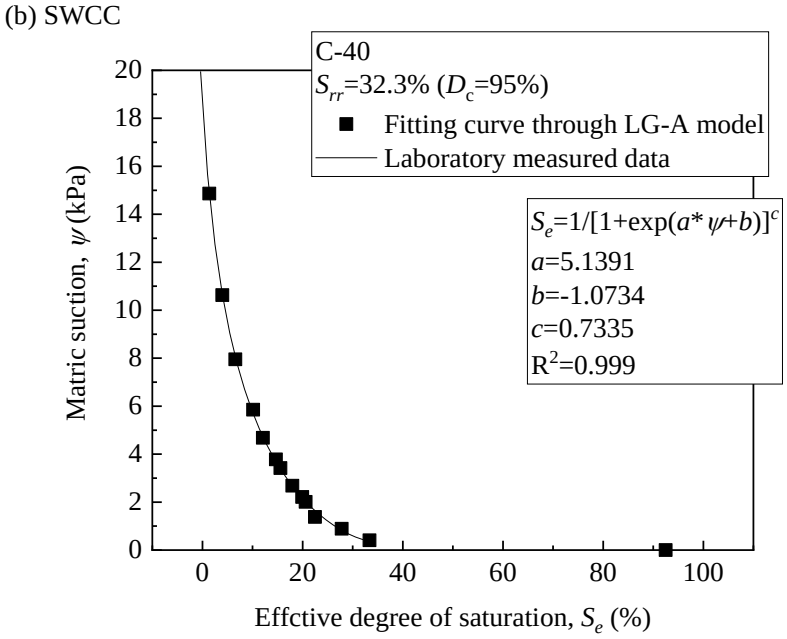

Figure 6-4 (a) Field measured base course water content and (b) SWCC of C-40

For subgrade layer, it is composed of Tomakomai soil. As the mechanical properties like resilient modulus of Tomakomai soil is under investigation, this study use Toyoura sand to represent the subgrade layer. It is assumed that effective degree of saturation, S_e, would be same in Toyoura sand subgrade and Tomakomai soil subgrade under same climate condition. S_e of subgrade layer illustrated as the red line in Figure 6-5 (a) was calculated by using a residual degree of saturation (S_{rr}) of 25.67%, which was determined through the SWCC estimated with grain-size distribution of Tomakomai soil [Fredlund et al., 2002]. Consequently, monthly average S_e is selected to determine matric suction, ψ in Equation (6-1), of subgrade layer in each month through laboratory measured SWCC of Toyoura sand and fitting curve through Fredlund-Xing model [Fredlund and Xing, 1994].

(a) Field measured saturation

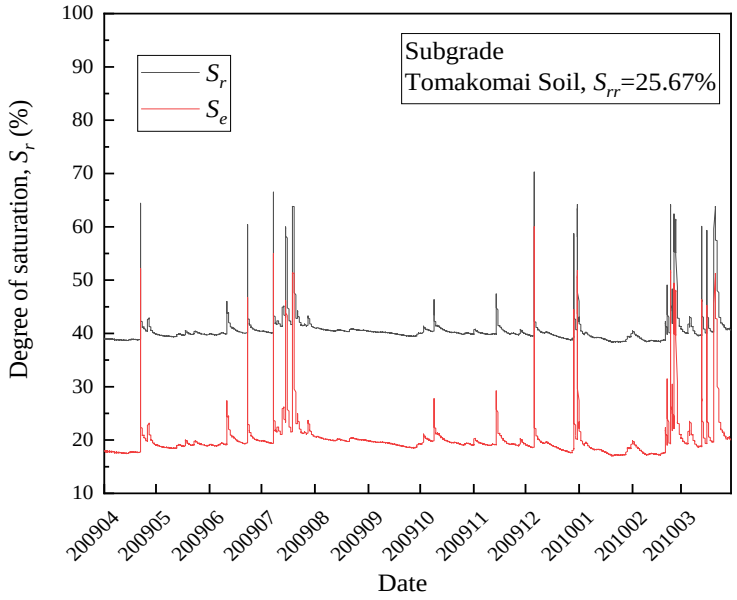

(b) SWCC

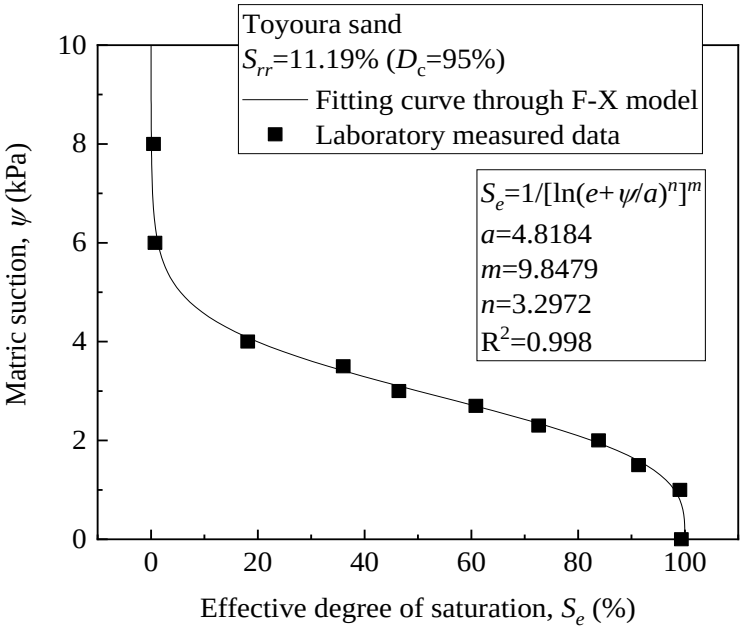

Figure 6-5 (a) Field measured subgrade layer water content and (b) SWCC of Toyoura sand

The value of constants, k_1 to k_4, in Ng model (Equation (6-1)) are determined through regression analysis on resilient modulus test results of C-40 and Toyoura sand with variant water contents. Resilient modulus of C-40 with three water contents, air-dried (S_r=8.2%), unsaturated (S_r=36.7%), saturated (S_r=100%), are determined through medium-size triaxial apparatus. More details about the apparatus and test procedure could be found in the previous

study [Ishikawa et al., 2019a]. Resilient modulus of Toyoura sand with two water contents, unsaturated (S_r=40%), saturated (S_r=100%), are determined through freeze-thaw triaxial apparatus as discussed in Chapter 4. Consequently, Figure 6-6 and 6-7 show the laboratory measured resilient modulus of C-40 and Toyoura sand and corresponding fitting surface through Ng model respectively. Table 6-1 summarized the value of constants, k_1 to k_4, in Ng model of C-40 and Toyoura sand.

(a) Saturated

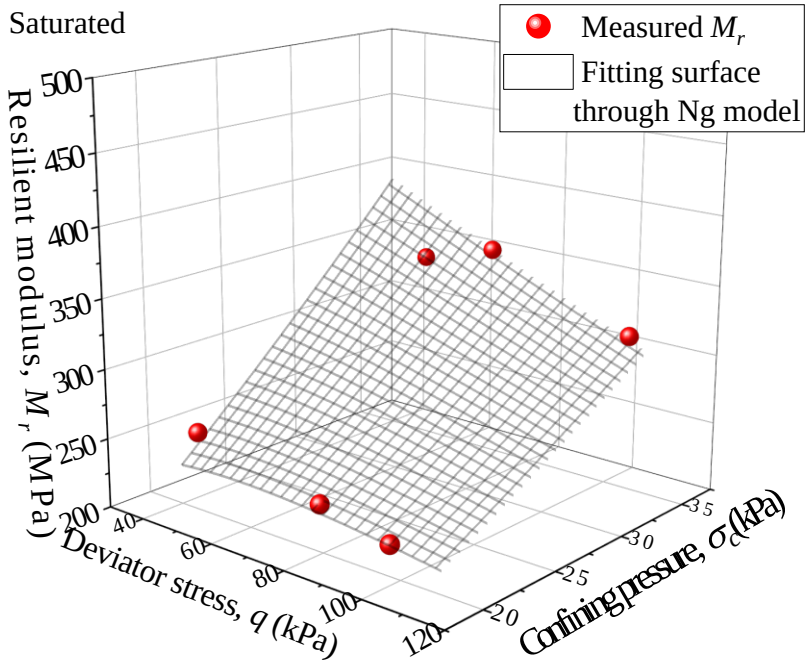

(b) Unsaturated

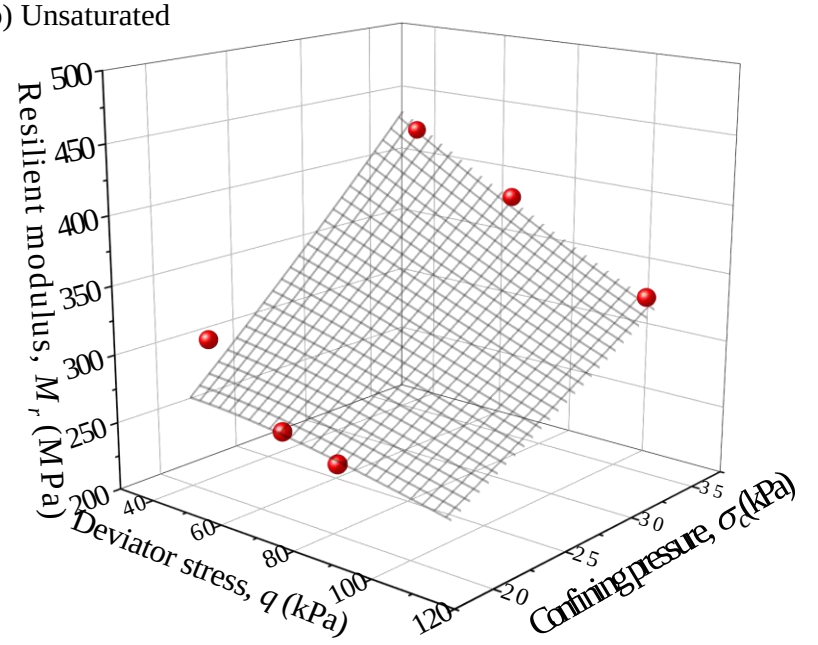

(c) Air-dried

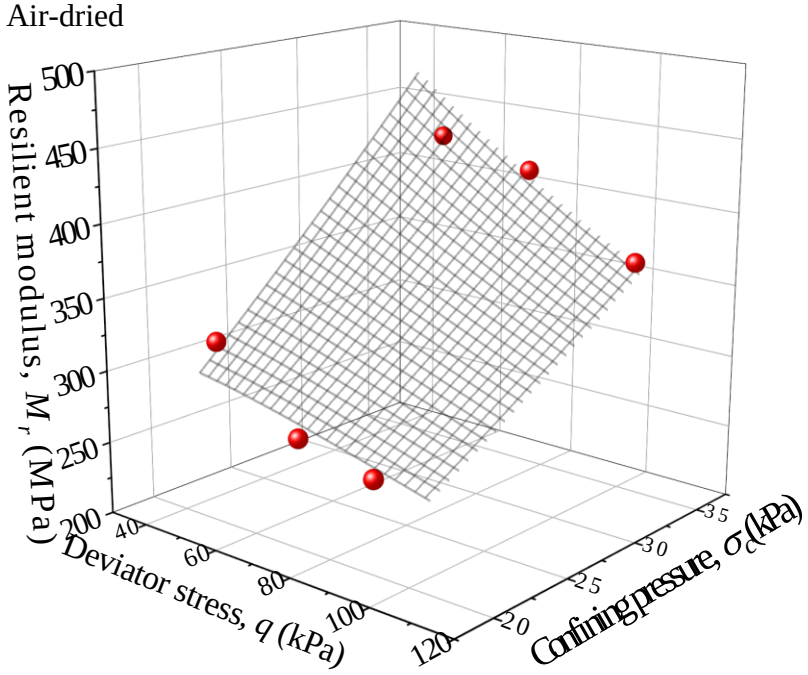

Figure 6-6 Resilient modulus of C-40 under different water contents

(a) Saturated

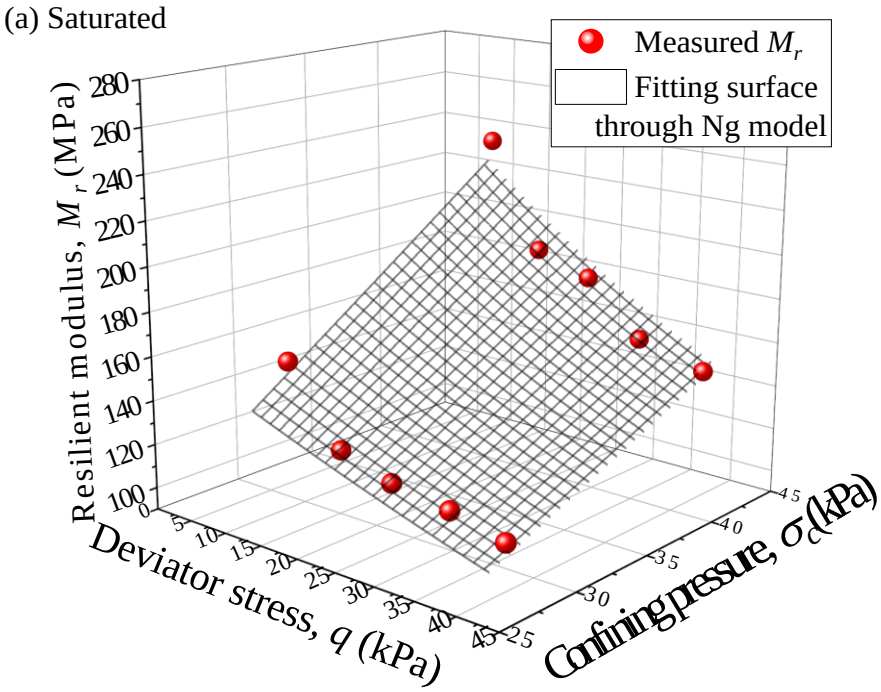

(b) Unsaturated

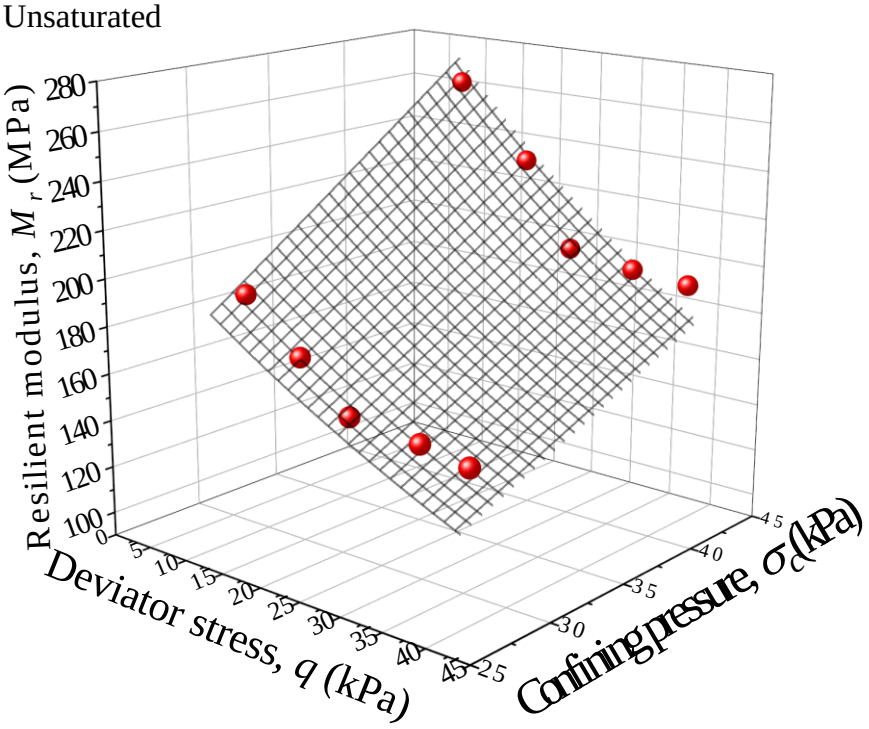

Figure 6-7 7 Resilient modulus of Toyoura sand under different water contents

Table 6-1 Value of regression constants through Ng model

	k_1	k_2	k_3	k_4	R^2
C-40	3.042	0.886	-1.696	1.076	0.939
Toyoura sand	2.103	1.065	-4.843	2.74	0.949

θ, τ_{oct}, and σ_{net} in Equation (6-1) for base layer and subgrade layer are determined with a principal stress ratio equals to 4 under 10 and 5 kPa confining pressure. It is noted that this stress condition was selected so that M_r at normal season matches layer stiffness determined in previous research [Maruyama et al., 2008]. Consequently, Table 6-2 shows the monthly representative base and subgrade layer moduli considering fluctuating water contents estimated through Ng model. A convergence analysis of layer moduli under variant stress states is discussed in later part.

Table 6-2 Monthly representative layer moduli considering fluctuating water contents

Name	Elastic moduli (MPa)											
	Jan	Feb	Mar	Apr	May	Jun	Jul	Aug	Sep	Oct	Nov	Dec
Base layer, E_2	217	209	143	193	195	195	174	185	195	191	189	208

Subgrade layer, E_3	77	75	61	76	76	71	69	76	76	76	76	75

6.2.1.2 Freeze-thaw action

When considering the climate effect, that is freeze-thaw action and seasonal fluctuation in water content, on the stiffness of base and subgrade layer, the monthly representative elastic moduli were divided into three types of seasonal *E* values (*E* for freezing season, thawing season, and regular season except for freezing and thawing seasons) for the simplicity of the fatigue life analysis.

Since there is no freeze-thaw effect during the regular season, the *E* value for the regular season is estimated by Ng model as shown in Equation (6-1) in a same way introduced in last section.

The E_2 and E_3 value for freezing season is set as 600 MPa and 200 MPa separately, according to back analysis of FWD test results [Ishikawa et al., 2019a]. In addition, this study assumes that when the average frost-penetration depth for the month gets into the base or subgrade layer regardless of deep or shallow, the *E* increases due to freezing. Here, the average frost-penetration depth (*z*) was calculated by substituting the freezing index calculated from the daily mean air temperatures measured by AMeDAS into the modified Berggren formula [Aldrich Jr, 1956] shown below:

$$z = \alpha\sqrt{\frac{172800F}{(L/\lambda)_{eff}}} \tag{6-2}$$

where α is a correction coefficient; *F* is a freezing index which is the average air temperature during freezing season multiplied by its duration in days; $(L/\lambda)_{eff}$ is an effective ratio of *L* to λ; *L* is the latent heat of soil; λ is a thermal conductivity of the soil.

The *E* value for thawing season stands for the average value between the moduli just after thawing, corresponds to the highest water content during thawing season, and the moduli already recovered, corresponds to the lowest water content during thawing season. The *E* value after thawing is estimated by modified Ng model, which is proposed in Chapter 4, with considering climate effect, F_{clim}. By adding nre parameter F_{clim} into Ng model as shown in Equation (6-3), modified Ng model captures the complex climate effect. The recovered *E* value is estimated through Equation (6-1) since the effect of freeze-thaw is already excluded when soil is fully recovered from the freeze-thaw action.

$$M_r = F_{clim} \cdot k_1 \cdot p_a \left(\frac{\theta}{p_a}\right)^{F_{clim}\cdot k_2} \left(\frac{\tau_{oct}}{p_a} + 1\right)^{F_{clim}\cdot k_3} \left(\frac{\psi}{\sigma_{net}} + 1\right)^{F_{clim}\cdot k_4} \tag{6-3}$$

Except modified Ng model, Liang model [Liang et al., 2008] is another approach to estimate resilient modulus with changing stress states like bulk stress, octahedral shear stress, and matric suction. Equation (6-4) show the Liang model. The most difference between Liang model and Ng model is that the former one incorporates the matric suction into applied bulk stress but the latter one extends the independent stress state variable. To capture the freeze-thaw effect on resilient modulus, modified Liang model (Equation (6-5)) is built by adding a reduction factor, $f(N_F,\theta)$, on Equation (6-4.1). $f(N_F,\theta)$ is determined by freeze-thaw stiffness test, which uses number of freeze-thaw process cycles (N_F) and volumetric water content (θ) for the sample as explanatory variables.

$$M_r = k_1 p_a \left(\frac{\theta_b + \chi\psi}{p_a}\right)^{k_2} \left(\frac{\tau_{oct}}{p_a} + 1\right)^{k_3} \quad (6\text{-}4.1)$$

$$\chi = \left(\frac{(u_a - u_w)_b}{\psi}\right)^{0.55} \quad (6\text{-}4.2)$$

$$M_r = f(N_f, \theta) \cdot k_1 p_a \left(\frac{\theta_b + \chi\psi}{p_a}\right)^{k_2} \left(\frac{\tau_{oct}}{p_a} + 1\right)^{k_3} \quad (6\text{-}5)$$

For base course material, both Ng model (Equation (6-1)) and Liang model (Equation (6-4)) have high R^2 value on the unfrozen C-40 material as shown in Table 2-1. The applicability of modified Ng model (Equation (6-3)) and modified Liang model (Equation (6-5)) on freeze-thawed C-40 are checked by comparing estimated M_r with freeze-thawed $M_{r(\mathrm{CBR})}$. Freeze-thawed $M_{r(\mathrm{CBR})}$ is detected with a freeze-thaw CBR (California Bearing Ratio) test apparatus which is based on a general CBR test apparatus and improved to reproduce in a laboratory environment the freeze-thaw history expected to be applied to the base course materials in the in-situ pavement structures. A series of freeze-thaw CBR tests for C-40 was conducted under three different water contents, air-dried (S_r=12.3%), unsaturated (S_r=67%), saturated (S_r=95%), along with three different patterns of freeze-thaw history, no freeze-thaw, once freeze-thaw, and twice freeze-thaw, in order to examine the effects of freeze-thaw action and water content on the frost-heave and bearing-capacity characteristics of sub- base course material. More details about the freeze-thaw CBR test apparatus and procedure could be found in the previous study [Ishikawa et al., 2019a]. Figure 6-8 shows the $M_{r(\mathrm{CBR})}$ and estimated M_r with Equation (6-3) and (6-5). It is noted that, both models can give reasonable predicted M_r and also capture the decreasing M_r with more freeze-thaw numbers and higher water contents. Table 6-3 also shows the R^2 value, F_{clim}, and $f(N_F,\theta)$ of modified Ng model (Equation (6-3)) and modified Liang model (Equation (6-5)) on freeze-thawed $M_{r(\mathrm{CBR})}$. N_F is the number of freeze-thaw cycle and θ is volumetric water content. It is noted that when conducting regression analysis for freeze-

thawed test, only F_{clim} and $f(N_F,\theta)$ is variant and k_1 to k_4 are fixed to check the validity of newly added parameter. Both models show high accuracy (R^2>0.9).

(a) Modified Ng model

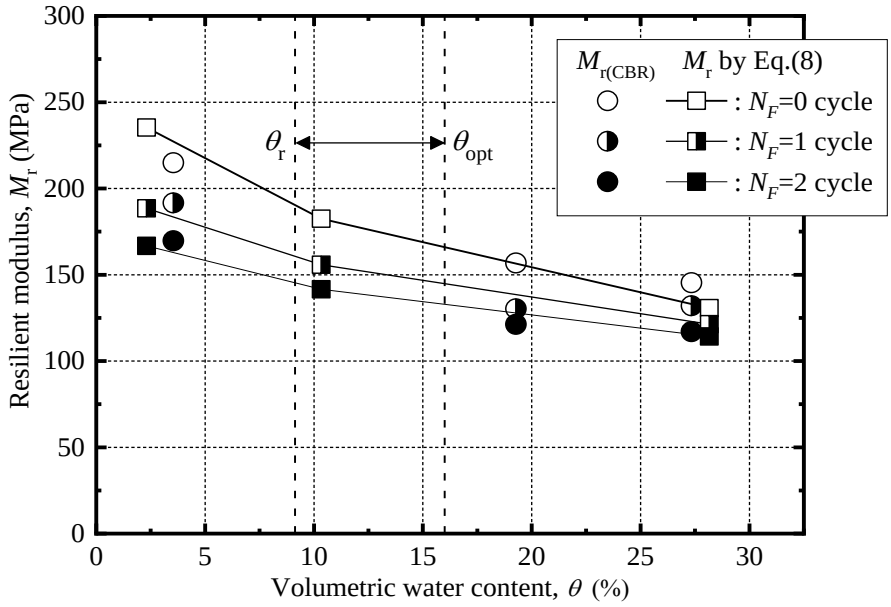

(b) Modified Liang model

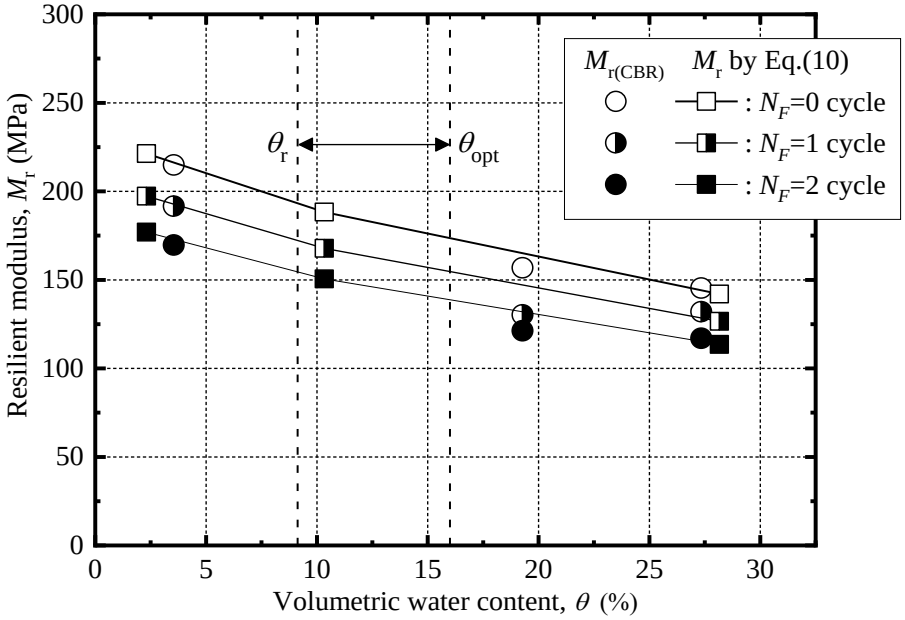

Figure 6-8 Estimated freeze-thawed C-40 resilient modulus with (a) modified Ng model and (b) modified Liang model

Table 6-3 Applicability of Modified Liang model and Modified Ng model on C-40

		k_1	k_2	k_3	k_4	F_{clim}	$f(N_F,\theta)$	R^2
U	Ng model	3.042	0.886	-1.696	1.076	—	—	0.939
	Liang model	4.861	1.525	-2.092	—	—	—	0.950
FT	modified Ng model	3.042	0.886	-1.696	1.076	0.749	—	0.921
(N_f=1)	modified Liang model	4.861	1.525	-2.092	—	—	0.891	0.991
FT	modified Ng model	3.042	0.886	-1.696	1.076	0.644	—	0.968
(N_f=2)	modified Liang model	4.861	1.525	-2.092	—	—	0.800	0.998

For subgrade material, Table 6-4 shows the applicability of Ng model (Equation (6-1)) and Liang model (Equation (6-4)) on unfrozen Toyoura sand and modified Ng model (Equation (6-3)) and modified Liang model (Equation (6-5)) on freeze-thawed Toyoura sand. Freeze-thaw resilient modulus of Toyoura sand is detected with freeze-thaw triaxial apparatus which could circulate low temperature fluids in the cap, pedestal, and inner cell to control the cap, pedestal, and around temperature of specimen separately to simulate a one-dimensional freeze-thaw action. A series of freeze-thaw resilient modulus tests for Toyoura was conducted under two different water contents, unsaturated (S_r=40%), saturated (S_r=100%), along with two different patterns of freeze-thaw history, no freeze-thaw and once freeze-thaw, in order to examine the effects of freeze-thaw action and water content on the mechanical properties of subgrade materials. Consequently, Figure 6-9 shows the freeze-thaw resilient modulus test results for Toyoura sand. It is noted that unfrozen resilient modulus test results for Toyoura sand is already plotted in Figure 6-7.

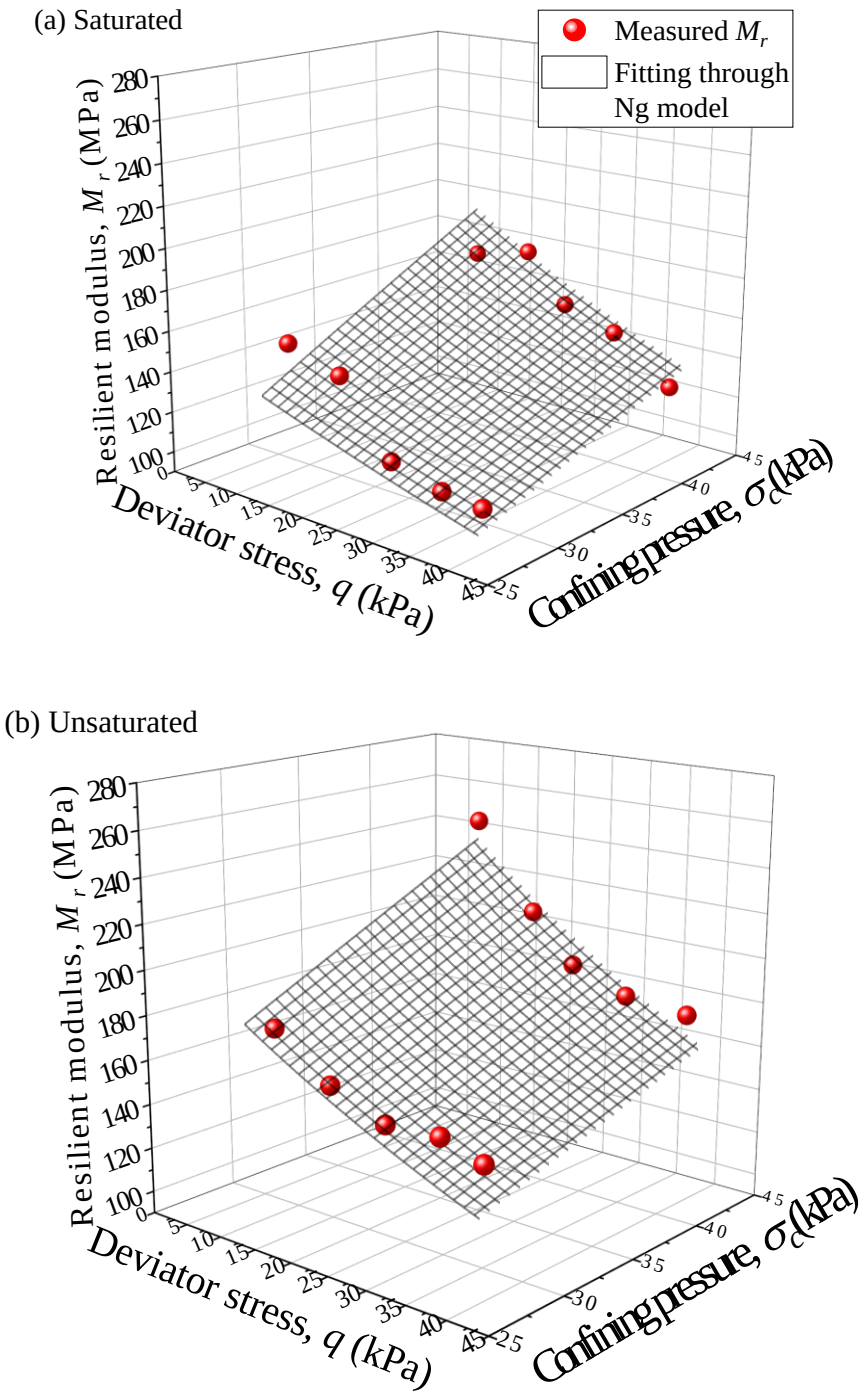

Figure 6-9 Freeze-thaw resilient modulus of Toyoura sand under different water contents

When performing regression analysis for freeze-thaw test results through modified Ng model (Equation (6-3)) or modified Liang model (Equation (6-5)), it is noted that only F_{clim} and $f(N_F,\theta)$ is variant and k_1 to k_4 are fixed to the same value obtained from regression analysis on unfrozen test results to check the validity of newly added parameter. It is recognized that Ng model shows much higher R^2 value than Liang model no matter for unfrozen or freeze-thawed

C-40. Consequently, this study uses modified Ng model to estimate resilient modulus of base layer and subgrade layer with fluctuating water content and freeze-thaw actions.

Table 6-4 Applicability of Modified Liang model and Modified Ng model on Toyoura sand

		k_1	k_2	k_3	k_4	F_{clim}	$f(N_F,\theta)$	R^2
U	Ng model	2.103	1.065	-4.843	2.74	—	—	0.949
	Liang model	2.396	0.979	-4.912	—	—	—	0.767
FT	modified Ng model	2.103	1.065	-4.843	2.74	0.885	—	0.901
	modified Liang model	2.396	0.979	-4.912	—	—	0.910	0.621

Consequently, Table 6-5 shows the monthly representative base and subgrade layer moduli estimated through modified Ng model with considering fluctuating water contents and freeze-thaw action.

Table 6-5 Monthly representative subgrade layer moduli considering climate effect

Name	Elastic moduli (MPa)											
	Jan	Feb	Mar	Apr	May	Jun	Jul	Aug	Sep	Oct	Nov	Dec
Base layer, E_2	600	600	110	193	195	195	174	185	195	191	189	208
Subgrade layer, E_3	77	200	50	76	76	71	69	76	76	76	76	75

6.2.2 Stress state

As discussed in introduction part, present Japanese design guide use constant elastic moduli of base layer and subgrade layer to calculate the strains under 49-kN wheel load. To overcome the limitation that unchangeable layer moduli under variant stress states caused by different layer thickness, the widely used resilient modulus in MEPDG, which changes with different stress states like deviator stress and confining pressure, is applied in this study to estimate the layer stiffness precisely. A convergence analysis of M_r is necessary to determine the reliable layer stiffness under 49-kN wheel loads since M_r affects and is affected by the stress states. The convergence analysis is conducted through following steps:

1) Input $E_1/E_2^1/E_3^1$ in the GAMES to obtain the stress states in base layer and subgrade layer.

According to previous researches [Huang, 2004; Japan Society of Civil Engineers 2015], stress states in two points shown in Figure 6-10 are chosen to estimate *E* for whole base and subgrade layer.

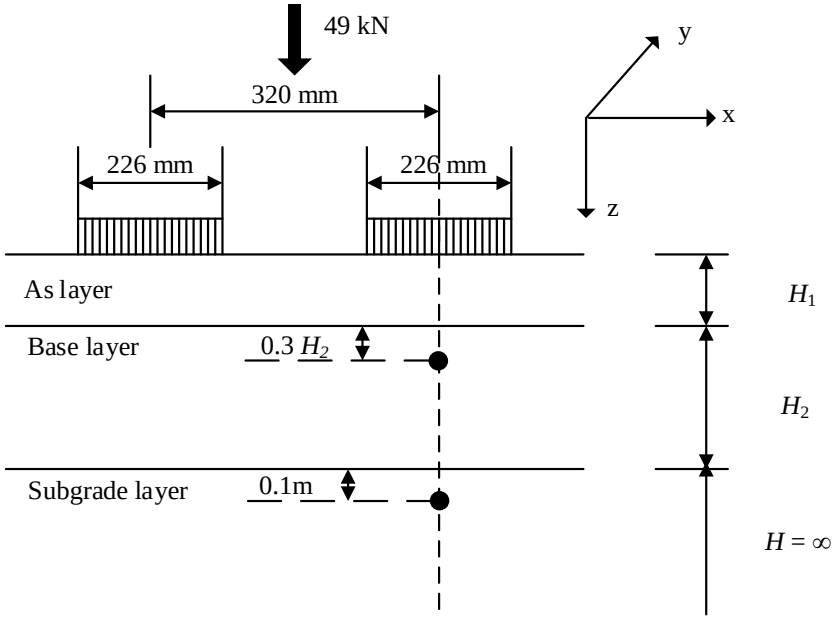

Figure 6-10 Stress states calculation points in base and subgrade layer

2) Substitute the stress states obtained in step 1 into modified Ng model to obtain new E_2^2/ E_3^2.

3) Step 1 and 2 are repeated until the error calculated in following equation is less than 1%.

$$e_{rr} = \frac{|E^{i-1} - E^i|}{E^i} \times 100 \qquad (6\text{-}6)$$

where E^i and $E^{i\text{-}1}$ is the layer modulus estimated in *i* th and *i*-1th iterations.

Based on this convergence analysis sequence, Figure 6-11 shows the development of estimated resilient modulus of base layer and subgrade layer with number of iterations in normal season (Aug). It is noted that all moduli are stable after 2-4 iterations. Besides, convergent E_2 decreases in all pavement sections and convergent E_3 decreases in section A, B, C while increases in section D compared with elastic moduli without convergence analysis. Resilient moduli in other month show similar tendency that E_2 decreases in all pavement sections and E_3 decreases in section with thin As layer while increases in section with thick As layer.

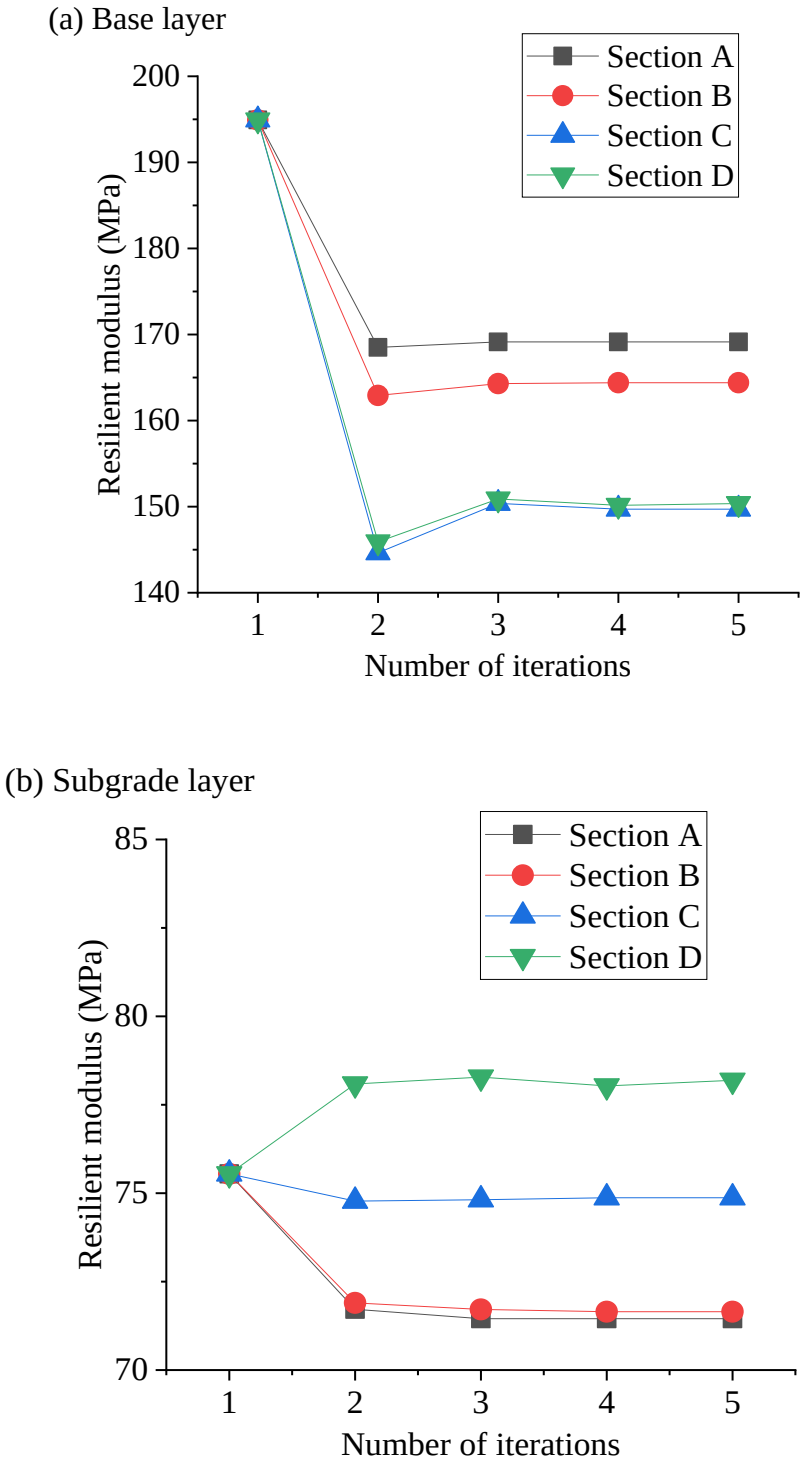

Figure 6-11 Iteration of resilient modulus of (a) base layer and (b) subgrade layer

Different increasing or decreasing tendency and level comes from the variant stress states when pavement structures changing. To clearly discuss how pavement structures and stress states influence the resilient modulus at stable condition, Figure 6-12 compares resilient modulus, strain, and stress states in different sections. Since As layer thickness increases from

section A to D, it is concluded that E_2 decreases significantly with As layer thickness while E_3 slightly increases with As layer thickness. It is noted that Figure 6-12 only show convergent resilient modulus and corresponding stress sates for Aug, which stands for the normal season. Resilient modulus and corresponding stress sates for other months have same tendency that E_2 decreases significantly with As layer thickness while E_3 slightly increases with As layer thickness. Such tendency could be attributed to the changing bulk stress (θ) and octahedral shear stress (τ_{oct}) with As layer thickness, as shown in Fig 6-12 (b). θ has a positive effect on the M_r while τ_{oct} has a negative M_r. In base layer, decreasing θ with thicker As layer is more significant than decreasing τ_{oct} with thicker As layer. Consequently, E_2 decreases from A to D. In subgrade layer, θ increases and τ_{oct} decreases. As a result, E_3 increases from A to D. Since fluctuation of stress states in base layer is much significant than them in subgrade layer, fluctuation of moduli in base layer is more significant than them in subgrade layer. Elastic strains (ε_a and ε_t) are also shown in Figure 6-12 (a). It is clear that no matter compressive strain (ε_a), which is used in Equation (1-1) to calculate N_{fs}, or tensile strain (ε_t), which is used in Equation (1-2) to calculate N_{fa}, all decrease with As layer thickness. Such tendency is reasonable as asphalt mixture has a much larger stiffness than crusher-run material and subgrade soil and a thicker As layer improves the mechanical properties of the whole multi-layer elastic structure. Table 6-6 summarizes the convergent monthly representative base/subgrade layer moduli in A section.

Table 6-6 Convergent monthly representative base/subgrade layer moduli in A section

Name	Elastic moduli (MPa)											
	Jan	Feb	Mar	Apr	May	Jun	Jul	Aug	Sep	Oct	Nov	Dec
E_2-Water content fluctuation	191	185	132	173	175	175	161	169	176	172	170	184
E_2-Climate effect	600	600	105	173	175	175	161	169	176	172	170	184
E_3-Water content fluctuation	74	73	58	74	73	69	68	72	73	73	73	73
E_3-Climate effect	77	200	40	74	73	69	68	72	73	73	73	73

(a) Resilient modulus and strain

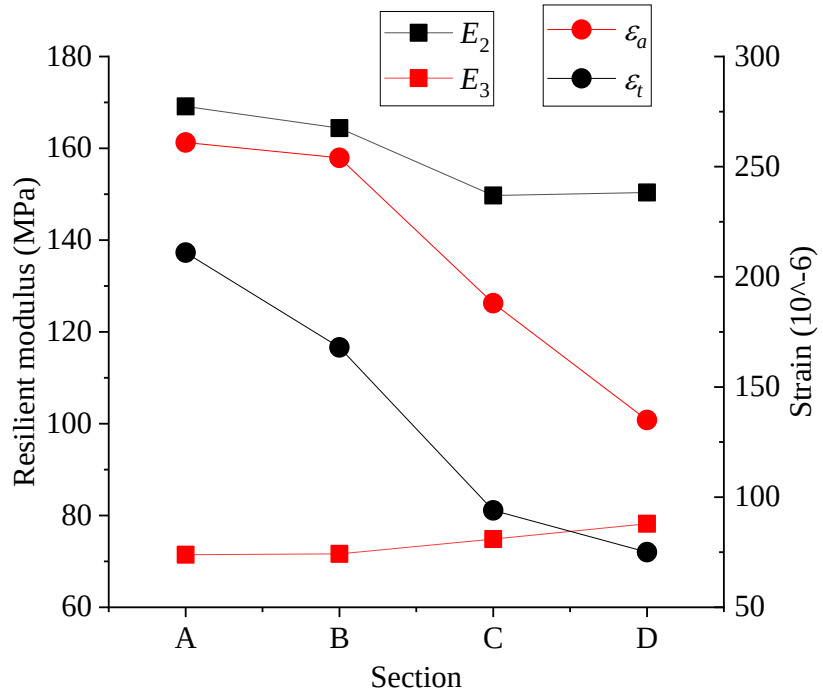

(b) Stress states

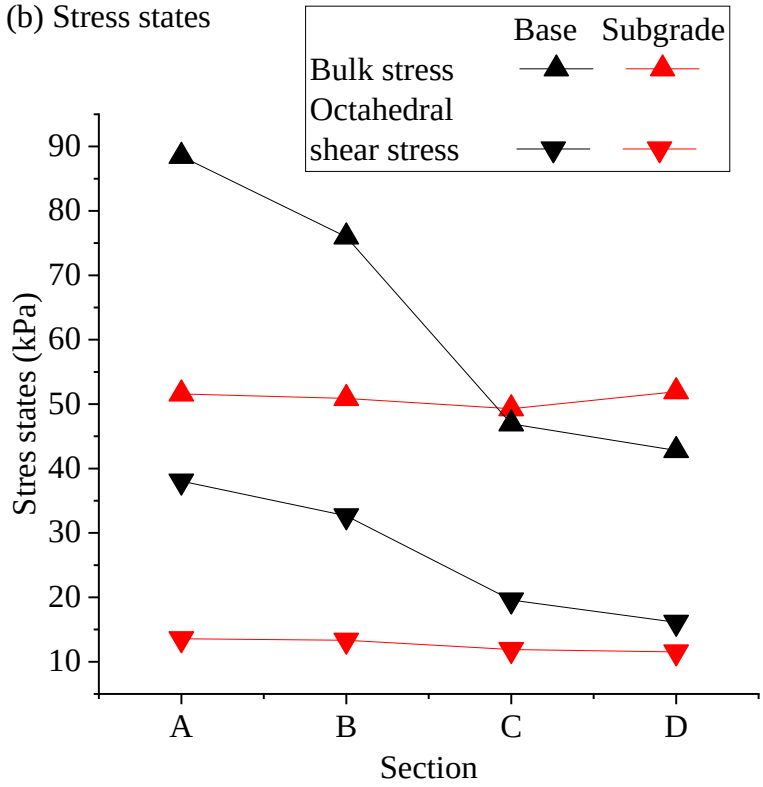

Figure 6-12 Convergent (a) Resilient modulus and (b) stress states in different sections

Figure 6-13 illustrates the calculated fatigue life of all sections through layer moduli with and without convergence analysis. Fatigue life under water content fluctuation condition, which means layer stiffness E_2 and E_3 changing with water contents, and climate condition, which means E_2 and E_3 changing with water contents and freeze-thaw action, are shown in (a) and (b) separately. It is noted that N_{fa} always decreases with convergent E_2 and E_3 regardless of pavement structures while N_{fs} only decreases with convergent E_2 and E_3 in pavement structures with thin As layer (A and B). Fatigue life calculated with constant E_2 and E_3, named as N_f-Original, are also shown in Fig. 14. It is concluded that the effect of convergence analysis on fatigue life is basically more significant compared with effect of water content fluctuation or climate effect regardless of section structure. To be precise, the difference between N_f-Original and N_f-without convergence is much less significant than the difference between N_f- without convergence and N_f-with convergence no matter the water content fluctuation (Fig. 14(a)) or climate effect is considered (Fig. 14(b)). The only exception that the effect of convergence analysis is less significant than effect of water content fluctuation or climate effect is for the fatigue life against rutting (N_{fs}) of structure with thick As layer. For example, for section C and D, the difference between N_{fs}-Original and N_{fs}-without convergence is more significant than the difference between N_{fs}- without convergence and N_{fs}-with convergence. Such phenomenon indicates that thick As layer helps improving the multi-layer structure mechanical properties and reducing the effect of convergence analysis.

The ratio of N_f with convergent E_2 and E_3 to N_f without convergent E_2 and E_3 is also plotted in the Figure 6-13. It is clear that N_{fa} ratio is always lower than 1 and generally decreases with thicker As layer, implies that convergent E_2 and E_3 has a negative effect on the fatigue life against cracking and this effect is more significant in thick As layer pavement structure. On the other hand, N_{fs} ratio increases with thicker As layer from a value lower than 1 to a value higher than 1, implies that convergent E_2 and E_3 has a negative effect on the fatigue life against rutting when As layer is thin. Consequently, convergence analysis for layer stiffness is essential when developing a mathematical flexible pavement design method with high applicability and precision.

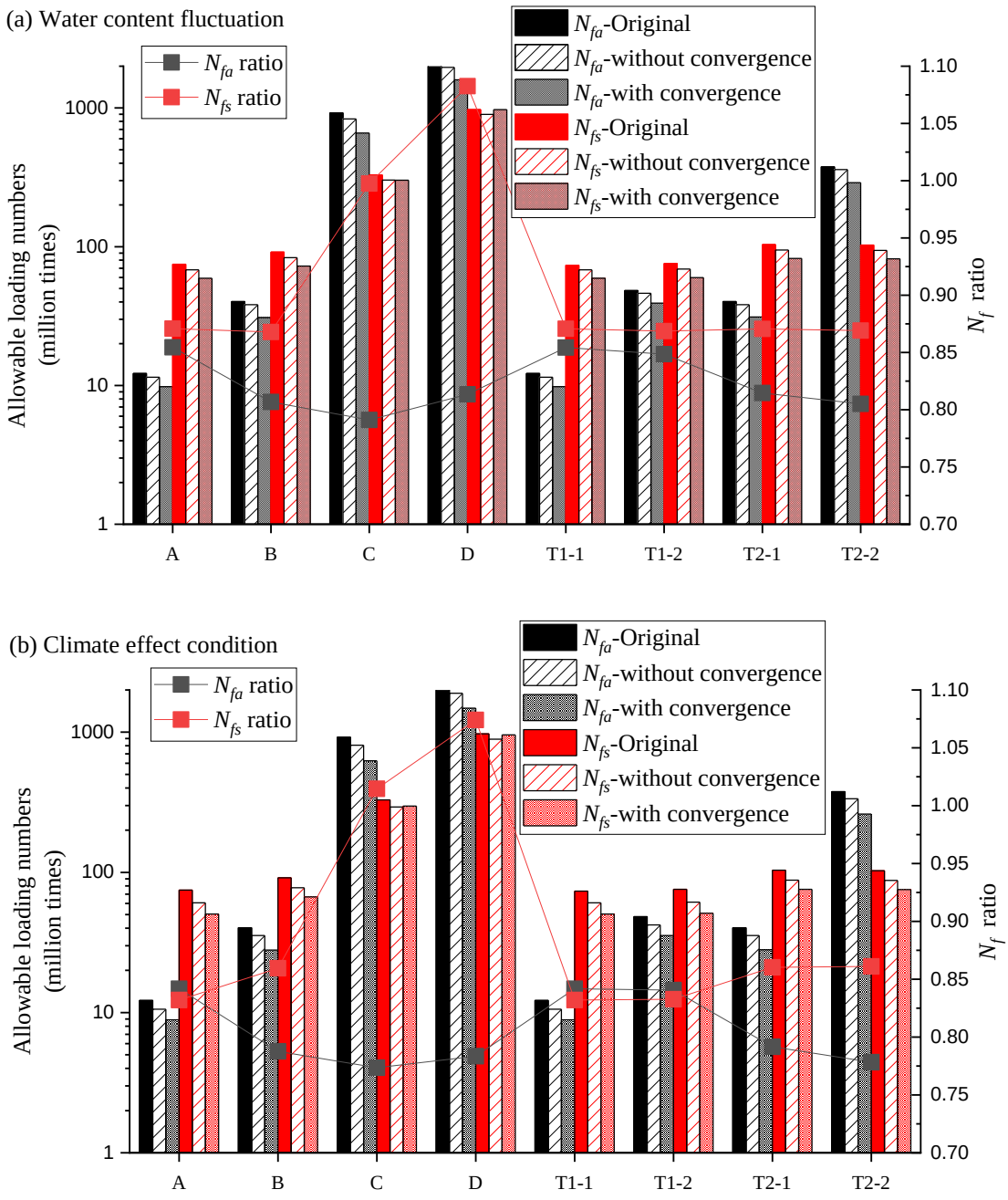

Figure 6-13 Convergence analysis effect on fatigue life under (a) water content fluctuation condition (b) climate effect condition

6.2.3 Climate effect on fatigue life

Figures 6-14 and 6-15 illustrate N_{fs} and N_{fa} of eight test pavement structures under three conditions, Original, Water content fluctuation, Climate effect. It is noted that all fatigue life in water content fluctuation condition and climate condition are calculated with convergent layer moduli. It is obvious that N_{fs} and N_{fa} both decrease from original condition to water content

condition, implies that changing E_2 and E_3 with fluctuating water content decrease pavement fatigue life. N_{fs} and N_{fa} decrease further from water content fluctuation condition to climate condition, indicates that freeze-thaw action decreases fatigue life further as the decreasing E_2 and E_3 during thawing season has a stronger influence on the fatigue life than the increasing E_2 and E_3 during the freezing season.

To clearly discuss the influence of water content fluctuation, freeze-thaw action, and climate effect on the fatigue life, R_{Nf} for different structures are also plotted in the Figures 6-14 and 6-15. The R_{Nf} considering water content fluctuation or climate effect are determined through dividing the N_f-Water content fluctuation or N_f-Climate effect by the N_f-Original, while the R_{Nf} considering freeze-thaw action is determined through dividing the N_f-Climate effect by the N_f-Water content fluctuation. All ratios are lower than 1, indicates that influence of water content fluctuation, freeze-thaw action, and climate effect on E_2 and E_3 all decrease the fatigue life. Within fatigue life against rutting calculation results, R_{Nf} caused by water content, freeze-thaw action, and climate effect are around 0.819, 0.931, and 0.765 separately. In other words, the N_{fs} decreases 18.1% when changing E_2 and E_3 caused by water content fluctuation is considered and it would further decrease 6.9% when effect of freeze-thaw action on E_2 and E_3 is also considered. A synergistic climate effect on E_2 and E_3 decreases N_{fs} about 23.5%. Within fatigue life against cracking calculation results, R_{Nf} caused by water content, freeze-thaw action, and climate effect are around 0.759, 0.93, and 0.706 separately. In other words, the N_{fa} decreases 24.1% when changing E_2 and E_3 caused by water content fluctuation is considered and it would further decrease 7% when effect of freeze-thaw action on E_2 and E_3 is also considered. A synergistic climate effect on E_2 and E_3 decreases N_{fa} about 29.4%.

These results suggest that for improving the applicability and validity of the current Japanese design standard, the introduction of the theoretical design method for pavement structures, which can take account of the effects of the freeze-thaw actions and the concurrent seasonal fluctuation in water content on the subgrade layer stiffness, is effective in the asphalt pavements for cold regions.

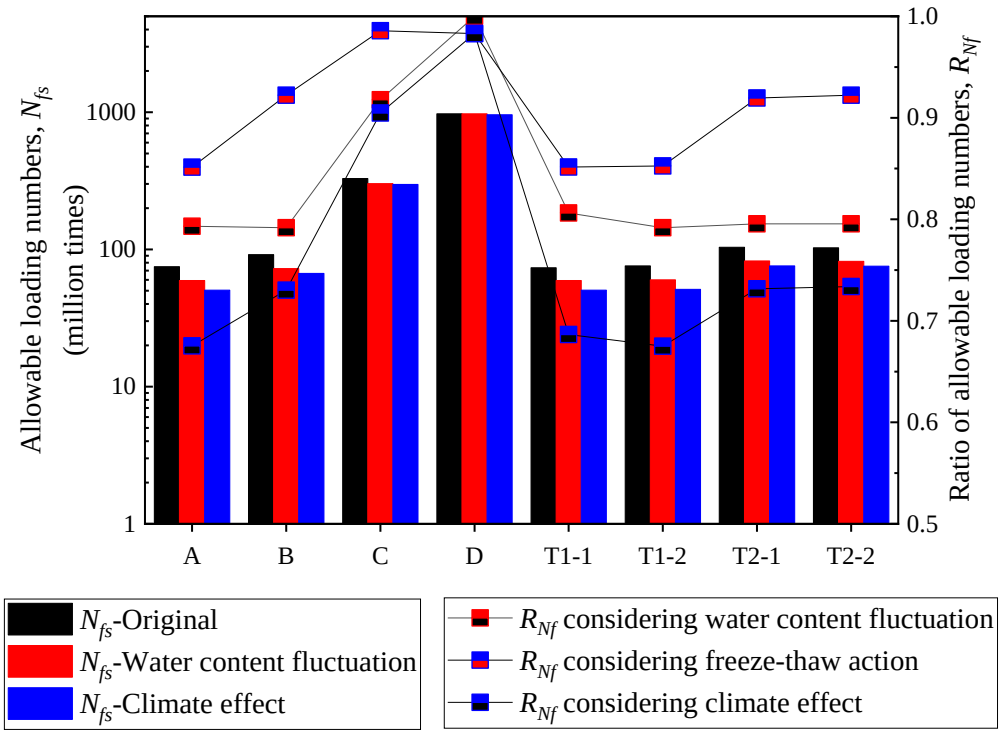

Figure 6-14 Fatigue life against rutting of eight test pavement structures

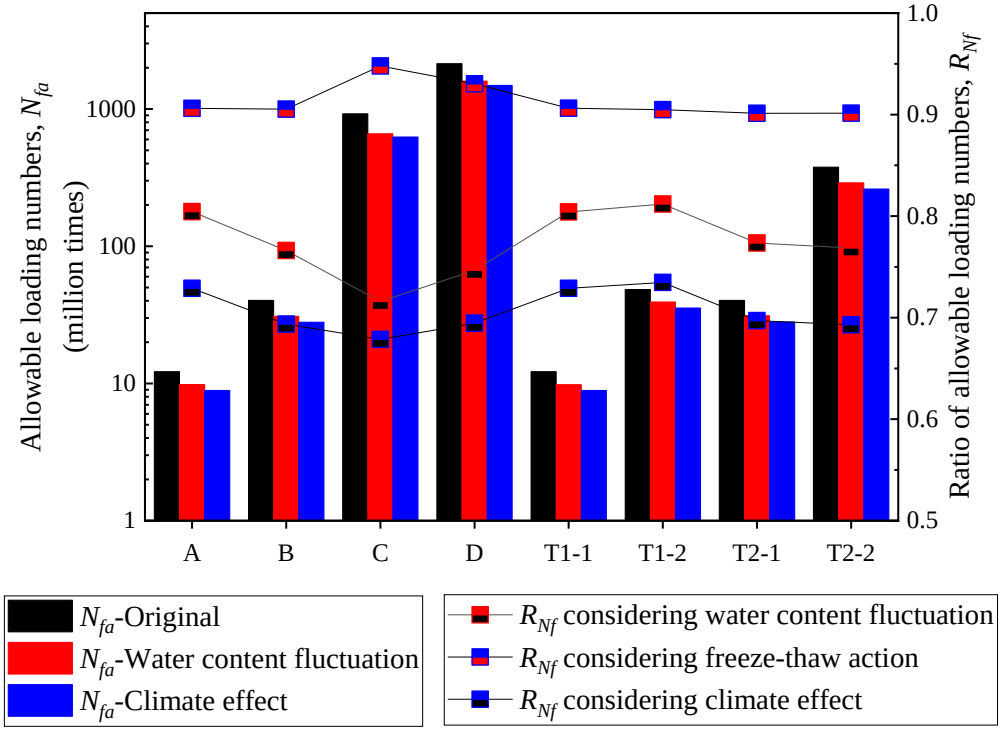

Figure 6-15 Fatigue life against cracking of eight test pavement structures

6.3 MODIFICATION OF FAILURE CRITERIA

6.3.1 MEPDG rutting prediction model

As pointed tin the introduction part, rutting failure criterion used in present Japanese design guide (Equation (1-1)), AI model, is limited that it provides no indication of the behavior of rutting over time or with the application of traffic loading. It also does not provide any indication of rate-hardening, nor does it consider the contribution of the non-subgrade layers to rutting. To overcome these limitations, MEPDG proposed a rutting depth prediction model [NCHRP, 2004], which converts the plastic strain measured from the laboratory to the field condition, as shown in Equation (1-9). This study modified the structure of AI model referring to MEPDG rutting model.

Since the rutting failure threshold value in present Japanese design guide is 15mm, Equation (1-9) could be transferred to following format when $\delta a(N)$ equals to 15mm.

$$15 = \beta_{s1} k_1 \varepsilon_a h (\frac{\varepsilon_0}{\varepsilon_r}) e^{-(\frac{\rho}{N_{fs}})^{\beta}}$$

$$e^{(\frac{\rho}{N_{fs}})^{\beta}} = \frac{\beta_{s1} k_1 \varepsilon_a h (\frac{\varepsilon_0}{\varepsilon_r})}{15}$$

$$(\frac{\rho}{N_{fs}})^{\beta} = ln\left(\frac{\beta_{s1} k_1 \varepsilon_a h (\frac{\varepsilon_0}{\varepsilon_r})}{15}\right)$$

$$\frac{\rho}{N_{fs}} = \left(ln\left(\frac{\beta_{s1} k_1 \varepsilon_a h \left(\frac{\varepsilon_0}{\varepsilon_r}\right)}{15}\right)\right)^{1/\beta}$$

$$N_{fs} = \rho \cdot \left(ln\left(\frac{\beta_{s1} k_1 \varepsilon_a h \left(\frac{\varepsilon_0}{\varepsilon_r}\right)}{15}\right)\right)^{-1/\beta} \quad (6\text{-}7)$$

Figure 6-16 shows the relationship between loading number, N_{fs}, and vertical strain, ε_a, in AI model (Equation (1-1)) and MEPDG model (Equation (1-9)). It is noted that N_{fs}-AI model is much larger than N_{fs}-MEPDG when ε_a locates between 50 to 500 E-6, which is the normal range for ε_a. In other words, AI model greatly overestimate the allowable loading number compares with MEPDG model. To modify the AI model based on MEPDG, an adjusting parameter, β_m, is added on traditional AI model. β_m is calculated through dividing N_{fs}-MEPDG by N_{fs}-AI. A logistic function is used to build the relation between β_m and ε_a, as shown in Figure

16 and Equation (6-8.2). Within the logistic function, A_1 and A_2 are lower and upper limit separately and the A_1 is force as positive value. Consequently, AI-MEPDG model is shown in Equation (6-8) to calculate allowable loading number against rutting.

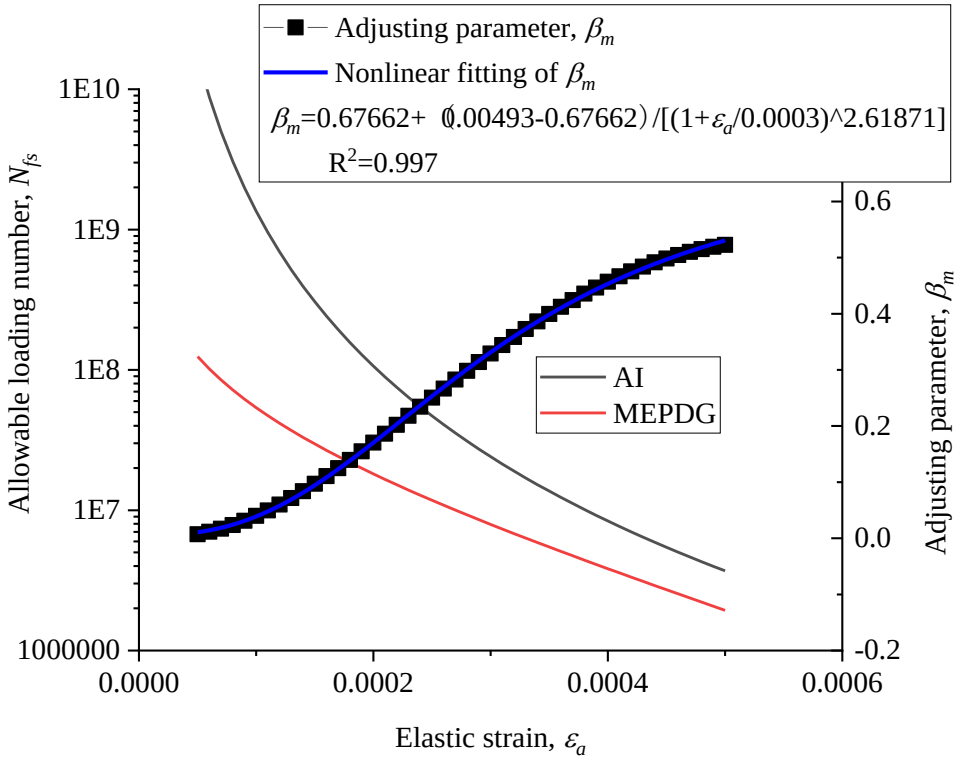

Figure 6-16 Allowable loading number calculated through AI and MEPDG model

$$N_{fs} = \beta_m \cdot \beta_{s1} \cdot \left\{1.365 \times 10^{-9} \cdot {\varepsilon_a}^{-4.477 \cdot \beta_{s2}}\right\} \quad (6\text{-}8.1)$$

$$\beta_m = A_2 + \frac{A_1 - A_2}{1+(\varepsilon_a/x_0)^p} \quad (6\text{-}8.2)$$

$$A_1 = 0.00493 \quad (6\text{-}8.3)$$

$$A_2 = 0.67662 \quad (6\text{-}8.4)$$

$$x_0 = 0.0003 \quad (6\text{-}8.5)$$

$$p = 2.61871 \quad (6\text{-}8.6)$$

$$\beta_{s1} = 2134 \quad (6\text{-}8.7)$$

$$\beta_{s2} = 0.819 \quad (6\text{-}8.8)$$

With AI-MEPDG rutting model, the N_{fs} in climate condition is calculated and illustrated in Figure 6-17. It is noticed that AI-MEPDG gives much smaller predicted N_{fs} than AI model predicted value. However, compared with actual measured loading number at failure, predicted N_{fs} through AI-MEPDG are still too large. Bias between predicted and actual pavement life are

probably caused by enormous variability between designed and actual geography, climatic conditions, construction materials, construction practices, traffic compositions and volumes. Besides variability between designed and actual conditions, which are hard to capture with mechanical calculation, the principal stress axis rotation (PSAR) should not be ignored. It is concluded that MEPDG rutting model is constructed on laboratory results from repeated loading triaxial test that has a constant confining stress and do not consider the effect of PSAR, which is always encountered under in-situ conditions and has a great effect on permanent deformation.

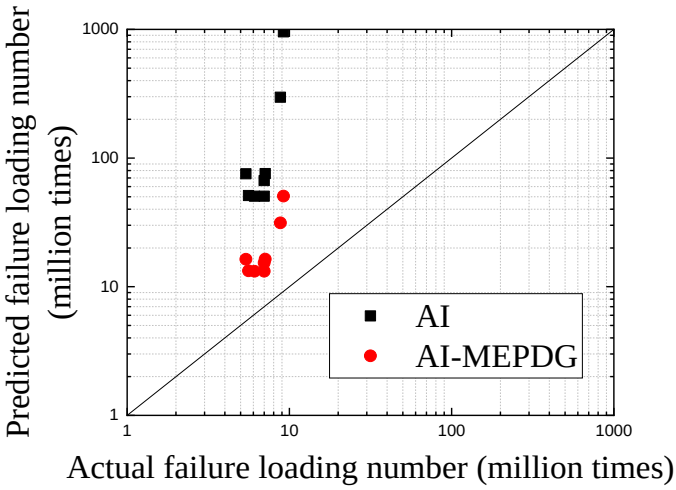

Figure 6-17 Predicted and actual rutting failure loading number

It is also noted that, N_{fs} through AI-MEPDG model in Figure 6-17 is calculated with convergent layer moduli. Figure 6-18 illustrates the ratio of N_{fs} with convergence to N_{fs} without convergence in AI-MEPDG model to show the effect of convergence analysis on fatigue life. Similar to the tendency shown in Figure 6-13, N_{fs} ratio increases with thicker As layer from a value lower than 1 to a value higher than 1, implies that convergent E_2 and E_3 has a negative effect on the fatigue life against rutting when As layer is thin. Again, convergence analysis for layer stiffness is essential when developing a mathematical flexible pavement design method, like AI-MEPDG model, with high applicability and precision.

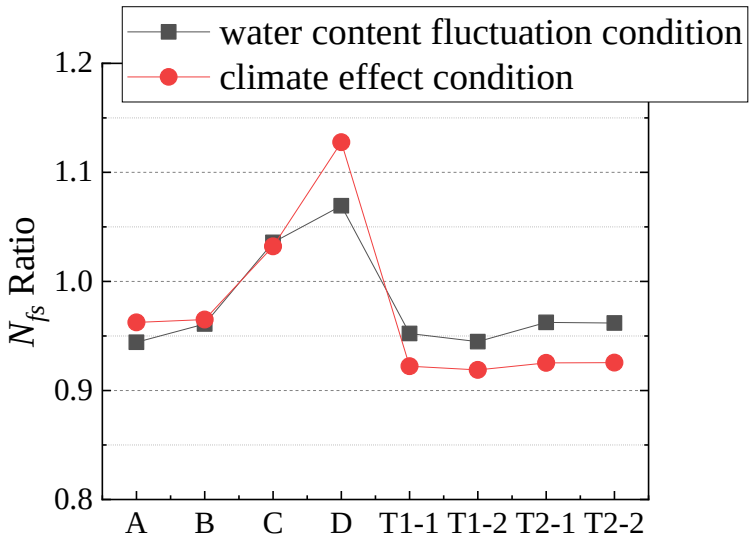

Figure 6-18 Effect of convergence analysis on N_{fs}

6.3.2 Principal stress axis rotation

The amplified permanent strain cause by PSAR is examined by test results through multi-ring shear apparatus, which could simultaneously apply axial load and shear stress to simulate PSAR. More details about the multi-ring shear apparatus could be found at previous researches [Ishikawa et al., 2011]. Figure 6-19 displays permanent axial strain of Toyoura sand with PSAR (hereafter is referred as Moving-wheel Loading test, ML test) and without PSAR (hereafter is referred as Fixed-point Loading test, FL test). Table 6-7 summarizes the experimental conditions of multi-ring shear tests.

Table 6-7 Experimental conditions of multi-ring shear tests for Toyoura sand

Test Name	S_r	Height (mm)	ρ_{dc} (g/cm^3)	$(\sigma_a)_{max}$ (kPa)	$(\tau_{a\theta})_{max}$ (kPa)
FL	Oven-dried	100	1.463	72.58	0
FL	S_r=25.6%	100	1.463	72.58	0
FL	S_r=31.6%	100	1.463	72.58	0
FL	S_r=46%	100	1.463	72.58	0
ML	Oven-dried	100	1.463	72.58	18.12
ML	S_r=25.6%	100	1.463	72.58	18.12
ML	S_r=31.6%	100	1.463	72.58	18.12
ML	S_r=46%	100	1.463	72.58	18.12

It is obvious that PSAR greatly amplifies the permanent axial strain regardless of water content. To quantitatively describe the amplificated axial strain caused by PSAR, ratio of axial strain, $(R_s)_{ave}$, is also plotted in Figure 6-19. $(R_s)_{ave}$ is determined through dividing permanent axial strain with PSAR to those without PSAR. Consequently, all ratios are stable around 1.90 after 180 loading cycles. According to previous research, $(R_s)_{ave}$ could be roughly approximated by Equation (6-9). Consequently, the constant A in Equation (6-9) is determined as 2.57 according to the test results that $(R_s)_{ave}$ equals to 1.9, $(\sigma_a)_{max}$ and $(\tau_{a\theta})_{max}$ are 72.58 kPa and 18.12 kPa respectively.

$$(R_s)_{ave} = \exp\left(A\frac{(\tau_{a\theta})_{max}}{(\sigma_a)_{max}}\right) \quad (6\text{-}9)$$

where $(\sigma_a)_{max}$ is maximum axial stress; $(\tau_{a\theta})_{max}$ is maximum shear stress; A is material constant.

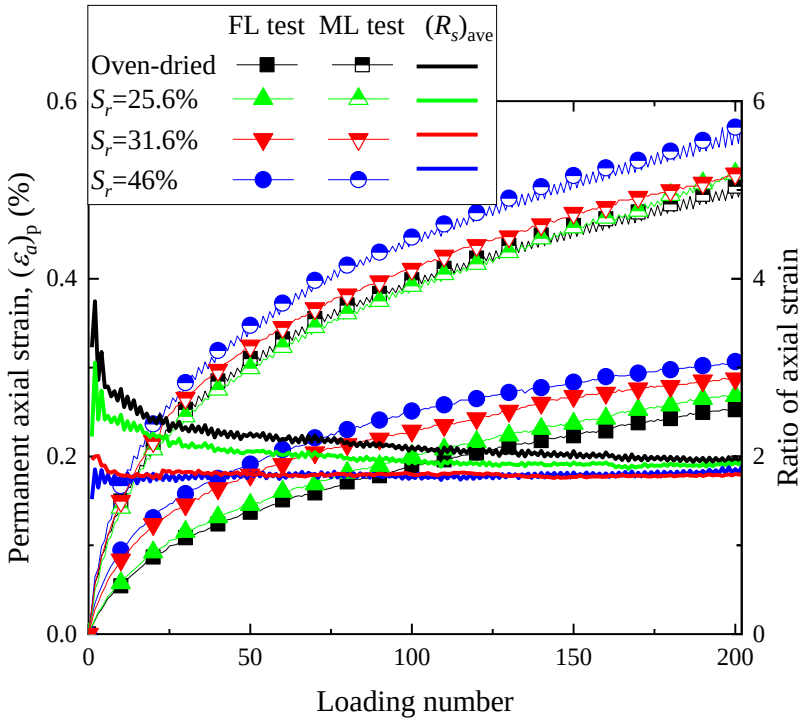

Figure 6-19 Permanent axial strain of Toyoura sand

As $(R_s)_{ave}$ represents the amplification of permanent axial strain caused by PSAR, the reciprocal of $(R_s)_{ave}$ represents the decreasing of failure loading number. As a result, Equation (6-8) is modified by adding the reciprocal of $(R_s)_{ave}$ to capture the effect of PSAR on fatigue life against rutting as shown in Equation (6-10). It is noted that $(\sigma_a)_{max}$ and $(\tau_{a\theta})_{max}$ are stress states in laboratory test through multi-ring shear apparatus. They are equal to vertical stress, $(\sigma_z)_{max}$, and shear stress, $(\tau_{yz})_{max}$, used in GAMES model.

$$N_{fs} = \beta_m \cdot \beta_{s1} \cdot \left\{1.365 \times 10^{-9} \cdot {\varepsilon_a}^{-4.477 \cdot \beta_{s2}}\right\} / \exp\left(\beta_{PSAR} \frac{(\tau_{yz})_{max}}{(\sigma_z)_{max}}\right) \quad (6\text{-}10.1)$$

$$\beta_m = A_2 + \frac{A_1 - A_2}{1 + (\varepsilon_a / x_0)^p} \quad (6\text{-}10.2)$$

$$A_1 = 0.00493 \quad (6\text{-}10.3)$$

$$A_2 = 0.67662 \quad (6\text{-}10.4)$$

$$x_0 = 0.0003 \quad (6\text{-}10.5)$$

$$p = 2.61871 \quad (6\text{-}10.6)$$

$$\beta_{s1} = 2134 \quad (6\text{-}10.7)$$

$$\beta_{s2} = 0.819 \quad (6\text{-}10.8)$$

$$\beta_{PSAR} = 2.57 \quad (6\text{-}10.9)$$

To apply Equation (6-10) into fatigue life prediction, it is necessary to determining the suitable position in subgrade layer to estimate the where $(\sigma_z)_{max}$ and $(\tau_{yz})_{max}$ through GAMES. To investigate how $(\sigma_z)_{max}$ and $(\tau_{yz})_{max}$ change with depth, Section A and layer moduli in Aug are chosen to build a model as shown in Figure 6-20. As a consequence, Figure 6-21 illustrates the σ_z and τ_{yz} in different h and corresponding $(R_s)_{ave}$. It is obvious that σ_z and τ_{yz} show same tendency regardless of h. σ_z reaches the largest value just below the wheel loading (y=0) and decreases with y. On the other hands, τ_{yz} is zero just below the wheel loading and increases to the largest value at y=600mm then decreases. When the h increases, both $(\sigma_z)_{max}$ and $(\tau_{yz})_{max}$ decreases. $(R_s)_{ave}$ in all conditions are around 2.1. Consequently, it is suggested to set the h as 10cm, same depth in convergent analysis of E_3 as shown in Figure 6-10.

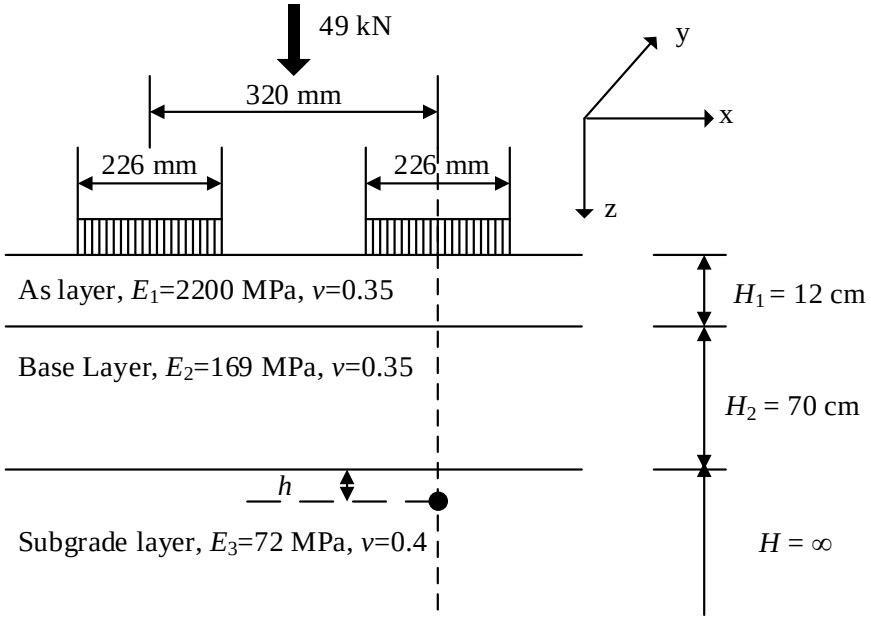

Figure 6-20 Stress states calculation point in subgrade layer

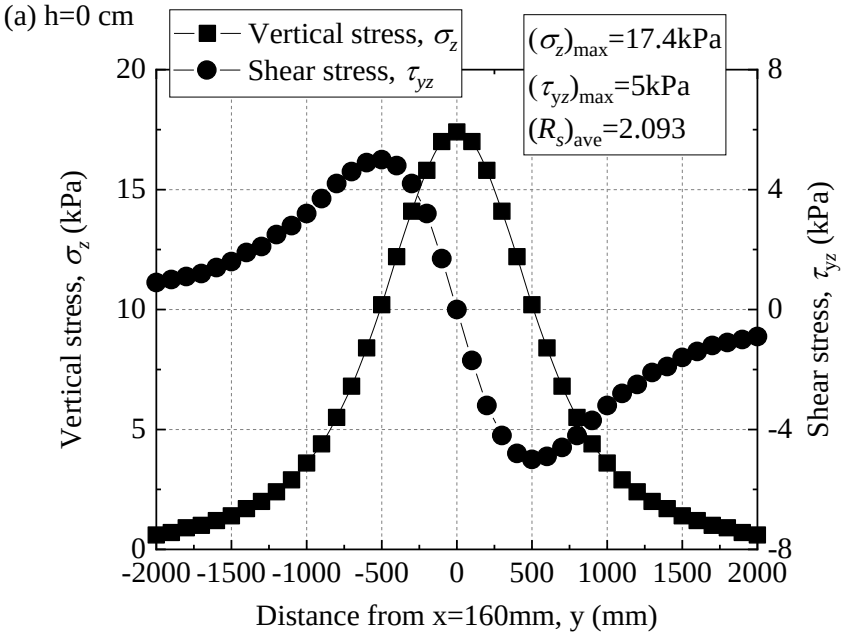

(b) h=5 cm

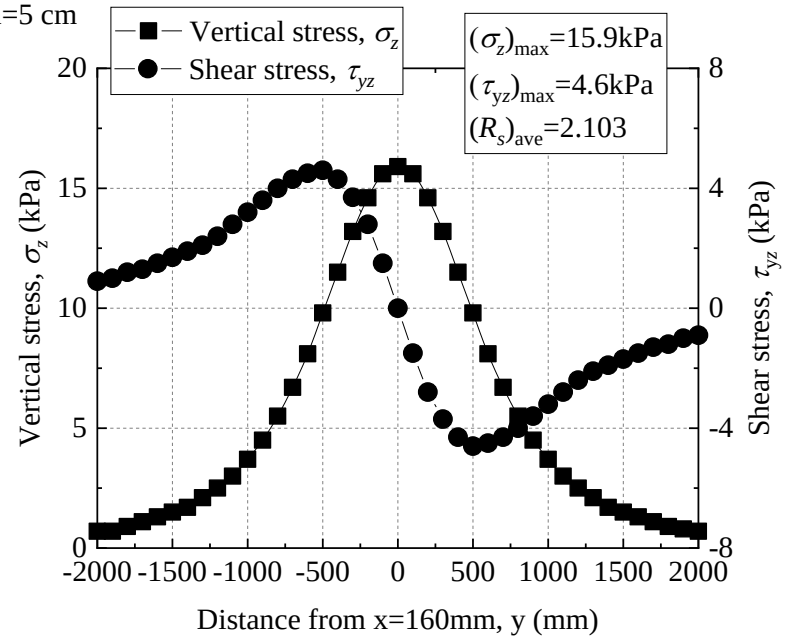

(c) h=10 cm

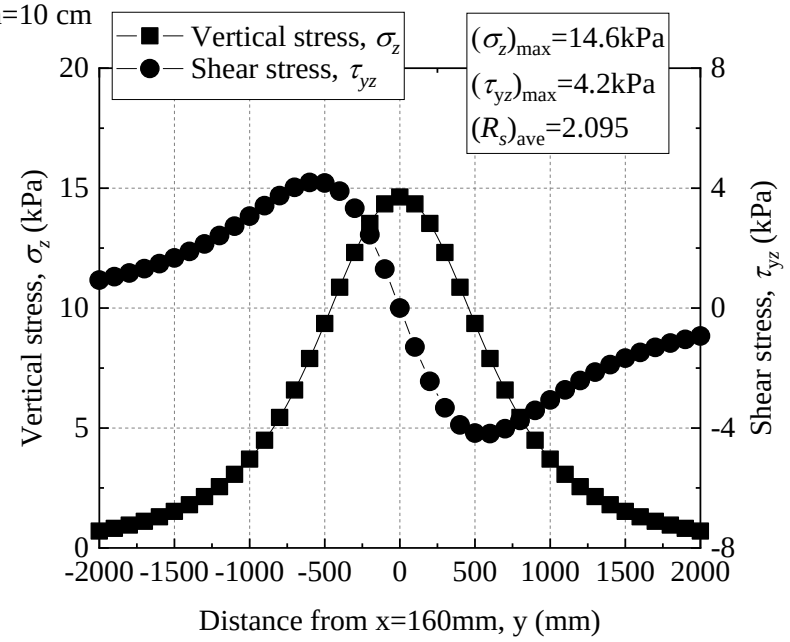

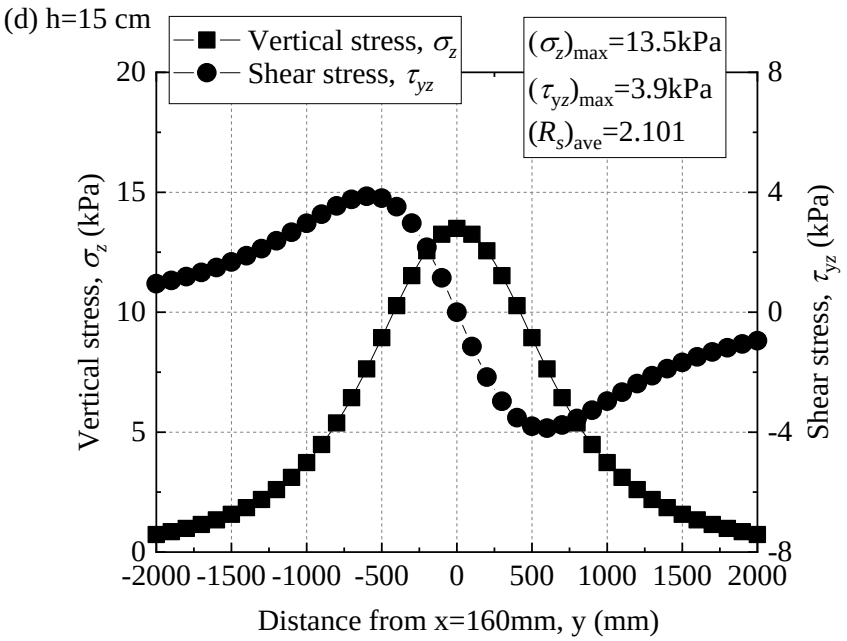

Figure 6-21 Stress states in different depth

Allowable loading number against rutting failure calculated through Equation (6-10) in all eight sections are shown in Figure 6- 22. It is obvious that PSAR greatly decreases calculated fatigue life and N_{fs} with considering PSAR is most close to actual measured failure loading number.

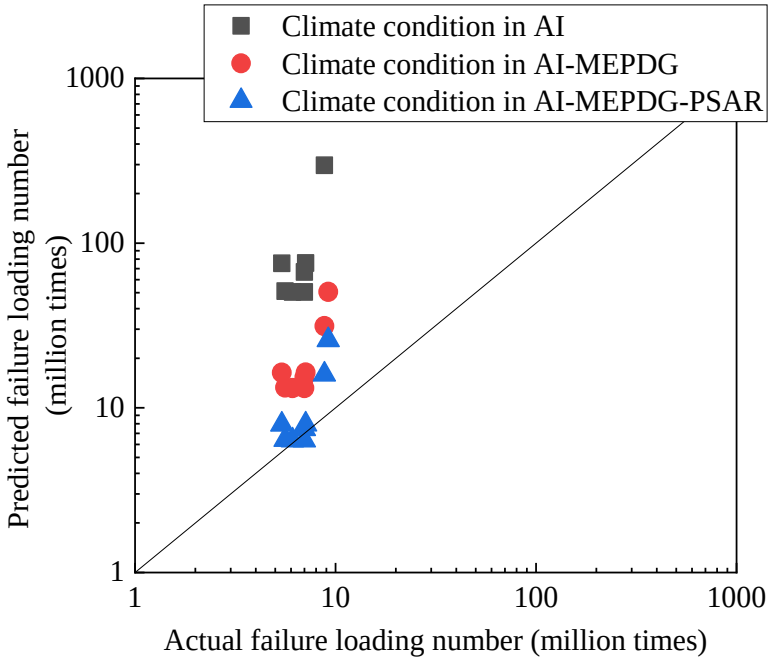

Figure 6-22 Predicted rutting failure loading number considering principal stress axis rotation

Finally, the Figure 6-23 illustrates the sequence in modified Japanese flexible pavement design guide. It should be noted that the modification achieved in this study specially focused on the base/subgrade layer mechanical properties and the rutting failure criterion as shown in the comparison between Figure 6-23 and Figure 1-2.

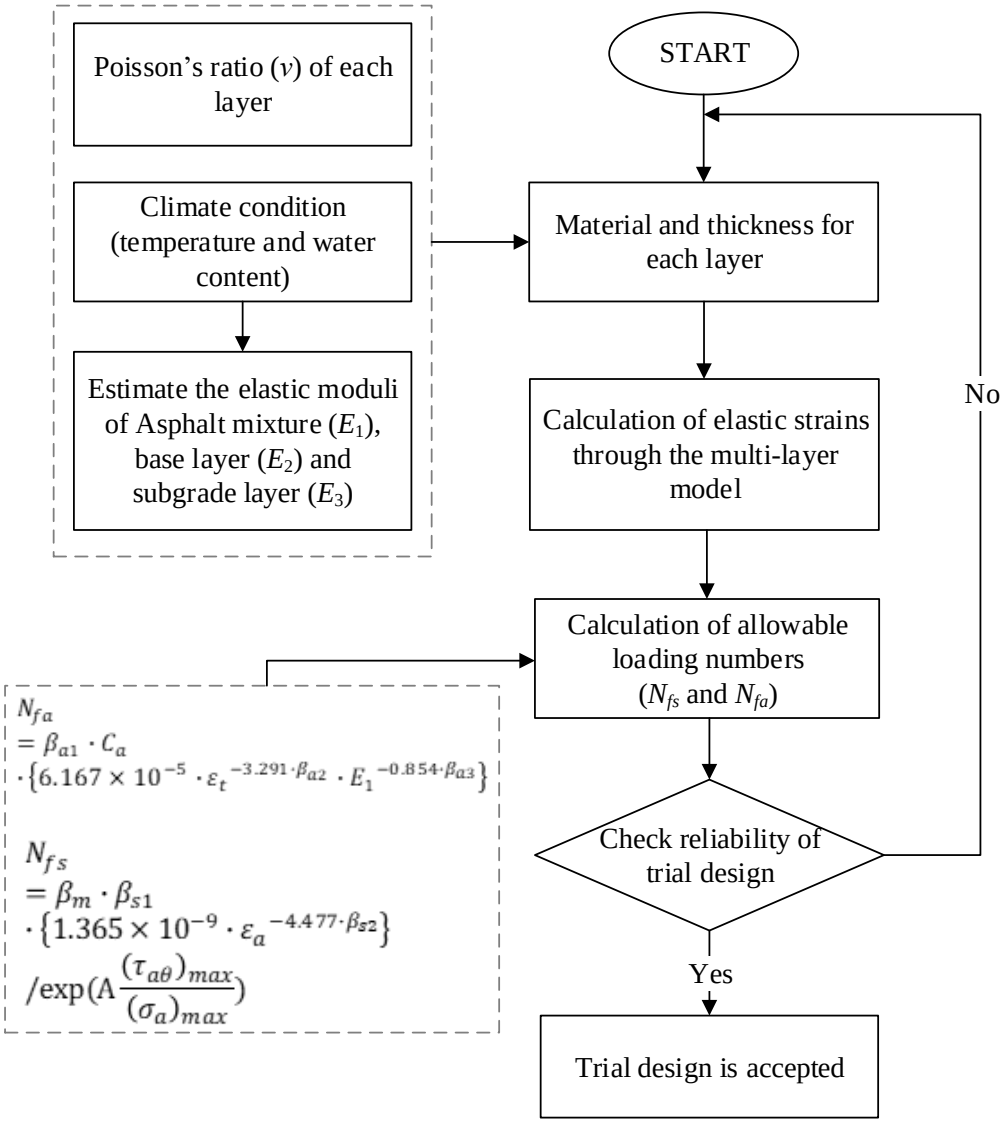

Figure 6-23 Sequence in modified Japanese flexible pavement design guide

6.4 SUMMARY

The following findings can be mainly obtained in this chapter:

1. To modify current Japanese design guide by replacing constant subgrade layer moduli with a variant relating to water content fluctuation and freeze-thaw history, newly proposed modified Ng model, long-term measured in-situ base and subgrade layer water content, and laboratory obtained SWCC are used. Calculated fatigue life against rutting and cracking proves

that both water content fluctuation and freeze-thaw action degrade stiffness of subgrade layer and finally decrease the fatigue life of asphalt pavements in cold regions.

2. Convergence analysis of the base and subgrade layer stiffness is essential since the stress states and resilient modulus affects each other. Analysis results indicate that all moduli are stable after 2-4 iterations and convergent base layer moduli decreases in all pavement structures and convergent subgrade layer moduli decreases in thin As layer structures while increases in thick As layer structures due the variant stress states when pavement structures changing. Accordingly, considering the change in the resilient modulus of base and subgrade layer caused by convergence analysis help determining the reliable layer stiffness and improving prediction accuracy of design guide.

3. Principal stress axis rotation is simulated with multi-ring shear test and it greatly amplifies the permanent strain compared with traditional triaxial repeated loading test. To quantitatively describe the amplificated axial strain caused by principal stress axis rotation, ratio of axial strain, $(R_s)_{ave}$, is proposed and estimated with axial stress and shear stress. $(R_s)_{ave}$ is added into rutting failure criterion and proved to be helpful on increasing prediction accuracy and applicability.

7 FINDING AND ASSIGNMENT

7.1 FINDING

The following findings have been obtained from this study.

- Test results show good consistency with previous research results like SWCC, which proves the validity of the test apparatus. Moreover, a test method for resilient modulus of unsaturated unbound granular materials subjected to freeze-thaw action is proposed and the most significant feature of this method is keeping matric suction stable during freeze-thaw action.
- Through performing a series of suction-controlled resilient modulus tests for a subgrade material with variant freeze-thaw, wheel loads, and water contents conditions, the effects of freeze-thaw actions and the concurrent seasonal fluctuations in water content (named as climate effect in this study) are examined and evaluated. As a consequence, climate effect degrades the resilient deformation characteristics of subgrade materials.
- Climate effect not only reduces the resilient modulus, but also weakens the influences of stress variables like bulk stress, octahedral shear stress, and matric suction on resilient modulus. Besides, the decreasing amount of resilient modulus caused by climate effect is more significant in a saturated condition, which implies that a synergistic effect of water content and freeze-thaw on the resilient modulus. The degradation in resilient modulus caused by freeze-thaw relates to the water content before the specimen is frozen. It is reasonable to assume that the amount of ice formed during the frozen period has a positive relationship with the change of particle skeleton structure uniformity and degradation of the mechanical properties of subgrade materials.
- A new parameter representing the climate effect, F_{clim}, is added into Ng model to quantitatively evaluate resilient modulus for the subgrade material under complex freeze-thaw, fluctuating water content, and variant stress states. A better performance compared with EICM proved the applicability and reliability of newly proposed modified Ng model.
- To modify current Japanese design guide by replacing constant base and subgrade layer moduli with a variant relating to water content fluctuation and freeze-thaw history, newly proposed modified Ng model, long-term measured in-situ base and subgrade

layer water content, and laboratory obtained SWCC are used. Calculated fatigue life against rutting proves that both water content fluctuation and freeze-thaw action degrade stiffness of subgrade layer and finally decrease the fatigue life of asphalt pavements in cold regions.

- Convergence analysis of the base and subgrade layer stiffness is essential since the stress states and resilient modulus affects each other. Analysis results indicate that all moduli are stable after 2-4 iterations and convergent base layer moduli decreases in all pavement structures and convergent subgrade layer moduli decreases in thin As layer structures while increases in thick As layer structures due the variant stress states when pavement structures changing. Accordingly, considering the change in the resilient modulus of base and subgrade layer caused by convergence analysis help determining the reliable layer stiffness and help improving prediction accuracy of design guide.
- Principal stress axis rotation is simulated with multi-ring shear test and it greatly amplifies the permanent strain compared with traditional triaxial repeated loading test. To quantitatively describe the amplificated axial strain caused by principal stress axis rotation, ratio of axial strain, $(R_s)_{ave}$, is proposed and estimated with axial stress and shear stress. $(R_s)_{ave}$ is added into rutting failure criterion and proved to be helpful on increasing prediction accuracy and applicability.
- Shear strength has a more significant influence on permanent deformation of unbound aggregate materials rather than resilient properties especially for test results through multi-ring shear apparatus which simulate the principal stress axis rotation.
- Modified UIUC model show good applicability on prediction of permanent deformation of unbound aggregate specimens with different water contents and stress states. Besides, a simple framework is proposed to predict rutting depth of base layers in flexible pavement structures based on the regression analysis results obtained from modified UIUC model.

7.2 ASSIGNMENT

These findings indicate that a detailed understanding of the mechanical behavior of the base and subgrade layer with complex water content fluctuation, freeze-thaw history, and stress states is essential to develop a mathematical model for the mechanical response of the base and subgrade layer in cold regions and incorporate it into the theoretical design method for pavement structures. Besides, a modification on the structure of failure prediction model by considering principal stress axis rotation is also important to improve the prediction accuracy

and applicability of mechanical-empirical design method for pavement in cold regions. Further and more comprehensive studies including more test on unbound granular materials with various water contents, local calibration with more test pavements are recommended to examine the validity, limitation of application, and so forth as these findings are obtained through limited experimental conditions and only examined with some local test pavement projects. Except widely used MEPDG, other rutting depth prediction model, like UIUC model, show great potential to be applied to practical pavement design since it overcomes many limitations exist in current MEPDG method. The modified UIUC model developed in this study needs further validation, as these findings are obtained through limited aggregate material types and have not been calibrated through comparing with actual rutting depth. Further and more comprehensive studies including more pavement materials and actual field performance to further validate these findings are recommended.

REFERENCES

1. AASHTO, 2008. Mechanistic-Empirical Pavement Design Guide: A Manual of Practice. American Association of State Highway and Transportation Officials, Washington D.C.
2. AASHTO, 2003. Standard method of test for determining the resilient modulus of soils and aggregate materials: AASHTO designation T 307-99. American Association of State Highway and Transportation Officials, Washington D.C.
3. Asphalt Institute, 1982. Research and Development of Asphalt Institute's Thickness Design Manual, 9th ed. Asphalt Institute, College Park Md.
4. Aldrich Jr, HP, 1956. Frost penetration below highway and airfield pavements. Highw. Res. Board Bull. 135, 124-149.
5. Aoki R, Ishikawa T, Tokoro T, Lin T, 2018. Evaluation method for resilient modulus of subgrade materials in cold regions. 58th Technical Report of the Annual Meeting of the JGS Hokkaido Branch, Sapporo; p. 23–30. [in Japanese]
6. Berg RL, Bigl SR, Stark JA, Durell GD, 1996. Resilient modulus testing of materials from Mn/Road: phase 1. https://doi.org/10.21949/1404573
7. Brown SF, 1996. Soil mechanics in pavement engineering. Géotechnique 46(3):383–426. https://doi.org/10.1680/geot.1996.46.3.383
8. Cary CE, Zapata CE, 2011. Resilient modulus for unsaturated unbound materials. Road Mater Pavement Des 12(3):615–638. https://doi.org/10.1080/14680629.2011.9695263
9. Chan FWK, Brown SF, 1994. Significance of principal stress rotation in pavements. 13th International Conference on Soil Mechanics and Foundation Engineering, 1823–1826.
10. Chow L, Mishra D, Tutumluer E, 2014a. Framework for development of an improved unbound aggregate base rutting model for mechanistic-empirical pavement design. Transportation Research Record: Journal of the Transportation Research Board 1:11 – 21. https://doi.org/10.3141/2401-02
11. Chow L, Mishra D, Tutumluer E, 2014b. Aggregate Base Course Material Testing and Rutting Model Development. Final Report, NCDOT Project 2013-18, FHWA/NC/2013-18. North Carolina Department of Transportation Research and Analysis Group, Raleigh, N.C.
12. Cole DM, Irwin LH, Johnson TC, 1981. Effect of freezing and thawing on resilient modulus of a granular soil exhibiting nonlinear behavior. Transportation Research Record: Journal of the Transportation Research Board 809:19–26.
13. Duncan JM, Chang CY, 1970. Nonlinear analysis of stress and strain in soils. Journal of

Soil Mechanics & Foundations Division 96:1629–1653.

14. Fredlund DG, Morgenstern NR, 1977. Stress State Variables for Unsaturated Soils. Journal of Geotechnical and Geoenvironmental Engineering 103(5):447–466.
15. Fredlund DG, Xing A, 1994. Equations for the soil-water characteristic curve. Canadian Geotechnical Journal 31(4):521–532. https://doi.org/10.1139/t94-061
16. Fredlund MD, Wilson GW, Fredlund DG, 2002. Use of the grain-size distribution for estimation of the soil-water characteristic curve. Canadian Geotechnical Journal 39(5):1103–1117. https://doi.org/10.1139/t02-049
17. Gräbe PJ, Clayton CR, 2009. Effects of principal stress rotation on permanent deformation in rail track foundations. Journal of Geotechnical and Geoenvironmental Engineering 135(4):555-565. https://doi.org/10.1061/(ASCE)1090-0241(2009)135:4(555)
18. Han Z, Vanapalli SK, 2016. State-of-the-art: Prediction of resilient modulus of unsaturated subgrade soils. International Journal of Geomechanics 16(4):04015104. https://doi.org/10.1061/(ASCE)GM.1943-5622.0000631
19. Huang YH, 2004. Pavement Analysis and Design, 2nd ed. Pearson Education, Inc.
20. Inam A, 2012. Performance evaluation of unsaturated base course materials subject to repeated traffic loads. Hokkaido University, 2012.
21. Inam A, Ishikawa T, Miura S, 2012. Effect of principal stress axis rotation on cyclic plastic deformation characteristics of unsaturated base course material. Soils and Foundations 52(3):465-480. https://doi.org/10.1016/j.sandf.2012.05.006
22. Ishikawa T, Lin T, Kawabata S, Kameyama S, Tokoro T, 2019a. Effect evaluation of freeze-thaw on resilient modulus of unsaturated granular base course material in pavement. Transportation Geotechnics 21:100284. https://doi.org/10.1016/j.trgeo.2019.100284
23. Ishikawa T, Lin T, Yang J, Tokoro T, Tutumluer E, 2019b. Application of the UIUC model for predicting ballast settlement to unsaturated ballasts under moving wheel loads. Transportation Geotechnics 18:149-162. https://doi.org/10.1016/j.trgeo.2018.12.003
24. Ishikawa T, Tokoro T, Miura S, 2016. Influence of freeze–thaw action on hydraulic behavior of unsaturated volcanic coarse-grained soils. Soils and Foundations 56 (5):790–804. https://doi.org/10.1016/j.sandf.2016.08.005
25. Ishikawa T, Zhang Y, Tokoro T, Miura S, 2014a. Medium-size triaxial apparatus for unsaturated granular subbase course materials. Soils and Foundations 54(1):67-80. https://doi.org/10.1016/j.sandf.2013.12.007

26. Ishikawa T, Miura S, Sekine E, 2014b. Simple plastic deformation analysis of ballasted track under repeated moving-wheel loads by cumulative damage model. Transportation Geotechnics 1(4):157–170. https://doi.org/10.1016/j.trgeo.2014.06.006
27. Ishikawa T, Kawabata S, Kameyama S, Abe R, Ono T, 2012. Effects of freeze-thawing on mechanical behavior of granular base in cold regions. 10-12 September 2012. In: I Miura, H Yoshida, Abe, editors. Advances in Transportation Geotechnics II, Proceeding of the International Conference, Sapporo; 118–124.
28. Ishikawa T, Sekine E, Miura S, 2011. Cyclic deformation of granular material subjected to moving-wheel loads. Canadian Geotechnical Journal 48(5):691-703. https://doi.org/10.1139/t10-099
29. Ishikawa, T., Miura, S., and Sekine, E, 2007. Development and performance evaluation of multi-ring shear apparatus. Proceedings of the International Workshop on Geotechnical Aspects and Processed Material; 53–64.
30. Japan Road Association, 2006. Pavement design manual, Japan Road Association, Tokyo. [in Japanese]
31. Japan Society of Civil Engineers, 2015. Characteristics and Evaluation of Sub-grade and Base Course Materials, Japan Society of Civil Engineers, Tokyo. [in Japanese]
32. Japanese Geotechnical Society, 2009. Test Method for frost susceptibility of soils (JGS 0172-2003), Standards of Japanese Geotechnical Society for Laboratory Soil Testing Methods; 2009. p. 45–50. [in Japanese]
33. Johnson TC, Cole DM, Chamberlain EJ, 1978. Influence of freezing and thawing on the resilient properties of a silt soil beneath an asphalt concrete pavement. U.S. Cold Regions Research and Engineering Laboratory, CRREL Report 78–23. http://hdl.handle.net/11681/9380
34. Jong DT, Bosscher P, Benson C, 1998. Field assessment of changes in pavement moduli caused by freezing and thawing. Transportation Research Record: Journal of the Transportation Research Board 1615:41–8. https://doi.org/10.3141/1615-06
35. Kim DS, Kweon GC, Lee KH, 1997. Alternative method of determining resilient modulus of compacted subgrade soils using free-free resonant column test. Transportation Research Record: Journal of the Transportation Research Board 1577(1):62–69. https://doi.org/10.3141/1577-08
36. Kishikawa T, Otgonjargal D, Kawaguchi T, Nakamura D, Yamashita S, 2017. Influence of freeze-thaw on stress propagation in the ground. Proc., 57th Technical Report of the Annual Meeting of the JGS Hokkaido Branch, Kitami; 27–34. [in Japanese]

37. Korkiala-Tanttu L, 2009. Verification of rutting calculation for unbound road materials. Proceedings of the Institution of Civil Engineers-Transport, 162(2): 107-114. https://doi.org/10.1680/tran.2009.162.2.107
38. Liang RY, Rabab'ah S, Khasawneh M, 2008. Predicting moisture-dependent resilient modulus of cohesive soils using soil suction concept. Journal of Transportation Engineering 134(1):34–40. https://doi.org/10.1061/(ASCE)0733-947X(2008)134:1(34)
39. Maina JW, Matsui K, 2004. Developing software for elastic analysis of pavement structure responses to vertical and horizontal surface loadings. Transportation Research Record: Journal of the Transportation Research Board 1896(1):107–118. https://doi.org/10.3141/1896-11
40. Maruyama K, Tako J, Kasahara A, 2008. Fatigue failure life prediction method of asphalt pavement. Journal of Japan Society of Civil Engineers Division E 64(3):416–426. [in Japanese] https://doi.org/10.2208/jsceje.64.416
41. Maruyama K, Tako J, Kasahara A, 2006. Long-term performance of asphalt pavements at bibi new test road. Journal of Japan Society of Civil Engineers Division E 62(3):519–530. [in Japanese] https://doi.org/10.2208/jsceje.62.519
42. Miura K, Miura S, Toki S, 1986. Deformation behavior of anisotropic dense sand under principal stress axis rotation. Soils and Foundations 26(1):36–52. https://doi.org/10.3208/sandf1972.26.36
43. Mori T, Kamiya K, Chiba T, Uzuoka R, Kazama M, 2009. The functional model of the soil-water characteristic curve used the logistic function during cyclic shearing. 44th Japan national conference on geotechnical engineering, 1519-1520. [in Japanese]
44. NCHRP, 2004. Guide for mechanistic-empirical design of new and rehabilitated pavement structures, National Cooperative Highway Research Program, Washington, D.C.
45. Ng CWW, Zhou C, Yuan Q, Xu J, 2013. Resilient modulus of unsaturated subgrade soil: experimental and theoretical investigations. Canadian Geotechnical Journal 50(2):223–232. https://doi.org/10.1139/cgj-2012-0052
46. Saeed A, Hall JW, Barker W, 2001. NCHRP Report 453: Performance-Related Tests of Aggregates for Use in Unbound Pavement Layers. TRB, National Research Council, Washington, D.C.
47. Seed HB, CHAN CK, Monismith CL, 1955. Effects of repeated loading on the strength and deformation of compacted clay. Highway Research Board Proceeding 34:541-558.

48. Simonsen E, Isacsson U, 2001. Soil behavior during freezing and thawing using variable and constant confining pressure triaxial tests. Canadian Geotechnical Journal 38(4):863–875. https://doi.org/10.1139/t01-007
49. Simonsen E, Isacsson U, 1999. Thaw weakening of pavement structures in cold regions. Cold Regions Science and Technology 29(2):135–151. https://doi.org/10.1016/S0165-232X(99)00020-8
50. Simonsen E, Janoo VC, Icacsson U, 2002. Resilient properties of unbound road materials during seasonal frost conditions. Journal of Cold Regions Engineering 16(1):28–50. https://doi.org/10.1061/(ASCE)0887-381X(2002)16:1(28)

NOTATIONS

The following symbols were used in this dissertation.

N_f: Allowable loading number of equivalent 49-kN wheel loads calculated in current Japanese design guide

N_{fs}: Allowable loading number of equivalent 49-kN wheel loads against rutting calculated in current Japanese design guide

N_{fa}: Allowable loading number of equivalent 49-kN wheel loads against cracking calculated in current Japanese design guide

β_{s1}, β_{s2}: The compensation rates for AI rutting failure criteria based on the actual situation of Japanese pavement

β_{a1}, β_{a2}, and β_{a3}: The compensation rates for AI cracking failure criteria based on the actual situation of Japanese pavement

C_a: The asphalt mixture parameter

K_a: Correction factor, which relates to the thickness of asphalt mixture

H_1: Thickness of asphalt mixture

H_2: Thickness of base layer

ε_a: The compressive strain on the top surface of the subgrade layer

ε_t: The tensile strain on the lower surface of the asphalt mixture layer

v: Poisson's ratio

E: Elastic modulus

E_1: Elastic moduli of asphalt mixture layer

E_2: Elastic moduli of base layer

E_3: Elastic moduli of subgrade layer

M_p: The monthly mean temperature of asphalt mixture at depth of h_1

h_1: The depth equals to one-third of the height of asphalt mixture

M_a: The monthly mean air temperature

$N_{fs.d}$: Failure loading number of equivalent 49-kN wheel loads against rutting calculated in current Japanese design guide

$N_{fa.d}$: Failure loading number of equivalent 49-kN wheel loads against cracking calculated in current Japanese design guide

M_r: Resilient modulus

k_1, k_2, k_3: Regression constants used in the universal model

p_a: The atmospheric pressure and set as 101 kPa in this study

θ: The bulk stress

τ_{oct}: The octahedral shear stress

k_1, k_2, k_3, k_4: Regression constants used in the Ng model

σ_{net}: The net mean stress, defined as [θ /3-u_a]

u_a: The pore-air pressure

u_w: The pore-water pressure

ψ: The matric suction

F_{env}: The factor used in EICM representing the reduction of resilient modulus caused by freeze-thaw

$\varepsilon_p(N)$: The permanent strain for the layer/sub-layer predicted in MEPDG rutting model

N: The number of traffic repetitions

ε_0, β, and ρ: Material properties used in MEPDG rutting model

ε_r: The resilient strain imposed in laboratory test to obtain material properties ε_0, β, and ρ

ε_v: The average vertical resilient strain in the layer

β_1: The calibration factor for the unbound granular and subgrade materials in MEPDG rutting model

W_c: The water content

ε_p: The permanent vertical strain in the K-T model

C_k: The permanent strain in the first loading cycle

b: The shear ratio parameter depending on the material

R: The shear failure ratio

q: The deviator stress

q_f: The deviator stress in failure

q_0: The deviator stress when p' equals to zero

p': The mean effective principal stress

c: The cohesion

ϕ: The friction angle

M: The slope of the failure line in p'-q space in triaxial test

c', d: Material parameters used in K-T model

σ_d: The applied deviator stress

SSR: The shear stress ratio

τ_f: The mobilized shearing resistance acting on failure plane

σ_f: The normal stress acting on failure plane

τ_{max}: The available shear strength obtained through Mohr-Coulomb failure criteria

A, B, C, D: Regression parameters used in the UIUC model

ρ_d: The dry density

D_c: Degree of compaction

S_r: Degree of saturation

S_{rr}: Residual degree of saturation:

S_e: Effective degree of saturation

q_{max}: Maximum deviator stress

q_{cyclic}: Cyclic deviator stress

q_{const}: Constant deviator stress

σ_c: Confining pressure

N_c: The loading number in laboratory test

f: The loading frequency

$E(f)$: The resilient modulus at any frequency, f

$F(\psi)$: The frequency effect, which is affected by matric suction, ψ

E_s: Secant Young's modulus, defined as the ratio of cyclic deviator stress to the $(\varepsilon_a)_{max}$

$(\varepsilon_a)_{max}$: The maximum axial strain during one loading cycle

$(\varepsilon_a)_r$: The recoverable axial strain during one loading cycle

$(\varepsilon_a)_p$: The permanent axial strain during one loading cycle

F_{clim}: The factor proposed in this study representing the reduction of resilient modulus caused by freeze-thaw

z: The average frost-penetration depth predicted in the modified Berggren formula

α: The correction coefficient used in the modified Berggren formula

F: The freezing index which is the average air temperature during freezing season multiplied by its duration in days

$(L/\lambda)_{eff}$: The effective ratio of L to λ

L: The latent heat of soil

λ: The thermal conductivity of the soil

$\gamma_{a\theta}$: Shear strain

ρ_{dc}: Dry density after consolidation

σ_a: The axial stress

$(\sigma_a)_{max}$: Maximum axial stress

$(\tau_{a\theta})_{max}$: Maximum shear stress

$(R_s)_{ave}$: The average ratio of axial strain between specimen with and without principal stress axis rotation

A, B, C, D, E: regression parameters used in the modified UIUC model

K_0: The coefficient of earth pressure at rest

ϕ': Effective internal friction angle

σ_1, σ_2, and σ_3: First, second, and third principal stress

α: The direction of major principal stress

η: The stress ratio

b: The principal stress parameter, which describes the relative magnitudes of the three principal stresses

$M_{r(\mathrm{CBR})}$: Resilient modulus detected with a freeze-thaw CBR (California Bearing Ratio) test apparatus

N_F: The number of freeze-thaw cycle

θ: Volumetric water content

R^2: The coefficient of determination

RMSE: Root mean square error

R_{Nf}: The ratio of allowable loading number N_f

σ_z: The vertical stress calculated in GAMES

τ_{yz}: The shear stress calculated in GAMES

β_m: The adjusting parameter used in AI model

$(\sigma_z)_{\max}$: Maximum vertical stress

$(\tau_{yz})_{\max}$: Maximum shear stress

β_{PSAR}: The adjusting parameter used in AI model: